UNIVERSIDADE DE SÃO PAULO
Instituto de Ciências Matemáticas e de Computação

Numerical simulation of complex fluid flows with moving interfaces

Hugo Leonardo França

Tese de Doutorado do Programa de Pós-Graduação em Ciências de Computação e Matemática Computacional (PPG-CCMC)

ICMC USP SÃO CARLOS

Hugo Leonardo França

Numerical simulation of complex fluid flows with moving interfaces

Thesis submitted to the Instituto de Ciências Matemáticas e de Computação – ICMC-USP – in accordance with the requirements of the Computer and Mathematical Sciences Graduate Program, for the degree of Doctor in Science. *FINAL VERSION*

Concentration Area: Computer Science and Computational Mathematics

Advisor: Prof. Dr. José Alberto Cuminato
Co-advisor: Prof. Dr. Cassio Machiaveli Oishi

USP – São Carlos
July 2023

Ficha catalográfica elaborada pela Biblioteca Prof. Achille Bassi
e Seção Técnica de Informática, ICMC/USP,
com os dados inseridos pelo(a) autor(a)

França, Hugo Leonardo
F814n Numerical simulation of complex fluid flows with moving interfaces / Hugo Leonardo França; orientador José Alberto Cuminato; coorientador Cassio Machiaveli Oishi. -- São Carlos, 2023.
125 p.

Tese (Doutorado - Programa de Pós-Graduação em Ciências de Computação e Matemática Computacional) -- Instituto de Ciências Matemáticas e de Computação, Universidade de São Paulo, 2023.

1. Fluidos complexos. I. Cuminato, José Alberto, orient. II. Oishi, Cassio Machiaveli, coorient. III. Título.

Bibliotecários responsáveis pela estrutura de catalogação da publicação de acordo com a AACR2:
Gláucia Maria Saia Cristianini - CRB - 8/4938
Juliana de Souza Moraes - CRB - 8/6176

Hugo Leonardo França

Simulação numérica de escoamentos de fluidos complexos com interfaces móveis

Tese apresentada ao Instituto de Ciências Matemáticas e de Computação – ICMC-USP, como parte dos requisitos para obtenção do título de Doutor em Ciências – Ciências de Computação e Matemática Computacional. *VERSÃO REVISADA*

Área de Concentração: Ciências de Computação e Matemática Computacional

Orientador: Prof. Dr. José Alberto Cuminato
Coorientador: Prof. Dr. Cassio Machiaveli Oishi

USP – São Carlos
Julho de 2023

ACKNOWLEDGEMENTS

I would like to greatly thank my supervisor Cassio Oishi for constantly supporting me for over a decade in my studies. I probably would have never entered the world of Computational Mathematics if you had not invited me during my undergraduate years. I have learned so much under your supervision since then and I am very grateful for that.

I thank my co-supervisor Mazi Jalaal for accepting and including me in your Amsterdam group and for offering me so much help during the last year of my PhD.

I also thank my supervisor in São Carlos, José Alberto Cuminato, for participating in this project.

My PhD colleague Irineu Palhares, for the collaboration that resulted in the article partially shown in chapter 3 of this thesis.

All my friends at ICMC in São Carlos, who I have spent so much time with during my first year. Our group interactions were greatly missed by me during the next two pandemic years that followed.

My friends at the FluidLab and the Institute of Physics at the University of Amsterdam. I thank you for always including me as a part of your group and making me feel extremely welcome during my visit. I also thank you for so patiently helping me many times with all the very basic physics questions that I had, especially Yuri, Tom, Antoine and Nico.

This research was supported by grants #2019/01811-9 and #2021/14953-6 by the São Paulo Research Foundation (FAPESP). Many of the results presented here were obtained using the computational resources of the Center for Mathematical Sciences Applied to Industry (CeMEAI) funded by FAPESP grant #2013/07375-0.

RESUMO

FRANÇA, H. L. **Simulação numérica de escoamentos de fluidos complexos com interfaces móveis**. 2023. 125 p. Tese (Doutorado em Ciências – Ciências de Computação e Matemática Computacional) – Instituto de Ciências Matemáticas e de Computação, Universidade de São Paulo, São Carlos – SP, 2023.

Escoamentos de diferentes tipos de fluidos não-newtonianos são numericamente investigados com foco em problemas complexos, como por exemplo escoamentos confinados em geometrias com singularidades e escoamentos com interfaces móveis e tensão superficial. Em geometrias confinadas, a formulação tensão natural é usada para representar o tensor tensão polimérico em escoamentos viscoelásticos. Uma maior precisão é obtida próximo a singularidades geométricas em comparação com a tradicional formulação cartesiana. Em escoamentos com interfaces móveis, um novo algoritmo baseado em aprendizado de máquina é proposto e validado para o cálculo da curvatura de interfaces Front-Tracking. Verifica-se que é possível obter resultados similares aos obtidos por abordagens mais tradicionais. A implementação viscoelástica é testada com o modelo Phan-Thien-Tanner para o problema da colisão binária de gotas. Mapas paramétricos são obtidos, classificando os resultados nas categorias *bouncing*, coalescência, e separação em função de números adimensionais que governam o problema. Além do espaço tradicional Newtoniano definido pelo número de Weber e o fator de impacto, também explora-se o número de Weissenberg e o parâmetro de extensibilidade PTT. Para casos sem *bouncing*, os resultados mostram que a tensão superficial e elasticidade mantém a integridade da gota, inibindo a separação da mesma. Por outro lado, efeitos *shear-thinning* induzem a separação. Deste modo, no modelo PTT existem tendências opostas associadas a elasticidade e ao *shear-thinning*, o que pode levar a respostas não-monotônicas. Também é estudado o espalhamento de uma gota elastoviscoplástica (EVP) sobre uma camada fina do mesmo fluido. Modelando o material EVP com o modelo de Saramito, realiza-se uma análise adimensional para entender a competição entre tensão superficial e tensão de escoamento, e como a elasticidade afeta este balanço. Observa-se que, para fluidos menos viscosos, elasticidade pode aumentar significativamente o espalhamento de uma gota, pois a tensão interna que resiste o escoamento se desenvolve mais lentamente devido ao tempo de relaxação polimérico. Este efeito é mais evidente em materiais com uma alta tensão de escoamento, o que indica que a elasticidade tem um maior impacto em sólidos elásticos do que em fluidos. Acredita-se que os resultados nesta tese podem esclarecer quanto a importância dos parâmetros elásticos em problemas industriais comuns como impressões 3D com espalhamento de gotas, ou *sprays* com coalescência de quebra de gotas.

Palavras-chave: Fluidos complexos, Escoamentos com interfaces móveis, Solução numérica.

ABSTRACT

FRANÇA, H. L. **Numerical simulation of complex fluid flows with moving interfaces**. 2023. 125 p. Tese (Doutorado em Ciências – Ciências de Computação e Matemática Computacional) – Instituto de Ciências Matemáticas e de Computação, Universidade de São Paulo, São Carlos – SP, 2023.

Flows of different types of non-Newtonian fluids are numerically investigated with a focus on complex problems, as for instance confined flows in geometries with singularities and moving interface flows with surface tension. For confined geometries, the novel natural stress formulation is used to represent the polymeric stress tensor in viscoelastic flows, and we show that greater accuracy is obtained near geometrical singularities in comparison to the traditional Cartesian formulation. For flows with a moving interface, we propose and validate a new algorithm based on machine learning to estimate the curvature in Front-Tracking interfaces, showing that it can provide similar results compared to more traditional approaches. Our viscoelastic implementation is tested with the Phan-Thien-Tanner model for the problem of binary droplet colisions. We provide maps of outcomes associated with the categories of Bouncing, Coalescence, and Separation as functions of the dimensionless numbers that govern the problem. In addition to the traditional Newtonian space defined by the Weber and the impact factor, associated with the collision angle, we also explore the Weissenberg number and the extensibility parameter in the PTT model. For non-bouncing scenarios, the results show that surface tension and elasticity act to maintain the integrity of the merged drop and avoid Separation. On the other hand, shear-thinning effects induce the Separation outcome. Hence, in the PTT model there are opposite trends associated with elasticity and shear-thinning, what can lead to non-monotonic responses. We also study the spreading of an elastoviscoplastic droplet over a thin-film. By modelling an elastoviscoplastic material using Saramito's model, we perform a nondimensional analysis to understand the competition between surface tension and yield-stress, and how elasticity affects this balance. We can see that, for less viscous fluids, elasticity can greatly increase the spreading of a droplet, since the internal resisting stresses develop more slowly due to the polymeric relaxation time. This effect is more pronounced for materials of high yield-stress, which indicates elasticity has a greater impact for elastic solids than fluids. We believe the results in this thesis could shed light on the importance of elastic parameters in common industrial problems such as 3D printing with spreading of droplets or sprays with droplet coalescence and breakup.

Keywords: Complex fluids, Moving interface flows, Numerical solution.

LIST OF FIGURES

Figure 1 – Rheological curves for some types of fluids covered in this thesis. a) Stress versus strain rate flow curves. b) Viscosity curves as a function of the strain rate. c) Elastic storage modulus as a function of the strain. 23

Figure 2 – Examples of applications in which the study of complex materials with moving interfaces is of importance. a) Droplets sitting on a leaf. b) Bubble bursting in a volcanic magma medium. c) Inkjet Drop-On-Demand printing system. 24

Figure 3 – Computational cell i, j and its points of interest on the staggered grid. 33

Figure 4 – Example of cell classification in a free surface simulation. 34

Figure 5 – Eight cases of possible normal vectors used in the free surface boundary conditions. 35

Figure 6 – Illustration of the free surface during the topological change algorithm that coalesces two blocks of fluid. 40

Figure 7 – Illustration of the free surface during the topological change algorithm that breaks a block of fluid presenting a thin filament. 41

Figure 8 – Geometry of the 4 : 1 contraction flow (a) and non-uniform mesh details (b). 45

Figure 9 – Time variation of the CSF (left) and NSF (right) local residuals near to the singularity. 47

Figure 10 – Horizontal profiles ($y = 0$) of u, p and $T^P_{22} - T^P_{11}$ at the steady-state for CSF and NSF considering the Newtonian velocity field. 48

Figure 11 – Visualization of the colour map for the flow classification parameter with the Newtonian velocity field. 49

Figure 12 – Zoom for the colour map visualization around the re-entrant corner with the Newtonian velocity field. 49

Figure 13 – Illustration of the selected angles for studying the asymptotic behaviour near the singularity. 50

Figure 14 – Asymptotic variation near the singularity. Variation of T^{xx}, T^{xy}, T^{yy} using CSF (left), and variaton of λ, μ and ν using NSF (right). 51

Figure 15 – Dominance of the groups of terms for components xx, xy and yy within the Cartesian constitutive equation in a Newtonian velocity field: first column for CSF and second column for NSF. 53

Figure 16 – Time variation of the CSF and NSF local residuals near the singularity using the viscoelastic velocity field. 54

Figure 17 – Horizontal profiles ($y = 0$) of u, p and $T_{22}^P - T_{11}^P$ at the steady-state for CSF and NSF considering the true viscoelastic velocity fields. For the viscoelastic velocity field, it was considered the hybrid version of the NSF (EVANS; FRANÇA; OISHI, 2019), denoted as Hyb. NSF. 55
Figure 18 – Visualization of the colour map for the flow classification parameter in a viscoelastic velocity field. a) CSF and b) Hybrid NSF. 56
Figure 19 – Dominance of the groups of terms for components 11, 12 and 22 within the Cartesian constitutive equation using the viscoelastic velocity field: first column for CSF and second column for NSF. 57
Figure 20 – Examples of cell classification in a free surface simulation with coalescence. 64
Figure 21 – Schematic of the geometry used in the binary droplet collision simulations. . 65
Figure 22 – Initial geometry setup for a binary droplet collision simulation. In this computational setup, the dimensionless lengths were defined using the droplet diameter, D, as characteristic quantity. 66
Figure 23 – Comparison between the numerical results and the semi–empirical time scale of Planchette et al. (PLANCHETTE *et al.*, 2017) for the ratio t_{Dmax}/t_{oscill} versus We. Parameters (S.I. units): $D = 0.0005$, $\rho = 948$, $\eta_s = 0.03$, $\sigma = 0.02$ and U is varied in the interval $[0.02, 2.90]$. The dimensionless numbers fixed in the simulations are $B = 0$ and $\beta = 1$. 67
Figure 24 – Transient dynamic of the interface for three different outcomes: bouncing (left), coalescence (middle) and separation (right). The black interfaces represent the results for the mesh size $h = 0.025$ while the red interfaces describe the results for the mesh size $h = 0.0125$. Parameters (S.I units): $D = 0.000375$, $\rho = 998$, $\eta_s = 0.0082$, $\sigma = 0.0458$, $\beta = 1$ and U is varied as U=$\{1.106,\ 1.916,\ 2.926\}$. The non-dimensionals are $Oh = 0.063$, while We and Re are taken as the pairs $(We, Re) = (10, 50.49), (30, 87.45), (50, 133.58)$. 68
Figure 25 – 'on of the x and y-thickness: blue curves are used to represent the numerical results for the current work while the results for the modified SPH scheme of (XU; TANG; YU, 2020) are plotted using orange curves. These simulations assume the cross-model for the viscosity function. Parameters (reduced units): $D = 25.04$, $U = 0.6$, $\rho = 1.78$, $\sigma = 2.13$, $\eta_0 = 1$, $\eta_\infty = 0.1$, $K = 1$, $m = 1$. The non-dimensionals are: $Re = 26.74$, $We = 7.53$ and $Oh = 0.102$. 69
Figure 26 – Experimental (left) and numerical (right) regime map for the CY model considering $n = 0.4$. The experimental results were obtained from (FINOTELLO *et al.*, 2018). Parameters (S.I. units): $D = 0.00102$, $\rho = 1000$, $\sigma = 0.072$, $\eta_0 = 0.228$, $\eta_\infty = 0.0025$, $\eta_{app} = 0.0038$, $\lambda = 3.29$, $a = 9.4$, $n = 0.4$, $U \in [0.838,\ 2.653]$. The non-dimensionals are $Oh = 0.014$, while We and Re are taken as the pairs $(We, Re) = (10, 225.88)$, $(20, 319.44)$, $(30, 391.23)$, $(45, 479.16)$, $(55, 529.73)$, $(90, 677.63)$, $(100, 714.29)$. 70

Figure 27 – Outcomes of *Bouncing* (magenta), *Coalescence* (blue), and *Separation* (green) in the $\{We, B\}$ space for shear thinning case with different levels of power-law index, corresponding to $n = \{0.1; 0.4; 0.7; 1\}$. Parameters (S.I. units): $D = 0.00102$, $\rho = 1000$, $\sigma = 0.072$, $\eta_0 = 0.228$, $\eta_\infty = 0.0025$, $\eta_{app} = 0.0038$, $\lambda = 3.29$, $a = 9.4$, $U \in [0.838,\ 2.653]$ and n is indicated above each map. The non-dimensionals are $Oh = 0.014$, while We and Re are taken as the pairs $(We, Re) = (10, 225.88)$, $(20, 319.44)$, $(30, 391.23)$, $(45, 479.16)$, $(55, 529.73)$, $(70, 597.61)$, $(80, 638.88)$, $(90, 677.63)$, $(100, 714.29)$. 72

Figure 28 – Transient dynamics of the interface for $B = 0.8$, $Re = 714.29$, $We = 100$, $Oh = 0.014$ and different values of n: $n = 0.1$ (black), $n = 0.4$ (red), and $n = 0.7$ (blue). Other parameters (S.I. units): $D = 0.00102$, $\rho = 1000$, $\sigma = 0.072$, $\eta_0 = 0.228$, $\eta_\infty = 0.0025$, $\eta_{app} = 0.0038$, $\lambda = 3.29$, $a = 9.4$, $U = 2.653$. . . 73

Figure 29 – Outcomes of the Oldroyd–B droplet collision corresponding to *Bouncing*, *Coalescence*, and *Separation* in the $\{Wi, We\}$ space for different values of the impact factor, $B = \{0; 0.4; 0.8\}$. Non-dimensional parameters: $\beta = 1/9$, $Wi = \{0, 1, 2, 3, 4, 5\}$, $B = \{0, 0.4, 0.8\}$, $Oh = 0.063$, Re and We are taken as the pairs $(We, Re) = (10, 50.49)$, $(30, 87.45)$, $(40, 100.98)$, $(50, 112.89)$, $(60, 123.67)$, $(70, 133.58$

Figure 30 – The $\{We, B\}$ map of outputs in the collision of two identical droplets of an Oldroyd–B fluid for different values of Wi. Non-dimensional parameters: $\beta = 1/9$, $Wi = \{0, 1, 2, 3\}$, $B = \{0, 0.2, 0.4, 0.6, 0.8\}$, $Oh = 0.063$, Re and We are taken as the pairs $(We, Re) = (10, 50.49)$, $(30, 87.45)$, $(40, 100.98)$, $(50, 112.89)$, $(60, 123.67)$, ... 75

Figure 31 – Transient dynamic of the interface for the Oldroyd–B case with fixed values of $B = 0.2$, $We = 10$, $Re = 50.49$, $Oh = 0.063$, $\beta = 1/9$. Black: Newtonian and red: Oldroyd-B with $Wi = 5$. 76

Figure 32 – Max radius over time for a bouncing simulation with fixed values of $B = 0.2$, $We = 10$, $Re = 50.49$, $Oh = 0.063$, $\beta = 1/9$. Black: Newtonian and red: Oldroyd-B with $Wi = 5$. 77

Figure 33 – Transient dynamic of the interface for the Oldroyd–B case with fixed values of $B = 0.6$, $We = 40$, $Re = 100.98$, $Oh = 0.063$, $\beta = 1/9$. The black interfaces represent the Newtonian limit case, while the red and blue interfaces correspond to $Wi = 1.5$ and $Wi = 3$, respectively. 78

Figure 34 – The $\{We, Wi\}$ map of outputs in the collision of two identical droplets of a PTT fluid for different values of ε. Non-dimensional parameters: $B = 0$, $\beta = 1/9$, $Wi = \{0, 1, 2, 3, 3.5, 4, 4.5, 5\}$, $Oh = 0.063$, $\varepsilon = \{0.05, 0.25\}$, Re and We are taken as the pairs $(We, Re) = (10, 50.49)$, $(30, 87.45)$, $(40, 100.98)$, $(50, 112.89)$, $(60, 123.6$ 79

Figure 35 – Transient dynamic of the interface for the PTT case with fixed values of $B = 0.3$, $We = 50$, $Re = 112.89$, $Oh = 0.063$, $\beta = 1/9$ and $Wi = 2.5$. The black and red interfaces correspond to $\varepsilon = 0.05$ and $\varepsilon = 0.25$, respectively. . 80

Figure 36 – The $\{We, Wi\}$ map of outputs in the collision of two identical droplets of a PTT fluid for different values of B. Non-dimensional parameters: $B = \{0, 0.1, 0.2, 0.3\}$, $\beta = 1/9$, $Wi = \{0, 1, 2, 3, 3.5, 4, 4.5, 5\}$, $Oh = 0.063$, $\varepsilon = 0.25$, Re and We are taken as the pairs $(We, Re) = (10, 50.49)$, $(30, 87.45)$, $(40, 100.98)$, $(50, 112.89)$,

Figure 37 – Transient dynamic of the interface for the PTT case with fixed values of $\varepsilon = 0.25$, $\beta = 1/9$, $We = 30$, $Re = 87.45$, $Oh = 0.063$ and $Wi = 4$. The black and red interfaces correspond to $B = 0$ and $B = 0.3$, respectively. . . . 82

Figure 38 – Description of the parameters F_i used to approximate the curvature at the point p_i. . . . 85

Figure 39 – Neural network used to describe the function C. . . . 86

Figure 40 – Dataset generation for the Front-Tracking method: (Left) normals pointing outside of the circle and (Right) normals pointing into the circle in which negative curvature is assumed. . . . 87

Figure 41 – Scatter plots of the exact curvature versus the machine learning predicted curvature for each entry in the test dataset (generated from circles). Three values of N and two values of h are used to compare results. In this figure, the curvature values on the axis scaling are given by $\kappa = \pm 1/R$, with R varying from 0.00225 to 0.475. . . . 88

Figure 42 – Results for the sine wave function. Left: plots of the exact and analytical curvature for $x \in [-\pi, \pi]$. Right: Scatter plot of the exact versus machine learning curvature according to the limits of sine wave curvature, e.g. $[-1, 1]$. 89

Figure 43 – Time sequence comparison between numerical and experimental droplet collisions in two cases: coalescence (a) and bouncing (b). In the numerical panels two interfaces are shown: interface obtained from the FT-ML curvature (blue) and from a traditional FT scheme (red). Panels from experimental results are reproduced from (PAN; LAW; ZHOU, 2008), with the permission of AIP Publishing. . . . 91

Figure 44 – Experimental (a) and numerical (b) regime maps for the Newtonian binary droplet collision. . . . 92

Figure 45 – Time sequence of three different simulations illustrating the possible outcomes: coalescence, bouncing and separation. . . . 93

Figure 46 – a) Sketch of the geometry of a spreading elastoviscoplastic droplet. We assume the droplet to be axisymmetric around the z-axis. b) Mechanical analog of Saramito's elastoviscoplastic model. . . . 97

Figure 47 – Non-uniform grid generated for the spreading simulation. Cells are colored by their level of refinement. We note that this figure does not capture the entire domain, which continues both in the r and z directions. 102
Figure 48 – Convergence tests for the Bingham regularization parameter (left) and for the mesh refinement parameter (right). For the regularization tests, the mesh is fixed at Level = 10. For the mesh tests, the regularization is fixed at $\varepsilon_{vp} = 10^{-3}$. 103
Figure 49 – Numerical mesh convergence tests for purely viscoelastic simulations. Left: droplet radius over time for different mesh levels. Right: droplet height over time. 104
Figure 50 – Convergence tests for the EVP regularization parameter (left) and for the mesh refinement parameter (right). In the regularization tests, we keep fixed the mesh level as 10 and in the mesh tests we fix the regularization $\varepsilon_{evp} = 10^{-7}$. All simulations are performed with Wi = 0.816 and $J = 0.18$. 104
Figure 51 – Viscoplastic droplet final radius and height as a function of the plastocapillary number. The theoretical prediction is developed in (JALAAL; STOEBER; BALMFORTH, 2021). The gray line indicates the initial radius and height of the droplets. 105
Figure 52 – Spreading radius (top) and height (bottom) over time for different values of the Weissenberg number. 106
Figure 53 – Anatomy of the flow inside a viscoelastic droplet with Wi = 0.245 at different time stamps. Regions of $\xi = 0$ indicate purely shear flow, $\xi = 1$ extensional flow, and $\xi = -1$ solid-like rotation. 107
Figure 54 – Distribution of the polymeric stress at different timestamps inside a elastoviscoplastic droplet with Wi $= 0.816$ and $J = 0.18$. Blue regions indicate stress below the plastocapillary number J (unyielded) and red regions are above J (yielded). 108
Figure 55 – Distribution of the polymeric stress inside the elastoviscoplastic droplet for different values of Wi and J. All snapshots are taken at time $t = 8.165$. Blue regions indicate stress below the plastocapillary number J (unyielded) and red regions are above J (yielded). We note that the colorbar limits do not include the total range of values present in the data, since we are only interested in visualizing regions that are above or below zero. 109
Figure 56 – Time evolution of the spreading height of an elastoviscoplastic droplet for different plastocapillary and Weissenber numbers. 110
Figure 57 – Final spreading radius (top) and height (bottom) of an elastoviscoplastic droplet as a function of the plastocapillary and Weissenberg numbers. 111

CONTENTS

1 GENERAL INTRODUCTION 21

2 MATHEMATICAL MODEL 27
2.1 Governing equations 27
2.2 Natural stress formulation 28
2.3 Boundary conditions 30
2.3.1 Solid walls *30*
2.3.2 Inflow *30*
2.3.3 Outflow *30*
2.3.4 Symmetry *31*
2.3.5 Free surface *31*
2.4 Overview of the numerical method 32
2.4.1 Projection method *32*
2.4.2 Spatial discretization *32*
2.4.3 Cell classification *33*
2.4.4 Time discretization for the momentum equation *35*
2.4.5 Pressure update equation *35*
2.4.6 Boundary conditions for the Poisson equation *36*
2.4.7 Strain tensor update *37*
2.4.7.1 Updating via CSF *37*
2.4.7.2 Updating via NSF *37*
2.4.8 Topological changes in the interface *38*
2.4.8.1 Case 1: Coalescence *38*
2.4.8.2 Case 2: Breakup *39*
2.4.9 Summarizing *40*

3 NATURAL STRESS FORMULATION ON A CONTRACTION FLOW 43
3.1 Introduction 43
3.2 Numerical setup 44
3.3 Results in a Newtonian velocity field 46
3.3.1 Temporal convergence *46*
3.3.2 Global behaviour *46*
3.3.3 Spatial convergence near the singularity *50*

3.3.4 *Boundary layer structures* . . . *50*
3.4 Results in the true viscoelastic velocity case . . . 52
3.4.1 *Temporal convergence* . . . *52*
3.4.2 *Global behaviour* . . . *52*
3.4.3 *Boundary layer structures* . . . *54*
3.5 Conclusions . . . 58

4 SHEAR-THINNING AND VISCOELASTIC BINARY DROPLET COLLISION . . . 59
4.1 Introduction . . . 59
4.2 Governing equations and nondimensionalization . . . 62
4.2.1 *Shear-thinning materials* . . . *62*
4.2.2 *Viscoelastic materials* . . . *63*
4.2.3 *Discretization and numerical coalescence* . . . *63*
4.2.4 *Computational geometry* . . . *64*
4.3 Validation of the numerical methodology . . . 66
4.3.1 *Newtonian fluids* . . . *66*
4.3.2 *Shear-thinning fluids* . . . *69*
4.4 Results . . . 71
4.4.1 *Shear–thinning* . . . *71*
4.4.2 *Oldroyd–B* . . . *71*
4.4.3 *PTT* . . . *74*
4.5 Conclusions . . . 77

5 A MACHINE LEARNING STRATEGY FOR COMPUTING INTERFACE CURVATURE IN FRONT-TRACKING METHODS . . . 83
5.1 Learning curvature and testing . . . 84
5.2 Application of the scheme for solving a complex free surface flow . . . 90
5.3 Conclusions . . . 92

6 ELASTOVISCOPLASTIC DROPLET SPREADING . . . 95
6.1 Introduction . . . 95
6.2 Problem description: capillary spreading of a droplet . . . 97
6.3 Governing equations . . . 98
6.4 Numerical method . . . 100
6.4.1 *Numerical regularization* . . . *101*
6.5 Validation of the numerical methodology . . . 102
6.5.1 *Purely viscoplastic validation* . . . *102*
6.5.2 *Purely viscoelastic validation* . . . *103*
6.5.3 *Elastoviscoplastic validation* . . . *103*

6.6 Results and discussion 103
6.6.1 Pure viscoplasticity *103*
6.6.2 Pure viscoelasticity *106*
6.6.3 Elastoviscoplastic spreading *107*
6.7 Conclusions 111

7 GENERAL CONCLUSION 113

BIBLIOGRAPHY 115

CHAPTER

1

GENERAL INTRODUCTION

Non-Newtonian materials are found in many different industrial applications, such as in oil industry problems, cosmetics, food products, or in biological fluid problems, such as hemodynamics (DONG *et al.*, 2012; BIRD; ARMSTRONG; HASSAGER, 1987). These materials can simultaneously present many different characteristics such as viscosity, elasticity, plasticity, thixotropy, among others. Therefore, these materials are often classified as "complex materials", since many combinations of these effects can be observed in the same material according to the flow regime to which it is subject to.

More specifically, viscoplastic materials are those that can exhibit both plastic and viscous behaviour. Their main characteristic is the presence of a yield-stress τ_0, which makes the material behave as a rigid solid if the internal stress is below τ_0 or as a viscous fluid if above. Viscoplastic fluids do not exhibit elastic behaviour, which means their stress and viscosity is simply determined by the current deformation rate, without any dependence on flow history. Two common mathematical descriptions for these types of fluids are the Bingham model (BINGHAM, 1922) and the Herschel-Bulkley model (HERSCHEL; BULKLEY, 1926), the latter assuming that shear-thinning is also present. The flow curves for these models can be seen in figures 1a-b. Viscoplastic materials appear often in applications such as painting, food products, and cosmetics.

Viscoelastic fluids, on the other hand, are those that exhibit only viscous and elastic properties. They are known for their ability to store and dissipate energy over time. Unlike Newtonian and common viscoplastic fluids, viscoelastic ones have a viscosity that depends on the flow history, as opposed to simply depending on the current deformation rate. Due to this, they are often characterized by their elastic storage modulus G', as shown in figure 1c, which can be estimated from oscillatory strain sweep tests. Understanding the rheological behaviour of these fluids is important in many areas of industry, such as polymer processing, cosmetics and biomedical engineering. Some common mathematical models to describe viscoelastic fluids include the Oldroyd-B and Phan-Thien-Tanner models (OLDROYD, 1950; THIEN; TANNER,

1977).

In reality, many materials actually present plastic, elastic and viscous behaviour at the same time, these are classified as elastoviscoplastic materials. In some cases one of these properties is less influential than the others and may be ignored, giving rise to the simpler viscoplastic and viscoelastic models mentioned previously. Common EVP materials behave as a viscoelastic fluid below the yield-stress and, above the yield-stress, their elastic modulus may abruptly decrease if a rigid solid is obtained. This is also illustrated in figure 1c. Even more complexity is needed for some materials in which thixotropy is also present. In these cases the viscosity also presents its own time-dependence, and does not instantaneously adapts to changes in the deformation rate.

Due to the high complexity in the mathematical modelling of these materials, some researchers have used specific governing equations to start with, and later included other effects in order to capture the combination of these rheological properties. For example, in the works of Saramito (SARAMITO, 2007; SARAMITO, 2009), viscoplastic models were combined with the constitutive equations of the Oldroyd-B viscoelastic model; while in the works of Souza Mendes (MENDES, 2009; MENDES, 2011), a viscoelastic model was used as a starting point to incorporate the viscoplastic and thixotropic effects. In (DULLAERT; MEWIS, 2006; MEWIS; WAGNER, 2009), the strategy used was to begin the modelling as a material initially viscoplastic, and then add elasticity and thixotropy. Recently, a more generalized model to handle complex fluids was presented in (DIMITRIOU; MCKINLEY, 2018). More details about these complex models can be seen in (MENDES; THOMPSON, 2013; BALMFORTH; FRIGAARD; OVARLEZ, 2014; FRAGGEDAKIS; DIMAKOPOULOS; TSAMOPOULOS, 2016).

In nature and industrial problems, these complex materials often appear in small-scale shapes in which a moving interface can be present. Some of these situations include droplets of polymeric sprays in plants (XU *et al.*, 2021), droplets of 3D-printing systems (DERBY, 2010) or bubbles in non-Newtonian mediums (GONNERMANN; MANGA, 2007), as illustrated in figure 2. In these situations an additional modelling challenge appears: the presence of important surface tension effects.

A fundamental tool in comprehending the modelling of complex materials is computational simulations, since these allow the analysis of rheological properties in different types of flows, such as viscometric flows, purely shearing or purely elongational flows, or also problems that combine these different types. Some numerical results for elastoviscoplastic materials were presented in the works of (CHEDDADI; SARAMITO, 2013; SANTOS *et al.*, 2014) and, more recently in (MITSOULIS; TSAMOPOULOS, 2017; SARAMITO; WACHS, 2017). Adding thixotropy to the mathematical models is still a very recent topic to the community of computational methods and, therefore, there are few works that have achieved success in these simulations, such as in (LINK *et al.*, 2015; LÓPEZ-AGUILAR *et al.*, 2015; LÓPEZ-AGUILAR *et al.*, 2016) and more recently in (LÓPEZ-AGUILAR *et al.*, 2018).

Figure 1 – Rheological curves for some types of fluids covered in this thesis. a) Stress versus strain rate flow curves. b) Viscosity curves as a function of the strain rate. c) Elastic storage modulus as a function of the strain.

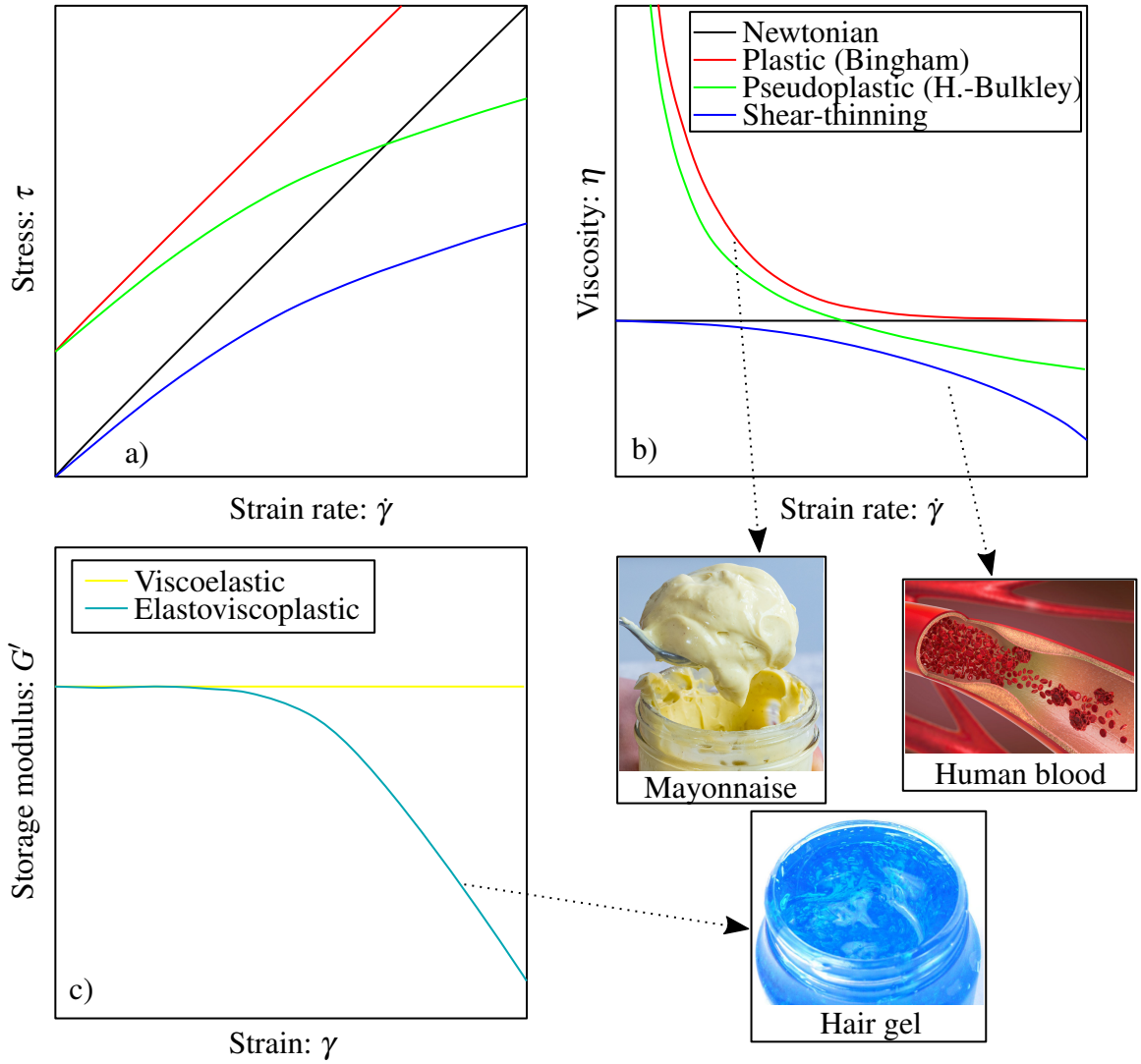

Source: Rheology curves elaborated by the author. Photographs from <https://cleanfoodcrush.com/delicious-creamy-homemade-mayonnaise>, <https://www.heart.org/en/news/2021/12/09/low-level-toxic-metal-exposure-may-raise-the-risk-for-clogged-arteries> and <https://www.belgraviacentre.com/blog/is-leaving-hair-gel-in-overnight-making-my-hair-thin>.

While viscoelastic fluid models have been studied for decades, there is still much room for improvement and further study in this field. In (DATTA *et al.*, 2022) the authors provide a perspective on current open questions related to elastic instabilities. They mention that current popular models such as Oldoryd-B or PTT can fail to quantitatively predict real-life behaviour in the high Weissenberg range where instabilities are seen.

Another topic that still contains much room for further numerical studies is the usage of these complex models in flows with moving interfaces and surface tension effects. In the

Figure 2 – Examples of applications in which the study of complex materials with moving interfaces is of importance. a) Droplets sitting on a leaf. b) Bubble bursting in a volcanic magma medium. c) Inkjet Drop-On-Demand printing system.

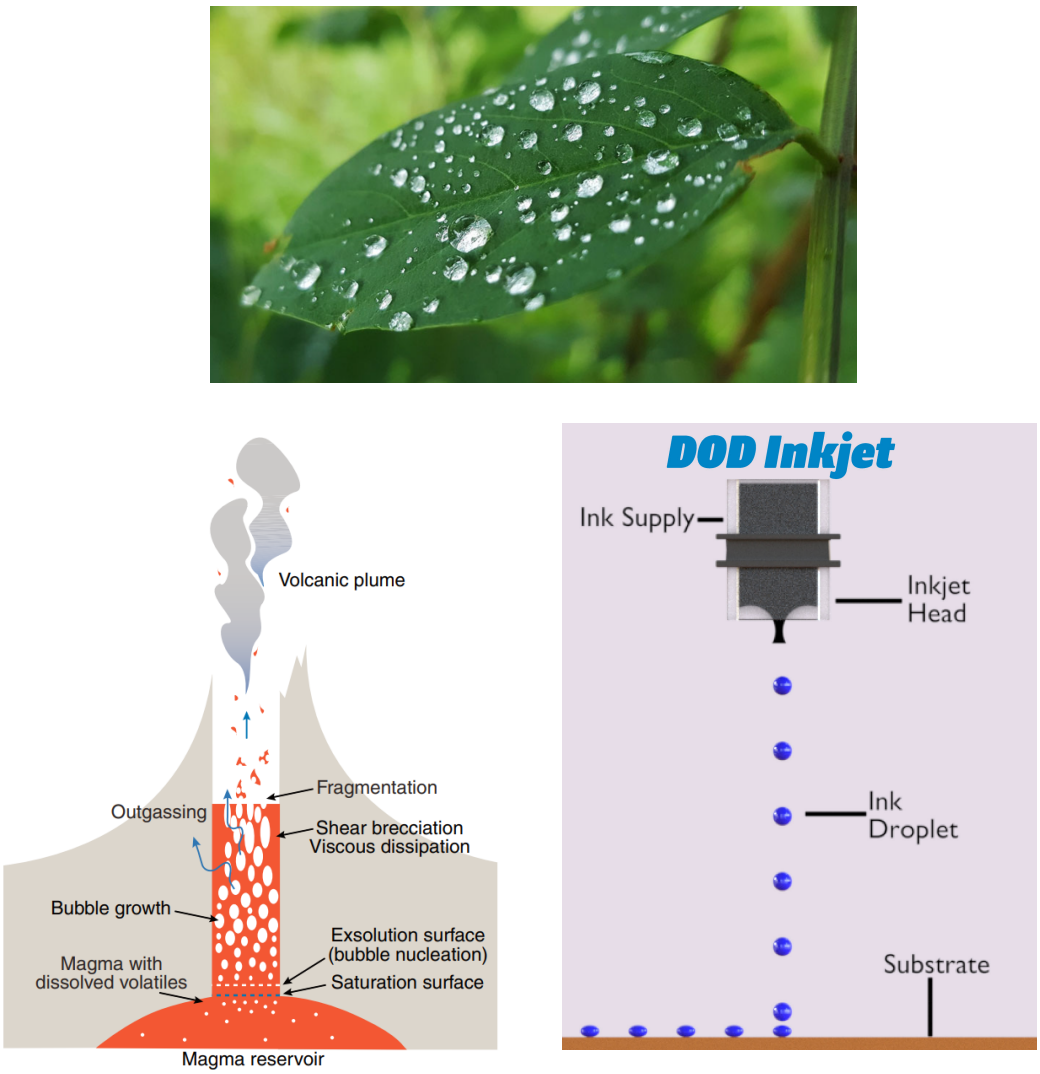

Source: Adapted from <https://www.insidescience.org/news/making-smaller-splashes-pesticides>, (GONNERMANN; MANGA, 2007) and <https://www.aaebv.com/news/inkjet-a-flexible-printing-strategy-for-high-quality-print-unique-part-identification-and-batch-customization/>.

context of free surface flows, it is worth mentioning the recent works of (OISHI; THOMPSON; MARTINS, 2016; OISHI; MARTINS; THOMPSON, 2017), while for multiphase flows, the work of (IZBASSAROV *et al.*, 2018). The recent works developed in the Applied Mathematics and Scientific Computing LAB (LMACC) group still do not cover surface tension effects very extensively in viscoelastic simulations. This can be observed in the papers: (JUNIOR *et al.*, 2016; TOMÉ *et al.*, 2016; TOMÉ *et al.*, 2018). In order to bridge this gap, we have tried to give special attention to studying problems in which the surface tension has an important role. We

also propose a new algorithm to calculate the curvature of an interface using machine learning, which can be useful for surface tension simulations due to their dependency on the curvature.

In chapter 2, we provide an overview of the viscoelastic mathematical modelling and the numerical method that was used in the following chapters of this thesis.

In chapter 3, the natural stress formulation (NSF) is investigated in order to represent the stress tensor using a non-Cartesian basis. By using a basis that follows the flow streamlines, we numerically show that we can obtain better asymptoptic behaviour for the flow properties near geometrical singularities. We perform viscoelastic simulations in a channel with a contraction geometry, and the results show that the NSF is able to provide better accuracy around the contraction corners when compared to the more traditional Cartesian formulation.

In chapter 4, we focus on simulations that present moving surfaces with topological changes. These changes can be generally classified in two types: fluid breakup or fluid coalescence. The test problem chosen for these simulations is the binary droplet collision, since both types of topological changes can happen here. We observe that the implemented algorithm is able to simulate both cases, although some numerical parameters still need to be manually tuned. By adopting the PTT viscoelastic model, we are able to create regime maps to study how the material and flow properties can affect the final result of binary droplet collisions. As we vary the Weissenberg number and the PTT ε parameter, we observe that elasticity and shear-thinning can greatly influence this outcome.

In chapter 5, we maintain our focus on surface tension effects by proposing a new algorithm based on machine learning to calculate the curvature of 2D Front-Tracking interfaces. After detailing the technique, we validate our algorithm with simple shapes such as circles and sinoids. We finish this chapter by showing that this approach can be successfully used in combination with our Front-Tracking flow solver to capture the necessary surface tension effects in binary droplet collision simulations.

In chapter 6 we finish our work by studying rheology models that also include a yield-stress in the material. In particular, we use the Saramito's model to analyse the spreading of an elastoviscoplastic droplet. This complex model describes a material that can transition from an elastic solid to an elastic fluid depending on the stress being imposed. The interactions between surface tension, viscosity, elasticity and plasticity can create interesting behaviour, which are studied in this thesis for the spreading of a droplet.

The work presented in chapters 3, 4 and 5 were respectively published in the following articles:

- Evans, J.D.; França, H.L.; Junior, I.P.; Oishi, C.M. Testing viscoelastic numerical schemes using the Oldroyd-B fluid in Newtonian kinematics. Applied Mathematics and Computation, v. 387, p. 125106, 2020.

- França, H.L.; Oishi, C.M.; Thompson, R.L. Numerical investigation of shear-thinning and viscoelastic binary droplet collision. Journal of Non-Newtonian Fluid Mechanics, v. 302, p. 104750, 2022.
- França, H.L.; Oishi, C.M. A machine learning strategy for computing interface curvature in Front-Tracking methods. Journal of Computational Physics, v. 450, p. 110860, 2022.

The work presented in chapter 6 will be submitted as an article that is currently in preparation. The tentative information for this article is:

- França, H.L.; Jalaal, M.; Oishi, C.M. Spreading of elastoviscoplastic droplets. In preparation.

CHAPTER

2

MATHEMATICAL MODEL

2.1 Governing equations

The governing equations for isothermal incompressible flow, are the continuity and momentum equations

$$\rho\left(\frac{\partial \mathbf{u}}{\partial t}+\nabla\cdot(\mathbf{uu})\right)=-\nabla p+\nabla\cdot\boldsymbol{\tau}+\rho\mathbf{g}, \tag{2.1}$$

$$\nabla\cdot\mathbf{u}=0, \tag{2.2}$$

where $\mathbf{u}$ and p are the velocity and pressure fields, respectively, ρ is the fluid density and $\mathbf{g}$ is a source term (usually gravity). The extra-stress tensor $\boldsymbol{\tau}$ is composed of solvent $\boldsymbol{\tau}^s$ and polymer $\boldsymbol{\tau}^p$ contributions, being written as

$$\boldsymbol{\tau}=\boldsymbol{\tau}^s+\boldsymbol{\tau}^p. \tag{2.3}$$

The solvent contribution represents the Newtonian behaviour of the fluid and is given by

$$\boldsymbol{\tau}^s=2\eta_s\mathbf{D}, \tag{2.4}$$

where η_s is the solvent viscosity and $\mathbf{D}=\frac{1}{2}\left(\nabla\mathbf{u}+(\nabla\mathbf{u})^T\right)$ is the rate-of-strain tensor. For polymeric fluids, the term $\boldsymbol{\tau}^p$ represents the non-Newtonian contribution in the flow which is often modelled by a hyperbolic constitutive equation. In particular, if the Oldroyd-B or Phan-Thien-Tanner (PTT) model is adopted, the constitutive equation is

$$\boldsymbol{\tau}^p+\lambda_p\left(\overset{\triangledown}{\boldsymbol{\tau}}^p+\frac{\varepsilon}{\eta_p}\mathrm{tr}(\boldsymbol{\tau}^p)\boldsymbol{\tau}^p\right)=2\eta_p\mathbf{D}, \tag{2.5}$$

where λ_p is the relaxation time, η_p is the polymer viscosity and ε is a parameter associated with the PTT model ($\varepsilon=0$ in the Oldroyd-B case). The upper-convected derivative $\overset{\triangledown}{\boldsymbol{\tau}}^p$ is defined as

$$\overset{\triangledown}{\boldsymbol{\tau}}^p=\frac{\partial\boldsymbol{\tau}^p}{\partial t}+(\mathbf{u}\cdot\nabla)\,\boldsymbol{\tau}^p-(\nabla\mathbf{u})\boldsymbol{\tau}^p-\boldsymbol{\tau}^p(\nabla\mathbf{u})^T. \tag{2.6}$$

A non-dimensionalization can be performed by scaling the variables as follows

$$\mathbf{x} = L\bar{\mathbf{x}}, \quad t = \frac{L}{U}\bar{t}, \quad \mathbf{u} = U\bar{\mathbf{u}}, \quad p = \rho U^2 \bar{p}, \quad \boldsymbol{\tau}^p = \frac{\eta_0 U}{L}\bar{\mathbf{T}}, \quad \mathbf{g} = g_0\bar{\mathbf{g}}, \tag{2.7}$$

using U and L as characteristic velocity and length, respectively, g_0 as a characteristic source term, and the total viscosity $\eta_0 = \eta_s + \eta_p$.

Removing, for convenience, the bars in (2.7), the non-dimensional governing equations for isothermal incompressible flows of Oldroyd-B fluids are given by

$$\frac{\partial \mathbf{u}}{\partial t} + \nabla\cdot(\mathbf{uu}) = -\nabla p + \frac{\beta}{Re}\nabla^2\mathbf{u} + \frac{1}{Re}\nabla\cdot\mathbf{T} + \frac{1}{Fr^2}\mathbf{g}, \tag{2.8}$$

$$\nabla\cdot\mathbf{u} = 0, \tag{2.9}$$

$$\mathbf{T} + Wi\left(\frac{\partial \mathbf{T}}{\partial t} + (\mathbf{u}\cdot\nabla)\mathbf{T} - (\nabla\mathbf{u})\mathbf{T} - \mathbf{T}(\nabla\mathbf{u})^T + \frac{\varepsilon}{(1-\beta)}\mathrm{tr}(\mathbf{T})\mathbf{T}\right) = 2(1-\beta)\mathbf{D}, \tag{2.10}$$

with non-dimensional groups: Reynolds number (Re), Weissenberg number (Wi), Froude number (Fr) and viscosity ratio ($\beta \in (0,1]$) defined as

$$Re = \frac{\rho UL}{\eta_0}, \quad Wi = \frac{\lambda_p U}{L}, \quad Fr = \frac{U}{\sqrt{g_0 L}}, \quad \beta = \frac{\eta_s}{\eta_0}. \tag{2.11}$$

Considering a 2D cartesian coordinate system, equations (2.8)-(2.10) can be rewritten as

$$\frac{\partial u}{\partial t} + \frac{\partial (uu)}{\partial x} + \frac{\partial (uv)}{\partial y} = -\frac{\partial p}{\partial x} + \frac{\beta}{Re}\left(\frac{\partial^2 u}{\partial x^2} + \frac{\partial^2 u}{\partial y^2}\right) + \frac{1}{Re}\left(\frac{\partial T^{xx}}{\partial x} + \frac{\partial T^{xy}}{\partial y}\right) + \frac{1}{Fr^2}g_x, \tag{2.12}$$

$$\frac{\partial v}{\partial t} + \frac{\partial (uv)}{\partial x} + \frac{\partial (vv)}{\partial y} = -\frac{\partial p}{\partial y} + \frac{\beta}{Re}\left(\frac{\partial^2 v}{\partial x^2} + \frac{\partial^2 v}{\partial y^2}\right) + \frac{1}{Re}\left(\frac{\partial T^{xy}}{\partial x} + \frac{\partial T^{yy}}{\partial y}\right) + \frac{1}{Fr^2}g_y, \tag{2.13}$$

$$\frac{\partial u}{\partial x} + \frac{\partial u}{\partial y} = 0. \tag{2.14}$$

$$T^{xx} + Wi\left(\frac{\partial T^{xx}}{\partial t} + \frac{\partial (uT^{xx})}{\partial x} + \frac{\partial (vT^{xx})}{\partial y} - 2\frac{\partial u}{\partial x}T^{xx} - 2\frac{\partial u}{\partial y}T^{xy} + \frac{\varepsilon}{(1-\beta)}(T^{xx}+T^{yy})T^{xx}\right) = 2(1-\beta)\frac{\partial u}{\partial x}, \tag{2.15}$$

$$T^{yy} + Wi\left(\frac{\partial T^{yy}}{\partial t} + \frac{\partial (uT^{yy})}{\partial x} + \frac{\partial (vT^{yy})}{\partial y} - 2\frac{\partial v}{\partial x}T^{xy} - 2\frac{\partial v}{\partial y}T^{yy} + \frac{\varepsilon}{(1-\beta)}(T^{xx}+T^{yy})T^{yy}\right) = 2(1-\beta)\frac{\partial v}{\partial y}, \tag{2.16}$$

$$T^{xy} + Wi\left(\frac{\partial T^{xy}}{\partial t} + \frac{\partial (uT^{xy})}{\partial x} + \frac{\partial (vT^{xy})}{\partial y} - \frac{\partial v}{\partial x}T^{xx} - \frac{\partial u}{\partial y}T^{yy} + \frac{\varepsilon}{(1-\beta)}(T^{xx}+T^{yy})T^{xy}\right) = (1-\beta)\left(\frac{\partial u}{\partial y} + \frac{\partial v}{\partial x}\right), \tag{2.17}$$

where $\mathbf{T} = T^{xx}\mathbf{i}\mathbf{i}^t + T^{xy}\left(\mathbf{i}\mathbf{j}^t + \mathbf{j}\mathbf{i}^t\right) + T^{yy}\mathbf{j}\mathbf{j}^t$, in which $\mathbf{i}$ and $\mathbf{j}$ are the standard basis vectors. When the fluid is Newtonian ($\beta = 1$), the tensor $\mathbf{T}$ is zero, such that equations (2.12)-(2.14) are the only ones that require solving.

2.2 Natural stress formulation

The most common formulation used to construct the component equations for the constitutive equation (2.10) is based upon the Cartesian decomposition of the tensor $\mathbf{T}$, i.e.

$$\mathbf{T} = T^{xx}\mathbf{i}\mathbf{i}^t + T^{xy}\left(\mathbf{i}\mathbf{j}^t + \mathbf{j}\mathbf{i}^t\right) + T^{yy}\mathbf{j}\mathbf{j}^t, \tag{2.18}$$

where **i** and **j** are unit vectors in fixed Cartesian x and y directions. In this framework, the component form of the polymer constitutive equation (2.10) for the Cartesian polymer extra-stresses T^{xx}, T^{xy}, T^{yy} is given by equations (2.15)-(2.17).

In computational rheology this Cartesian stress formulation (CSF) is widely used by many authors to construct in-house codes (OISHI *et al.*, 2011; AFONSO *et al.*, 2011) and open free codes (PIMENTA; ALVES, 2017; ARAÚJO *et al.*, 2018).

An alternative formulation is to use the streamlines to construct the constitutive equations of the polymer extra-stresses as proposed by Renardy (RENARDY, 1994) and earlier researchers (DUPONT; MARCHAL; CROCHET, 1985). This natural stress formulation (NSF) uses the velocity field and a suitable orthogonal vector to span the polymer extra-stress field as follows

$$\mathbf{T}^p = \frac{(1-\beta)}{\mathrm{Wi}}\left(-\mathbf{I} + \lambda \mathbf{v}\mathbf{v}^T + \mu(\mathbf{v}\mathbf{w}^T + \mathbf{w}\mathbf{v}^T) + \nu \mathbf{w}\mathbf{w}^T\right), \tag{2.19}$$

with

$$\mathbf{w} = \frac{1}{|\mathbf{v}|^2}(-v\mathbf{i} + u\mathbf{j}).$$

In order to obtain the component equations for variables λ, μ and ν it is convenient to perform the following scaling

$$\hat{\lambda} = |\mathbf{v}|^2\lambda, \quad \hat{\mu} = \mu, \quad \hat{\nu} = \frac{\nu}{|\mathbf{v}|^2}. \tag{2.20}$$

Substituting (2.19) and (2.20) into (2.15)-(2.17) the new component equations take the form

$$\left[\frac{\partial \hat{\lambda}}{\partial t} + \frac{2\hat{\mu}}{|\mathbf{u}|^2}\left(v\frac{\partial u}{\partial t} - u\frac{\partial v}{\partial t}\right) + |\mathbf{u}|^2(\mathbf{u}\cdot\nabla)\left(\frac{\hat{\lambda}}{|\mathbf{u}|^2}\right) + 2\hat{\mu}|\mathbf{u}|^2\nabla\cdot\mathbf{w}\right] + \frac{1}{\mathrm{Wi}}\left(\hat{\lambda} - 1\right) = 0, \tag{2.21}$$

$$\left[\frac{\partial \hat{\mu}}{\partial t} + \left(\frac{\hat{\lambda} - \hat{\nu}}{|\mathbf{u}|^2}\right)\left(u\frac{\partial v}{\partial t} - v\frac{\partial u}{\partial t}\right) + (\mathbf{u}\cdot\nabla)\hat{\mu} + \hat{\nu}|\mathbf{u}|^2\nabla\cdot\mathbf{w}\right] + \frac{\hat{\mu}}{\mathrm{Wi}} = 0, \tag{2.22}$$

$$\left[\frac{\partial \hat{\nu}}{\partial t} + \frac{2\hat{\mu}}{|\mathbf{u}|^2}\left(u\frac{\partial v}{\partial t} - v\frac{\partial u}{\partial t}\right) + \frac{1}{|\mathbf{u}|^2}(\mathbf{u}\cdot\nabla)\left(\hat{\nu}|\mathbf{u}|^2\right)\right] + \frac{1}{\mathrm{Wi}}(\hat{\nu} - 1) = 0, \tag{2.23}$$

where

$$|\mathbf{u}|^2\nabla\cdot\mathbf{w} = \frac{1}{|\mathbf{u}|^2}\left[(v^2 - u^2)\left(\frac{\partial v}{\partial x} + \frac{\partial u}{\partial y}\right) + 4uv\frac{\partial u}{\partial x}\right]. \tag{2.24}$$

The natural stress variables $(\hat{\lambda}, \hat{\mu}, \hat{\nu})$ are related to the cartesian stresses (T^{xx}, T^{xy}, T^{yy}) by the equations

$$T^{xx} = \frac{(1-\beta)}{Wi}\left[-1 + \frac{1}{|\mathbf{u}|^2}\left(\hat{\lambda}u^2 - 2\hat{\mu}uv + \hat{\nu}v^2\right)\right], \tag{2.25}$$

$$T^{xy} = \frac{(1-\beta)}{Wi}\left[\hat{\lambda}uv + \hat{\mu}(u^2 - v^2) - \hat{\nu}uv\right], \tag{2.26}$$

$$T^{yy} = \frac{(1-\beta)}{Wi}\left[-1 + \frac{1}{|\mathbf{u}|^2}\left(\hat{\lambda}v^2 + 2\hat{\mu}uv + \hat{\nu}u^2\right)\right]. \tag{2.27}$$

Therefore, to model a viscoelastic flow using the natural stress formulation (NSF), we combine the conservation equations (2.8)-(2.9) with the NSF constitutive equations (2.21)-(2.23). When needed, the cartesian stresses can be obtained from the relations (2.25)-(2.27).

2.3 Boundary conditions

To guarantee a unique solution, the Navier-Stokes equations also require appropriate boundary conditions. In this section we describe all the boundary conditions used throughout out work.

2.3.1 Solid walls

Solid walls are modelled here by the *no-slip* condition, given by equations

$$\begin{cases} u_n = 0, \\ u_m = u_f, \end{cases} \tag{2.28}$$

where u_n is the velocity component perpendicular to the wall, u_m is the component tangent to the wall.

2.3.2 Inflow

When fluid is entering the domain, the flow velocity at this inflow boundary is given. Therefore, the condition at this boundary is modeled by equations

$$\begin{cases} u_n = u_i, \\ u_m = 0, \end{cases} \tag{2.29}$$

where u_i is a given inflow velocity.

The inflow conditions for $\mathbf{T}$ are obtained considering a fully developed flow inside a channel. In a flow that happens in the x direction, for example, they are given by

$$T^{xx} = 2(1-\beta)Wi\left(\frac{\partial u}{\partial y}\right)^2, \qquad T^{xy} = (1-\beta)\left(\frac{\partial u}{\partial y}\right), \qquad T^{yy} = 0. \tag{2.30}$$

Analogously, the inflow conditions for the NSF variables λ, μ e ν are

$$\hat{\lambda} = \frac{Wi}{(1-\beta)}T^{xx} + 1, \qquad \hat{\mu} = \frac{Wi}{(1-\beta)}T^{xy}, \qquad \hat{\nu} = \frac{Wi}{(1-\beta)}T^{yy} + 1. \tag{2.31}$$

2.3.3 Outflow

When a fluid is leaving the computational domain, we assume that this happens spontaneously, that is, there are no outside forces "pulling" it. This is modeled by the homogeneous Neumann conditions

$$\begin{cases} \dfrac{\partial u_n}{\partial \mathbf{n}} = 0, \\ \dfrac{\partial u_m}{\partial \mathbf{n}} = 0, \\ \dfrac{\partial \mathbf{T}}{\partial \mathbf{n}} = \mathbf{0}, \end{cases} \tag{2.32}$$

where $\mathbf{n}$ is the vector normal to the boundary.

2.3.4 Symmetry

A symmetry boundary condition is sometimes used in 2D simulations that present a symmetric behaviour around an axis. This is very useful since it cuts the geometry in half, greatly reducing the computational cost for the simulation. On these boundaries, we impose the following conditions

$$\begin{cases} u_n = 0, \\ \dfrac{\partial u_m}{\partial \mathbf{n}} = 0. \end{cases} \tag{2.33}$$

2.3.5 Free surface

In free surface flows, that is, flows in which there is direct contact between the fluid and the outside environment (air), we apply conditions directly on this free boundary. These conditions are modeled by the normal and tangential stress equations, given, respectively, by

$$\mathbf{n} \cdot (\boldsymbol{\sigma} \cdot \mathbf{n}) = \gamma \kappa, \tag{2.34}$$

$$\mathbf{m} \cdot (\boldsymbol{\sigma} \cdot \mathbf{n}) = 0, \tag{2.35}$$

where $\mathbf{n}$ is the normal vector to the free surface, $\mathbf{m}$ is the tangential vector, γ is the surface tension coefficient, κ is the surface curvature, while the total stress tensor $\boldsymbol{\sigma}$ is

$$\boldsymbol{\sigma} = \boldsymbol{\tau} - p\mathbf{I} = 2\eta_s \mathbf{D} + \boldsymbol{\tau}^p - p\mathbf{I}. \tag{2.36}$$

We non-dimensionalize equations (2.34)-(2.35) using the same characteristic values as in (2.7), along with

$$\kappa = \frac{1}{L}\bar{\kappa}. \tag{2.37}$$

This way, equations (2.34)-(2.35) become

$$\mathbf{n} \cdot (\bar{\boldsymbol{\sigma}} \cdot \mathbf{n}) = \frac{1}{We}\bar{\kappa}, \tag{2.38}$$

$$\mathbf{m} \cdot (\bar{\boldsymbol{\sigma}} \cdot \mathbf{n}) = 0, \tag{2.39}$$

where

$$\bar{\boldsymbol{\sigma}} = 2\beta \bar{\mathbf{D}} + \bar{\mathbf{T}} - Re \cdot \bar{p}\mathbf{I}, \tag{2.40}$$

and We is the Weber number, given by

$$We = \frac{\rho U^2 L}{\gamma}. \tag{2.41}$$

From now on, the upper bars used for the non-dimensional variables will be dropped.

In cartesian coordinates, equations (2.38) and (2.39) are respectively written as

$$p = \frac{2\beta}{Re}\left[n_x^2 \frac{\partial u}{\partial x} + n_x n_y \left(\frac{\partial u}{\partial y} + \frac{\partial v}{\partial x}\right) + n_y^2 \frac{\partial v}{\partial y}\right] + \frac{1}{Re}\left[n_x^2 T^{xx} + 2n_x n_y T^{xy} + n_y^2 T^{yy}\right] + \frac{1}{We}\kappa, \tag{2.42}$$

$$\beta\left[2n_x n_y \left(\frac{\partial v}{\partial y} - \frac{\partial u}{\partial x}\right) + (n_x^2 - n_y^2)\left(\frac{\partial v}{\partial x} + \frac{\partial u}{\partial y}\right)\right] = n_x n_y (T^{xx} - T^{yy}) + (n_y^2 - n_x^2) T^{xy}, \tag{2.43}$$

where $\mathbf{n} = (n_x, n_y)$ is the unit outward normal vector to the fluid domain.

When the flow is considered purely Newtonian, the tensor $\mathbf{T}$ is always null, so that all its components can be removed in equations (2.42)-(2.43).

2.4 Overview of the numerical method

2.4.1 Projection method

In chapters 3, 4 and 5 of this work, the Navier-Stokes equations are solved numerically using an in-house code based on the well-known projection method. In summary, this method uses the Helmhotz-Hodge decomposition to decouple velocity and pressure from equations (2.8)-(2.9).

The Helmhotz-Hodge decomposition (CHORIN; MARSDEN, 1979) states that any vector field defined in a region Ω with smooth boundary $\partial\Omega$ can be uniquely decomposed as

$$\tilde{\mathbf{u}} = \mathbf{u} + \nabla\psi, \tag{2.44}$$

where $\mathbf{u}$ is a vector field such that $\nabla \cdot \mathbf{u} = 0$ and ψ a scalar field also defined in Ω.

The first step in the projection method is to solve the momentum equation (2.8) for an intermediate velocity field $\tilde{\mathbf{u}}$. In order to decouple velocity and pressure, we approximate the unknown p by some known scalar field $\tilde{p}$, which will be discussed further. The equation then becomes

$$\frac{\partial \tilde{\mathbf{u}}}{\partial t} + \nabla \cdot (\tilde{\mathbf{u}}\tilde{\mathbf{u}}) = -\nabla\tilde{p} + \frac{\beta}{Re}\nabla^2\tilde{\mathbf{u}} + \frac{1}{Re}\nabla \cdot \mathbf{T} + \frac{1}{Fr^2}\mathbf{g}, \tag{2.45}$$

where, for non-Newtonian flows, the tensor $\mathbf{T}$ is also assumed to be known.

Solving (2.45), we obtain a velocity field $\tilde{\mathbf{u}}$ for which, in general, the continuity equation is not yet satisfied. Using the Helmhotz-Hodge decomposition (2.44) and the continuity equation (2.9) we can create a Poisson equation for ψ:

$$\nabla^2\psi = \nabla \cdot \tilde{\mathbf{u}}. \tag{2.46}$$

After solving equations (2.45) and (2.46) we have both $\tilde{\mathbf{u}}$ and ψ, such that the Helmhotz-Hodge decomposition (2.44) can be used to obtain the final velocity field $\mathbf{u}$ that also satisfies the continuity equation.

2.4.2 Spatial discretization

The domain is discretized using a regular non-uniform mesh. Points $x_0, x_1, \ldots, x_{N_x}$ are chosen to discretize the x direction, while $y_0, y_1, \ldots, y_{N_y}$ are chosen for the y direction. These points result in a mesh with $N_x \times N_y$ cells with spacings

$$\Delta_{x_i} = x_i - x_{i-1}, \;\; i = 1, 2, \ldots, N_x \;\; \text{and} \tag{2.47}$$

$$\Delta_{y_j} = y_j - y_{j-1}, \;\; j = 1, 2, \ldots, N_y. \tag{2.48}$$

Let $\mathbf{x}_{i,j}$ be the point at the center of cell (i, j), that is

$$\mathbf{x}_{i,j} = \left(x_i + \frac{1}{2}\Delta_{x_i},\ y_j + \frac{1}{2}\Delta_{y_j} \right). \tag{2.49}$$

A staggered grid will be used to evaluate properties in different cell locations:

- p, $\mathbf{T}$, ψ: these properties are evaluated at cell centers $\mathbf{x}_{i,j}$;
- u: the velocity in the x direction is evaluated at vertical cell faces, that is $\mathbf{x}_{i-\frac{1}{2},j}$;
- v: the velocity in the y direction is evaluated at horizontal cell faces, that is $\mathbf{x}_{i,j-\frac{1}{2}}$.

These cell locations are illustrated in Figure 3.

Figure 3 – Computational cell i, j and its points of interest on the staggered grid.

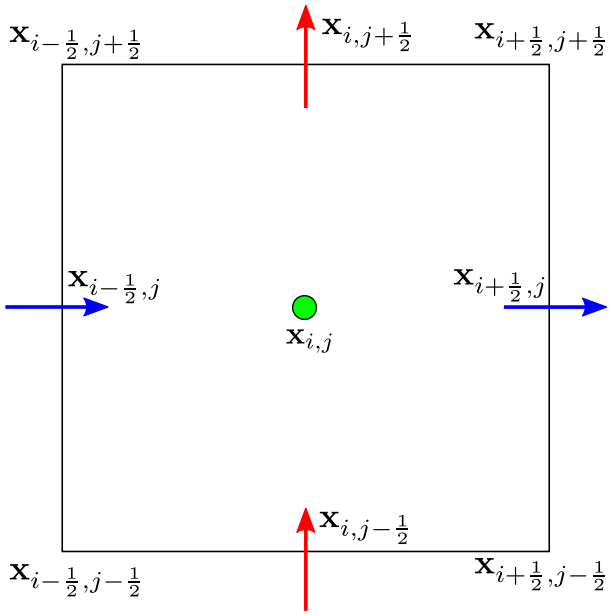

Source: Elaborated by the author.

2.4.3 Cell classification

When performing free surface simulations, the fluid interface is represented explicitly via connected marker particles, according to the Front-Tracking methodology. The grid cells are classified according to their position with respect to the fluid interface. Each cell is classified as one of three possible options:

- EMPTY: a cell receives the EMPTY label if it does not contain any marker particles inside it and is located outside the region with fluid;
- SURFACE: a cell that contains at least one marker particle and that borders an EMPTY cell;

- FULL: these cells do not have EMPTY cells around its four faces, that is, they are inside a region with fluid.

Figure 4 shows a grid example with all its cells classified according to the fluid location. The Front-Tracking representation of the interface can also be seen through the connected marker particles.

Figure 4 – Example of cell classification in a free surface simulation.

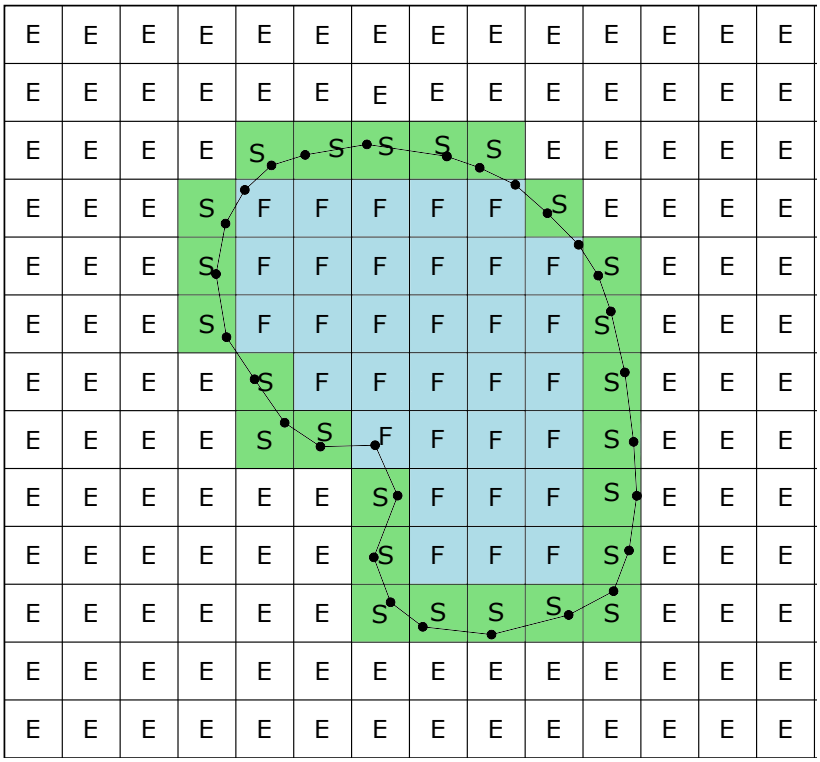

Source: Elaborated by the author.

The cell classification described above will determine which equations are solved in each of the grid points. For points inside FULL cells, for example, the momentum and Poisson equations are solved normally. For points inside EMPTY regions, nothing will be done, since there is no flow happening here. For points around SURFACE cells, the free surface boundary conditions will be used.

When the free surface boundary conditions (2.34)-(2.35) are used, two important interface properties need to be approximated: normal vector and curvature. For the normal vector, a rough approximation will be used according to the classification of neighbor cells. Eight possible normal vectors will be used, and the classifications for each of them are shown in Figure 5.

For the curvature, the marker particles are used to create a least-squares fit of the interface using a parabola. The parabola curvature is then used as an approximation for the curvature of the original interface. This process is described in much more detail in (FRANçA, 2018) (written in portuguese). We have recently also developed a new approach to calculate the curvature using

Figure 5 – Eight cases of possible normal vectors used in the free surface boundary conditions.

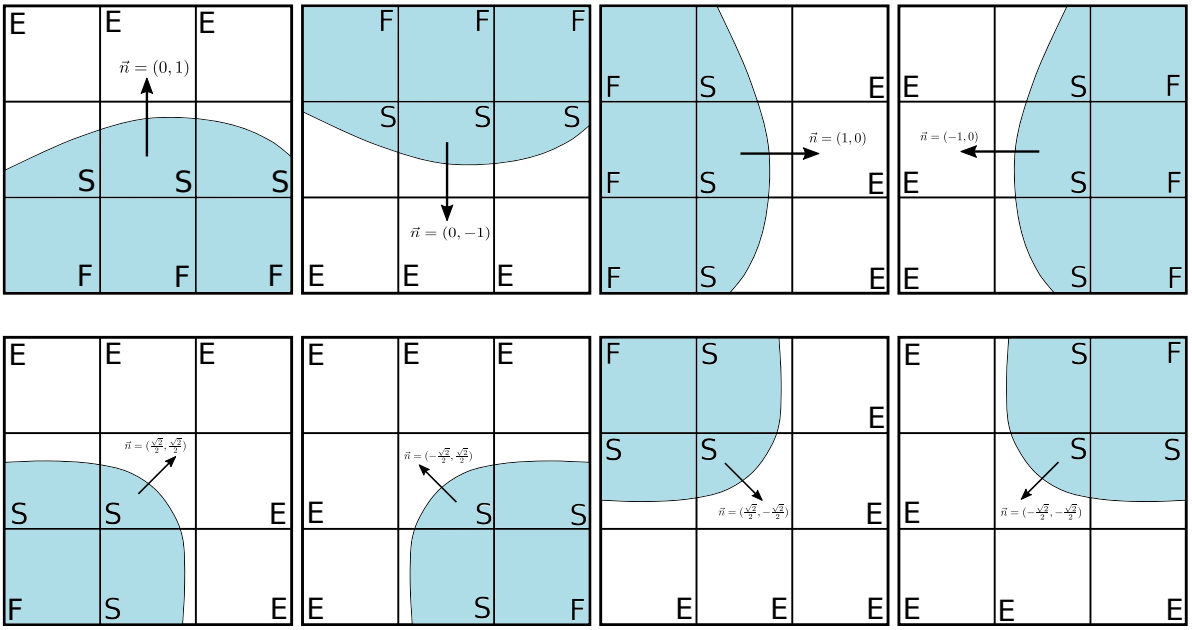

Source: Elaborated by the author.

a machine learning algorithm. A description of this approach and some preliminary results will be presented in section 5.

2.4.4 Time discretization for the momentum equation

Currently, the time discretization is performed by a semi-implicit Euler scheme, that is, the viscous terms in the equation are treated implicitly, while the convective terms are explicit. This way, the discrete version of equation (2.45) becomes

$$\frac{\widetilde{\mathbf{u}}^{n+1} - \mathbf{u}^n}{\Delta_t} + \nabla \cdot (\mathbf{u}\mathbf{u})^n = -\nabla p^n + \frac{\beta}{Re}\nabla^2 \widetilde{\mathbf{u}}^{n+1} + \frac{1}{Re}\nabla \cdot \mathbf{T}^n + \frac{1}{Fr^2}\mathbf{g}^{n+1}. \tag{2.50}$$

2.4.5 Pressure update equation

After the velocity is updated, we need to calculate the new pressure p^{n+1}. In order to to this, consider the momentum equation (2.8) discretized in time, given by

$$\frac{\mathbf{u}^{n+1} - \mathbf{u}^n}{\Delta_t} + \nabla \cdot (\mathbf{u}\mathbf{u})^n = -\nabla p^{n+1} + \frac{\beta}{Re}\nabla^2 \mathbf{u}^{n+1} + \frac{1}{Re}\nabla \cdot \mathbf{T}^n + \frac{1}{Fr^2}\mathbf{g}^{n+1}. \tag{2.51}$$

Substracting (2.50) from (2.51), we get

$$\frac{\mathbf{u}^{n+1} - \widetilde{\mathbf{u}}^{n+1}}{\Delta_t} = -\nabla p^{n+1} + \nabla p^n + \frac{\beta}{Re}\left[\nabla^2 \mathbf{u}^{n+1} - \nabla^2 \widetilde{\mathbf{u}}^{n+1}\right]. \tag{2.52}$$

Finally, substituting $\widetilde{\mathbf{u}}$ in (2.52) by its decomposition (2.44), we obtain the following pressure update formula

$$p^{n+1} = p^n + \frac{\psi}{\Delta_t} - \frac{\beta}{Re}\nabla^2\psi^{n+1}. \tag{2.53}$$

To avoid the necessity to discretize the laplacian operator in (2.53), we neglect this term, as proposed also in (SOUSA; OISHI; BUSCAGLIA, 2015). This way, the pressure update formula is given by

$$p^{n+1} = p^n + \frac{\psi}{\Delta_t}. \tag{2.54}$$

2.4.6 Boundary conditions for the Poisson equation

For the property ψ, according (TOMÉ, 1993) the boundary conditions in solid walls and inflows are

$$\frac{\partial\psi}{\partial\mathbf{n}} = 0, \tag{2.55}$$

and, for outflows,

$$\psi = 0. \tag{2.56}$$

The boundary condition on the free surface is created using equations (2.44), (2.54) and (2.42), according to the implicit methodology proposed in (OISHI *et al.*, 2008). Writing the normal condition (2.42) at time t_{n+1}, we have

$$\begin{aligned} p^{n+1} =& \frac{2\beta}{Re}\left[n_x^2\frac{\partial u^{n+1}}{\partial x} + n_x n_y\left(\frac{\partial u^{n+1}}{\partial y} + \frac{\partial v^{n+1}}{\partial x}\right) + n_y^2\frac{\partial v^{n+1}}{\partial y}\right] + \\ & \frac{1}{Re}\left[n_x^2 T^{xx,n} + 2n_x n_y T^{xy,n} + n_y^2 T^{yy,n}\right] + \frac{1}{We}\kappa, \end{aligned} \tag{2.57}$$

with the stress tensor being explicitly approximated at time n.

Substituting (2.54) in (2.57), we obtain

$$\begin{aligned} p^n + \frac{\psi^{n+1}}{\Delta_t} =& \frac{2\beta}{Re}\left[n_x^2\frac{\partial u^{n+1}}{\partial x} + n_x n_y\left(\frac{\partial u^{n+1}}{\partial y} + \frac{\partial v^{n+1}}{\partial x}\right) + n_y^2\frac{\partial v^{n+1}}{\partial y}\right] + \\ & \frac{1}{Re}\left[n_x^2 T^{xx,n} + 2n_x n_y T^{xy,n} + n_y^2 T^{yy,n}\right] + \frac{1}{We}\kappa. \end{aligned} \tag{2.58}$$

Finally, the velocities are replaced by their Helmhotz-Hodge decomposition (2.44), resulting in

$$\begin{aligned} & p^n + \frac{\psi^{n+1}}{\Delta_t} = \frac{2\beta}{Re}\left[n_x^2\frac{\partial}{\partial x}\left(\tilde{u}^{n+1} - \frac{\partial\psi^{n+1}}{\partial x}\right) + \right. \\ & \left. n_x n_y\left(\frac{\partial}{\partial y}\left(\tilde{u}^{n+1} - \frac{\partial\psi^{n+1}}{\partial x}\right) + \frac{\partial}{\partial x}\left(\tilde{v}^{n+1} - \frac{\partial\psi^{n+1}}{\partial y}\right)\right) + n_y^2\frac{\partial}{\partial y}\left(\tilde{v}^{n+1} - \frac{\partial\psi^{n+1}}{\partial y}\right)\right] + \\ & \frac{1}{Re}\left[n_x^2 T^{xx,n} + 2n_x n_y T^{xy,n} + n_y^2 T^{yy,n}\right] + \frac{1}{We}\kappa. \end{aligned} \tag{2.59}$$

The relation (2.59) is used as boundary condition for the Poisson equation and, in some cases where values of ψ^{n+1} are required outside the domain, we use $\psi^{n+1} = 0$.

2.4.7 Strain tensor update

As described earlier, the strain tensor update is done in our work using two different approaches: the Natural Stress or the Cartesian Stress formulations. We describe the time discretization for both approaches below.

2.4.7.1 Updating via CSF

In this case the strain tensor is updated according to equations (2.15)-(2.17). The time discretization of these equations is performed using the explicit Euler scheme, such that we get

$$T^{xx,n+1} = T^{xx,n} + \Delta_t \cdot F^{xx}_{CSF}, \tag{2.60}$$

$$T^{yy,n+1} = T^{yy,n} + \Delta_t \cdot F^{yy}_{CSF}, \tag{2.61}$$

$$T^{xy,n+1} = T^{xy,n} + \Delta_t \cdot F^{xy}_{CSF}, \tag{2.62}$$

where

$$\begin{aligned} F^{xx}_{CSF} = &- \frac{\partial (u^{n+1} T^{xx,n})}{\partial x} - \frac{\partial (v^{n+1} T^{xx,n})}{\partial y} + 2\frac{\partial u^{n+1}}{\partial x} T^{xx,n} + 2\frac{\partial u^{n+1}}{\partial y} T^{xy,n} + \\ & 2\frac{(1-\beta)}{Wi}\frac{\partial u^{n+1}}{\partial x} - \frac{1}{Wi} T^{xx,n}, \end{aligned} \tag{2.63}$$

$$\begin{aligned} F^{yy}_{CSF} = &- \frac{\partial (u^{n+1} T^{yy,n})}{\partial x} - \frac{\partial (v^{n+1} T^{yy,n})}{\partial y} + 2\frac{\partial v^{n+1}}{\partial x} T^{xy,n} + 2\frac{\partial v^{n+1}}{\partial y} T^{yy,n} + \\ & 2\frac{(1-\beta)}{Wi}\frac{\partial v^{n+1}}{\partial y} - \frac{1}{Wi} T^{yy,n}, \end{aligned} \tag{2.64}$$

$$\begin{aligned} F^{xy}_{CSF} = &- \frac{\partial (u^{n+1} T^{xy,n})}{\partial x} - \frac{\partial (v^{n+1} T^{xy,n})}{\partial y} + \frac{\partial v^{n+1}}{\partial x} T^{xx,n} + \frac{\partial u^{n+1}}{\partial y} T^{yy,n} + \\ & \frac{(1-\beta)}{Wi}\left(\frac{\partial u^{n+1}}{\partial y} + \frac{\partial v^{n+1}}{\partial x}\right) - \frac{1}{Wi} T^{xy,n}. \end{aligned} \tag{2.65}$$

2.4.7.2 Updating via NSF

For this formulation, equations (2.21)-(2.23) are used to update $\hat{\lambda}, \hat{\mu}, \hat{\nu}$. Afterwards, $\mathbf{T}^{n+1}$ is obtained using relations (2.25)-(2.27).

The explicit Euler discretization of the NSF equations (2.21)-(2.23) becomes

$$\hat{\lambda}^{n+1} = \hat{\lambda}^n + \Delta_t \cdot F^{\hat{\lambda}}_{NSF}, \tag{2.66}$$

$$\hat{\mu}^{n+1} = \hat{\mu}^n + \Delta_t \cdot F^{\hat{\mu}}_{NSF}, \tag{2.67}$$

$$\hat{\nu}^{n+1} = \hat{\nu}^n + \Delta_t \cdot F^{\hat{\nu}}_{NSF}, \tag{2.68}$$

where

$$\begin{aligned} F^{\hat{\lambda}}_{NSF} = &- \frac{2\hat{\mu}^n}{(|\mathbf{u}^{n+1}|^2 + tol)}\left(v^{n+1}\frac{\partial u^{n+1}}{\partial t} - u^{n+1}\frac{\partial v^{n+1}}{\partial t}\right) - |\mathbf{u}^{n+1}|^2\left(\frac{\partial (u^{n+1}\lambda^n)}{\partial x} + \frac{\partial (v^{n+1}\lambda^n)}{\partial y}\right) \\ & - 2\hat{\mu}^n |\mathbf{u}^{n+1}|^2 \nabla \cdot \mathbf{w}^{n+1} - \frac{1}{Wi}\left(\hat{\lambda}^n - 1\right), \end{aligned} \tag{2.69}$$

and $\lambda^n = \frac{\hat{\lambda}^n}{(|\mathbf{u}^{n+1}|^2+tol)}$ is used in the convective term;

$$F^{\hat{\mu}}_{NSF} = -\left(\frac{\hat{\lambda}^n - \hat{\nu}^n}{|\mathbf{u}^{n+1}|^2+tol}\right)\left(u^{n+1}\frac{\partial v^{n+1}}{\partial t} - v^{n+1}\frac{\partial u^{n+1}}{\partial t}\right) - \left(\frac{\partial(u^{n+1}\hat{\mu}^n)}{\partial x} + \frac{\partial(v^{n+1}\hat{\mu}^n)}{\partial y}\right) - \hat{\nu}^n|\mathbf{u}^{n+1}|^2\nabla\cdot\mathbf{w}^{n+1} - \frac{\hat{\mu}^n}{Wi}, \tag{2.70}$$

$$F^{\hat{\nu}}_{NSF} = -\frac{2\hat{\mu}^n}{(|\mathbf{u}^{n+1}|^2+tol)}\left(u^{n+1}\frac{\partial v^{n+1}}{\partial t} - v^{n+1}\frac{\partial u^{n+1}}{\partial t}\right) - \frac{1}{(|\mathbf{u}^{n+1}|^2+tol)}\left(\frac{\partial(u^{n+1}\nu^n)}{\partial x} + \frac{\partial(v^{n+1}\nu^n)}{\partial y}\right) - \frac{1}{Wi}(\hat{\nu}^n - 1), \tag{2.71}$$

in which

$$|\mathbf{u}^{n+1}|^2\nabla\cdot\mathbf{w}^{n+1} = \frac{1}{(|\mathbf{u}^{n+1}|^2+tol)}\left[((v^{n+1})^2 - (u^{n+1})^2)\left(\frac{\partial v^{n+1}}{\partial x} + \frac{\partial u^{n+1}}{\partial y}\right) + 4u^{n+1}v^{n+1}\frac{\partial u^{n+1}}{\partial x}\right]. \tag{2.72}$$

Note that a new term tol was added in some denominators from equations (2.66)-(2.68). This is done due to the basis used in (2.19) being degenerate near regions where the velocity field is null (walls or stagnation points, for example). To regularize some terms, a very small constant tol is added to avoid divisions by zero or close-to-zero denominators.

2.4.8 Topological changes in the interface

In this project we are also interested in performing simulations of free surface flows in which the fluid interface undergoes topological changes. These types of changes do not happen naturally in Front-Tracking representations, so an explicit algorithm is required. The algorithm used here is proposed by (GLIMM *et al.*, 1988) and is based on the idea of fixing interfaces that are "tangled". This algorithm is described in detail in the Master's thesis (FRANçA, 2018) (by the same author of this monograph, in portuguese). In this section we will briefly summarize how this topological change algorithm interacts with the MAC method for solving the equations in our code.

As explained in section 2.4.3, the MAC method classifies the grid cells in three categories: EMPTY, FULL and SURFACE. As a quick reminder, SURFACE cells are those in which free surface conditions are applied, and FULL cells are those that do not have any EMPTY cells around itself. Using these classifications, we will now mention how the topological change is performed in the MAC method for two separate cases: coalescence and breakup.

2.4.8.1 Case 1: Coalescence

This case will be illustrated using the example in which two colliding drops are merged into a single block of fluid. Figure 6a shows the initial simulation state, and 6b a more advanced stage when the drops have already met. In both images, blue, grey and red colours represent, respectively, FULL, EMPTY and SURFACE cells.

When marker particles from the different droplets are too close to each other, that is, they are in the same cell or in adjacent cells, the MAC method classifies this region as FULL, since

there are no EMPTY cells in this area. This means that no boundary conditions will be applied here, causing the droplets interfaces to never actually cross each other.

Figure 6c shows a zoomed view of this collision stage (the green points and arrows will be explained shortly). We can see there is a sizeable region containing marker particles, but that does not actually contain any SURFACE cells in it, only FULL. To use the untangling algorithm proposed in (GLIMM *et al.*, 1988), we must force a tangling in this interface to create a topological change.

Whenever we find a region with too many adjacent FULL cells containing marker particles, we interpret that this region is a candidate for the coalescing topological change. To create this change, a tangling is performed according to the following steps:

1. Let A and B be the curves that represent each of the two blocks of fluids, respectively.
2. We iterate over the particles in A that are inside the FULL region, and store the two particles that limit this region. With this, we will have two particles named A_1 and A_2. These are illustrated in Figure 6c.
3. Analogously, we iterate over the curve B and find the particles B_1 and B_2 that limit its FULL region.
4. All particles between A_1 and A_2 will change positions with particles between B_1 and B_2, which tangles the interface as shown in Figure 6d.

After forcing these steps, the general untangling algorithm can be applied and the two blocks of fluids will be merged, as shown in Figure 6e.

2.4.8.2 Case 2: Breakup

We now illustrate the breakup case in a MAC simulation. The example used here will be the impact of a drop on a liquid film causing a splashing effect. Twos stages of this simulation can be seen in Figures 7a and 7b.

Similarly to the coalescence case, the MAC method does not automatically tangles the interface in this case. The curves become extremely close, but never cross each other. Once again, we need to choose some criteria to determine when the interface should be forcefully tangled to create a topological change. Currently, our criteria is simply based on the thickness of a fluid filament. If a body of fluid has a filament with thickness smaller than a chosen threshold, then this area receives a topological change according to the following steps:

1. Two particles A and B are chosen across the width of the filament (see Figure 7c). The distance between these particles needs to be smaller than a chosen threshold.
2. The positions of A and B are swapped, tangling the interface as shown in Figure 7d.

Figure 6 – Illustration of the free surface during the topological change algorithm that coalesces two blocks of fluid.

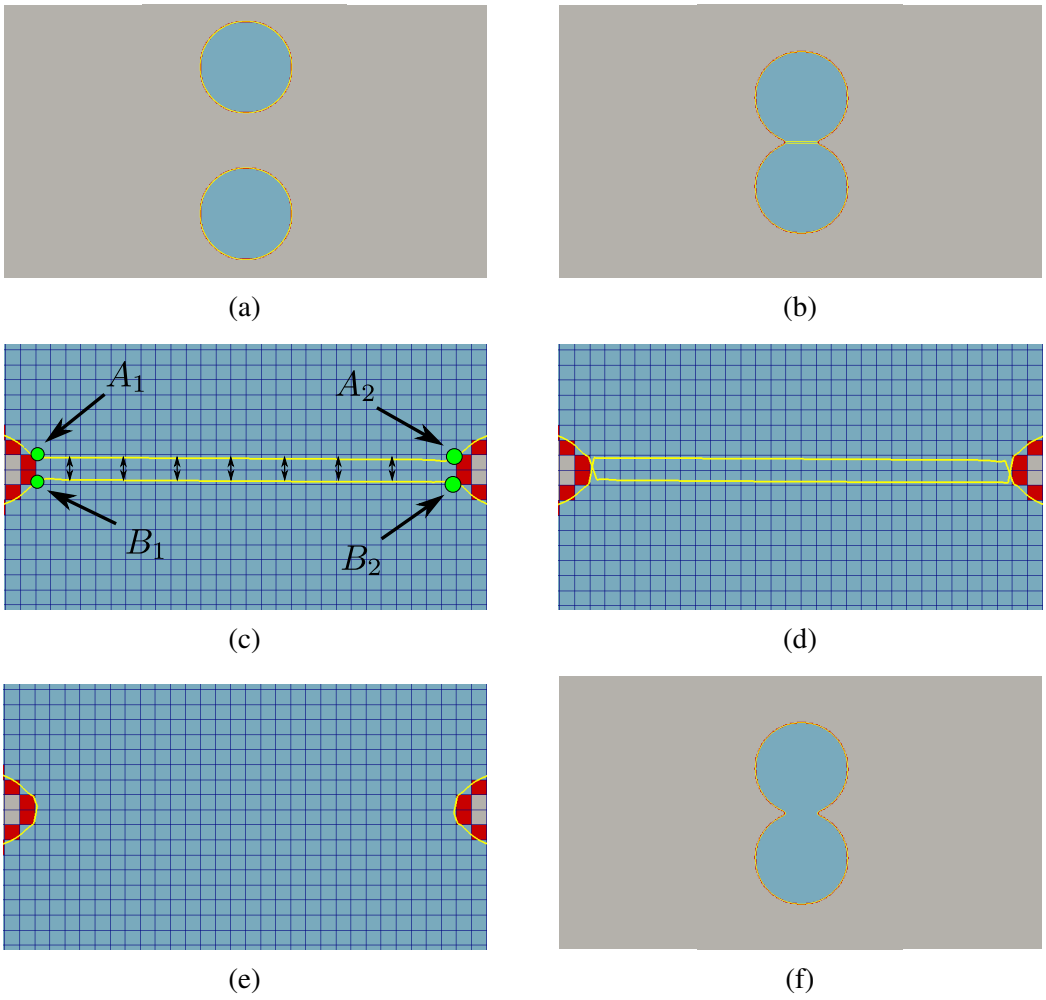

Source: Elaborated by the author.

3. The untangling algorithm is executed, performing the topological change (Figure 7e).

2.4.9 Summarizing

Using all the equations described previously, the projection method used in this work can be summarized in the following steps

1. Calculate the boundary velocity at points around the SURFACE cells using the free surface equations (2.34)-(2.35);
2. Obtain the intermediate velocity $\widetilde{\mathbf{u}}$ by solving equation (2.50) with approximate derivatives. The values from step 1 are used as boundary conditions here;
3. Calculate the scalar field ψ by solving the Poisson equation (2.46);
4. Obtain $\mathbf{u}^{n+1}$ using the update formula (2.44);

Figure 7 – Illustration of the free surface during the topological change algorithm that breaks a block of fluid presenting a thin filament.

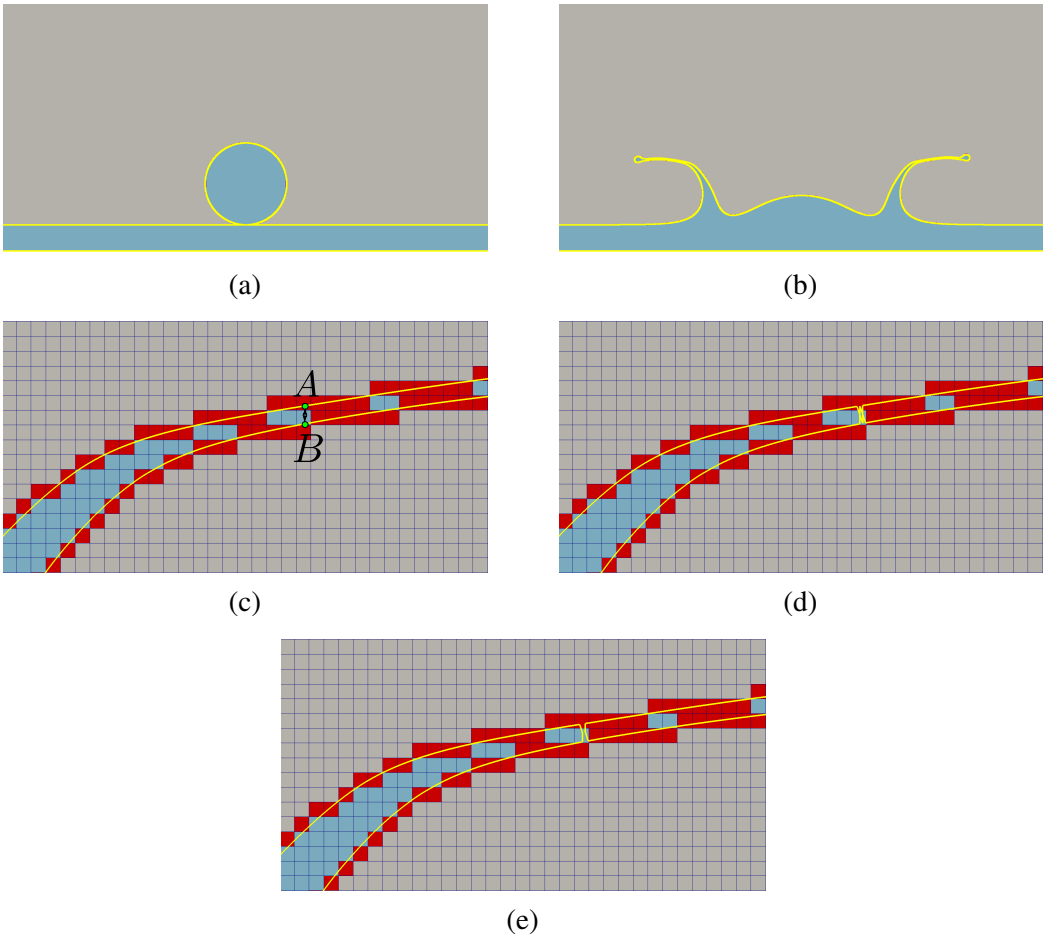

(a) (b) (c) (d) (e)

Source: Elaborated by the author.

5. Obtain p^{n+1} using the update formula (2.54);

6. Update tensor $\mathbf{T}$ using the chosen formulation (CSF or NSF) and its respective equations (2.60)-(2.62) or (2.66)-(2.68);

7. Advect the marker particles using the new velocity according to the equation

$$\dot{\mathbf{x}} = \mathbf{u}. \tag{2.73}$$

The steps described above must be executed for each time step, in such a way that the velocity and pressure are iteratively updated.

CHAPTER

3

NATURAL STRESS FORMULATION ON A CONTRACTION FLOW

3.1 Introduction

Advances in numerical methodologies have contributed to the investigation into the rheological response behaviour of complex materials in specific geometries. These include contraction type flows (BOGER, 1987) or new micro-devices such as cross-slot flows (POOLE; ALVES; OLIVEIRA, 2007). These flow geometries are used in general to measure the extensional properties and explore fluid rheology responses, where quite distinct behaviour from Newtonian fluids are obtained for viscoelastic fluids such as Boger fluids (AFONSO *et al.*, 2011).

In recent decades, since the publication of Walters and Webster (WALTERS; WEBSTER, 2003) evidencing the challenges involved in the contraction geometry and its admission as a classical benchmark problem back in 1988 (FIFTH. . . , 1988), it has been widely used for validation/verification of numerical codes. In particular, not only the accuracy (ABOUBACAR; MATALLAH; WEBSTER, 2002)–(LIU; SI, 2019) but also the stability of the numerical methodologies (AFONSO *et al.*, 2011)–(MEDVID'OVÁ; NOTSU; SHE, 2015) have been exhaustively verified. Besides in-house code validations, this benchmark problem has been also applied for verifying open-source solvers provided in the literature, as for example, in the implementation of toolboxes in OpenFOAM (FAVERO *et al.*, 2010; PIMENTA; ALVES, 2017; ARAÚJO *et al.*, 2018). One aspect of the many code verifications described in the literature for contraction flows is their predominant focus upon vortex behaviour and pressure drops. Attention is only given briefly to the asymptotic behaviour of the stress in the vicinity of the sharp re-entrant corner (ALVES; OLIVEIRA; PINHO, 2003; KIM *et al.*, 2005; EVANS; OISHI, 2017), despite the presence of sharp stress wall boundary layers which have not been investigated. Thus, in order to present further knowledge about the stress singularity and to allow for continuous improvement of the codes, in this chapter we have adopted Newtonian kinematics. This allows for a careful

comparison to be made between the asymptotics and numerical computations in a simplified, intermediate case. Imposing a Newtonian velocity field, we propose to use it as a simplified benchmark for testing viscoelastic numerical schemes focusing on the behaviour of the stress components around corners.

The studies concerning the benchmark flows will be done for two distinct mathematical methodologies: the Cartesian and the natural stress formulations. The former, is widely applied in the computational rheology, whilst the latter has been recently applied for unsteady viscoelastic simulations (EVANS; FRANÇA; OISHI, 2019). Using the intermediate case of a Newtonian velocity field allows a direct comparison to be made between the two formulations for numerical schemes, since the results can be benchmarked to the known asymptotics around singular points for contraction flows.

It is worth noting that the assumption of fixed Newtonian kinematics for Oldroyd-B fluids has previously been applied for asymptotic and computational studies of other benchmark problems, for instance, the flow of a viscoelastic fluid around a cylinder (RENARDY, 2000; WAPPEROM; RENARDY, 2005). It has also been used in early numerical work for the stick-slip problem (ROSENBERG; KEUNINGS, 1991; FORTIN; ZINE; AGASSANT, 1992), before the asymptotic classification of the problem. Further, for other viscoelastic models, such as Phan-Thien–Tanner (PTT) (THIEN; TANNER, 1977; PHAN-THIEN, 1978) and Giesekus (GIESEKUS, 1982), a Newtonian velocity field predominates at stress singularities for sharp corners (RENARDY, 1997; EVANS, 2010b; EVANS, 2010a). As such, using a Newtonian velocity field for such models is then wholly relevant and evaluating how the Oldroyd-B model behaves provides a useful study.

The work that will be described in this chapter is part of the following publication:

- Evans, J.D.; França, H.L.; Junior, I.P.; Oishi, C.M. Testing viscoelastic numerical schemes using the Oldroyd-B fluid in Newtonian kinematics. Applied Mathematics and Computation, v. 387, p. 125106, 2020.

3.2 Numerical setup

We begin our numerical simulations by investigating the solution of a 4 : 1 contraction flow using the natural stress formulation. These simulations are performed in the geometry shown in Figure 8a, with non-uniform cell distributions around the re-entrant corners as shown in Figure 8b. Two different meshes are used in our tests, their details are presented in Table 1.

For simulations in a contraction geometry, we will obtain the nondimensionalised equations (2.8)-(2.10) by choosing the following characteristic values: U is the average outflow velocity and L is the half-width of the outflow channel. We note that this is a confined problem with no gravity, such that $\mathbf{g} = \mathbf{0}$ in equation (2.8).

Figure 8 – Geometry of the 4 : 1 contraction flow (a) and non-uniform mesh details (b).

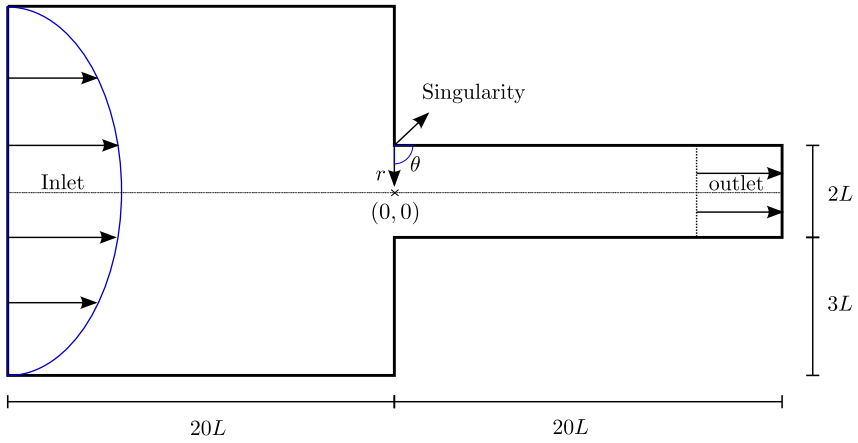

(a) Contraction geometry

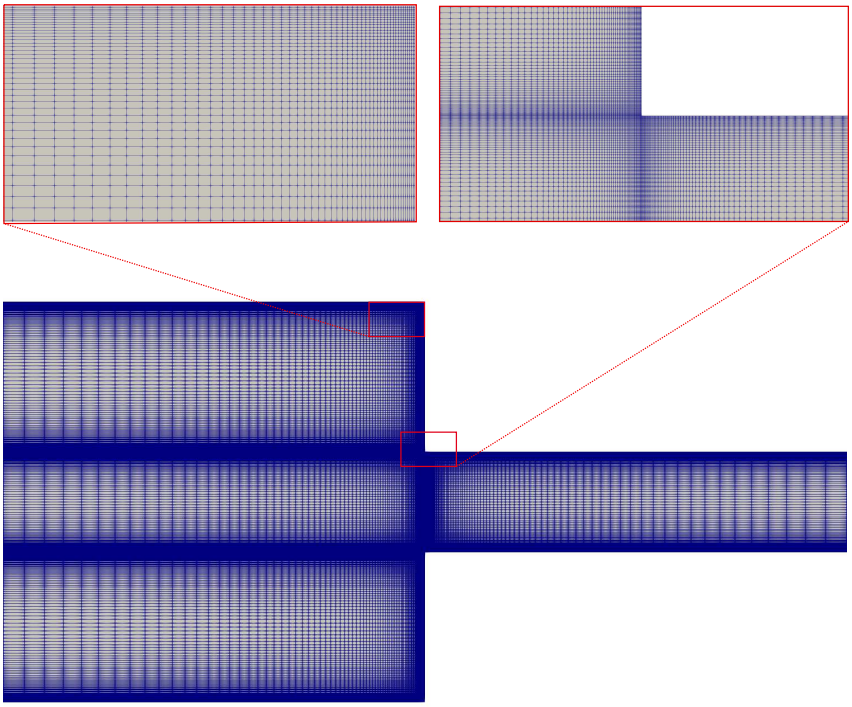

(b) Contraction mesh

Source: Elaborated by the author.

Table 1 – Details of the non-uniform meshes.

Mesh	Space-step	No. of cells	No. of cells in the x and y directions
M1 (non-uniform)	$\frac{\delta x_{min}}{L} = \frac{\delta y_{min}}{L} = 0.008$	32300	190×260
M2 (non-uniform)	$\frac{\delta x_{min}}{L} = \frac{\delta y_{min}}{L} = 0.004$	48400	220×340

Source: Research data.

3.3 Results in a Newtonian velocity field

The investigations in this section use only a Newtonian velocity field, that is, we assume that $\nabla \cdot \mathbf{T} = 0$ in equation (2.8). The nondimensional parameter values adopted are $\mathrm{Re} = 0.01$, $\mathrm{Wi} = 1$, $\beta = 1/9$ and $\varepsilon = 0$ (Oldroyd-B model).

3.3.1 Temporal convergence

We describe first the temporal convergence of CSF and NSF schemes. The mesh adopted is $M1$, as described in Table 1. The behaviour of the components of the Cartesian stress tensor and the NS variables around the singularity is studied through the local residuals as a function of time. In particular, the local residuals are captured at a control point Z located in the cell closest to the singularity. For instance, the residuals for the component T^{xx} of the extra stress tensor and the $\hat{\lambda}$ NS variable are respectively evaluated as

$$\begin{aligned} res(T^{xx})|_Z = & \left. \frac{(T^{xx})^{(n+1)} - (T^{xx})^{(n)}}{\delta t} \right|_Z + \left(u \frac{\partial T^x}{\partial x} + v \frac{\partial T^{xx}}{\partial y} \right) \Bigg|_Z^{(n+1)} \\ & - \left(2 \frac{\partial u}{\partial x} T^{xx} + 2 \frac{\partial u}{\partial y} T^{xy} \right) \Bigg|_Z^{(n+1)} + \left. \frac{T^{xx}}{\mathrm{Wi}} \right|_Z^{(n+1)} - \left. \frac{2}{\mathrm{Wi}} (1-\beta) \frac{\partial u}{\partial x} \right|_Z^{(n+1)}, \end{aligned} \tag{3.1}$$

and

$$\begin{aligned} res(\hat{\lambda})|_Z = & \left. \frac{\hat{\lambda}^{(n+1)} - \hat{\lambda}^{(n)}}{\delta t} \right|_Z + \left(\frac{2\hat{\mu}}{|\mathbf{v}|^2} \left(v \frac{\partial u}{\partial t} - u \frac{\partial v}{\partial t} \right) \right) \Bigg|_Z^{(n+1)} + \left(|\mathbf{v}|^2 (\mathbf{v} \cdot \nabla) \left(\frac{\hat{\lambda}}{|\mathbf{v}|^2} \right) \right) \Bigg|_Z^{(n+1)} \\ & + \left(2\hat{\mu} |\mathbf{v}|^2 \nabla \cdot \mathbf{w} \right) \Big|_Z^{(n+1)} + \left(\frac{1}{Wi} \left(\hat{\lambda} - 1 \right) \right) \Bigg|_Z^{(n+1)}, \end{aligned} \tag{3.2}$$

where the local residuals for the other components of the extra stress tensor and for the remaining NS variables can be constructed in a similar manner according to their constitutive equations. The local residual investigation is performed for the time-steps $\delta t = 10^{-4}, 5 \times 10^{-5}$ and 10^{-5}.

Figure 9 shows the time variation of the local residuals on a logarithm scale, verifying that both formulations are convergent with similar decay rates. For the $\hat{\mu}$ and $\hat{v}$ variables using $\delta t = 10^{-4}$ and $\delta t = 10^{-5}$, there are slight oscillations when the residuals become small.

3.3.2 Global behaviour

The second round of comparisons considers the global behaviour of the properties away from the re-entrant corner. In figure 10, we have plotted the results for the u-component of the velocity field, the pressure field and the first normal stress difference ($N_1 = T_{22}^P - T_{11}^P$) along the centreline of the contraction, for instance at $y = 0$. For the variables u and p in Figs. 10 a) and b), we have the exact same values for both formulations since we are using the same Newtonian velocity field. For the N_1 variable both formulations show excellent agreement.

Figure 9 – Time variation of the CSF (left) and NSF (right) local residuals near to the singularity.

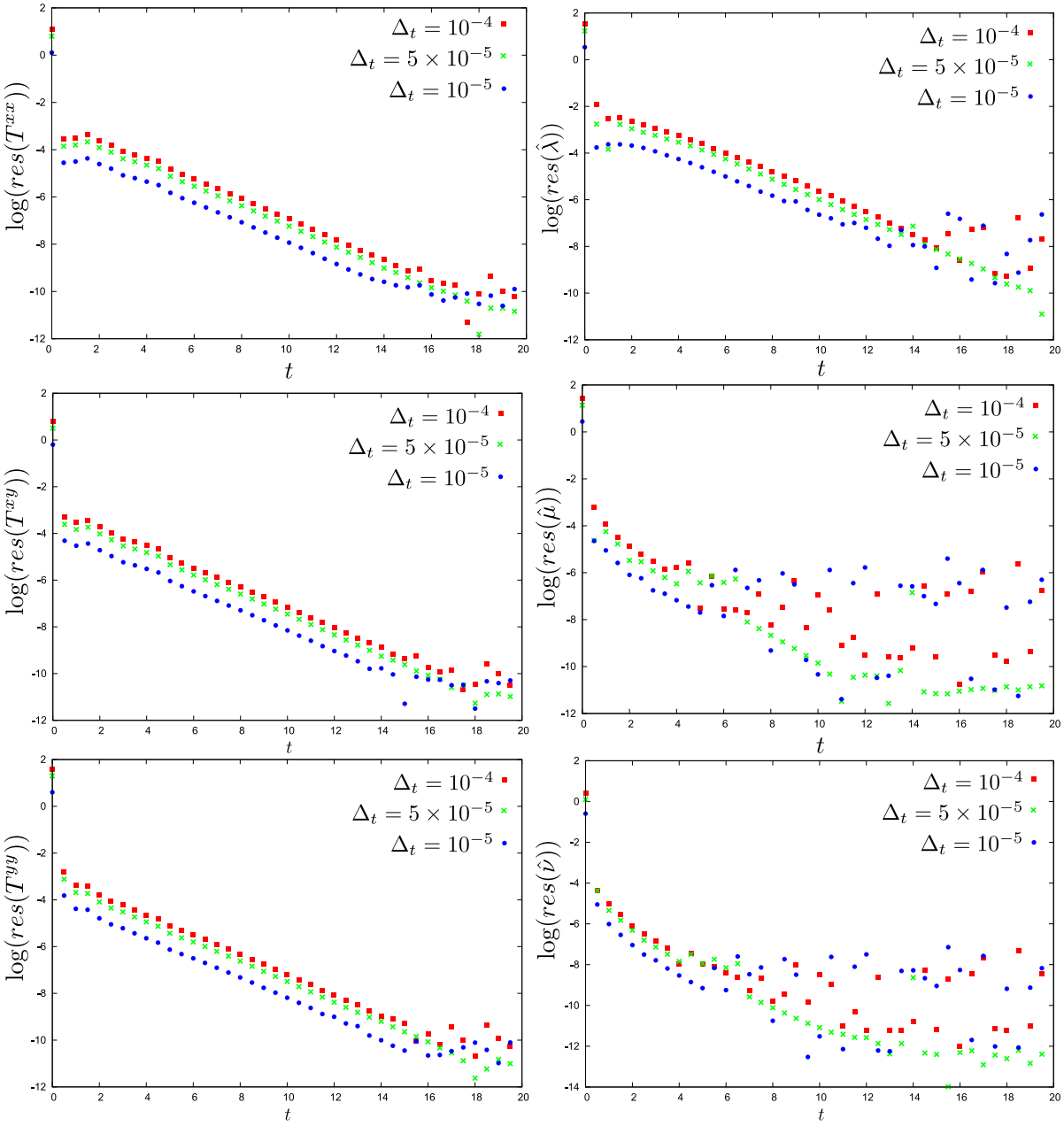

Source: Elaborated by the author.

Another study of interest is analysing the flow type parameter (ξ) defined by

$$\xi = \frac{|\frac{1}{2}(\nabla \mathbf{v} + (\nabla \mathbf{v})^T)| - |\frac{1}{2}(\nabla \mathbf{v} - (\nabla \mathbf{v})^T)|}{|\frac{1}{2}(\nabla \mathbf{v} + (\nabla \mathbf{v})^T)| + |\frac{1}{2}(\nabla \mathbf{v} - (\nabla \mathbf{v})^T)|}. \tag{3.3}$$

This may be used for identifying the type of local flow dominating in spatial locations, where $\xi = -1$ implies solid-like rotation, $\xi = 1$ characterizes pure extensional flow, and $\xi = 0$ represents pure shear flow. Results for the contour map of ξ are presented in figure 11 while figure 12 shows a zoom of the re-entrant corner. It is interesting to note that the Newtonian velocity field maintains the same main local types of flow seen in (AFONSO *et al.*, 2011) for the fully viscoelastic flow field, i.e. extensional flow around the salient corner and in the centreline of the

Figure 10 – Horizontal profiles ($y = 0$) of u, p and $T_{22}^P - T_{11}^P$ at the steady-state for CSF and NSF considering the Newtonian velocity field.

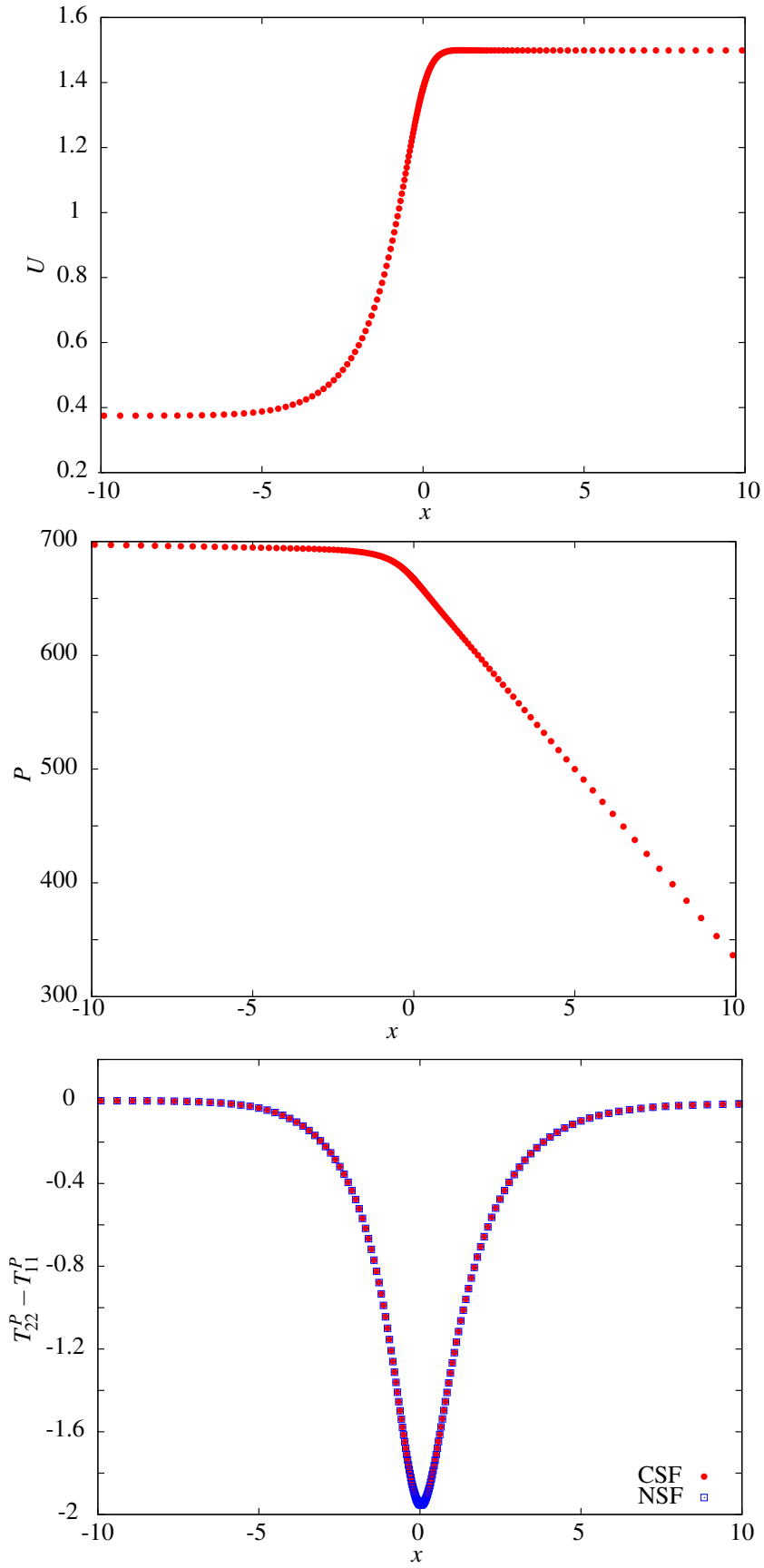

Source: Elaborated by the author.

Figure 11 – Visualization of the colour map for the flow classification parameter with the Newtonian velocity field.

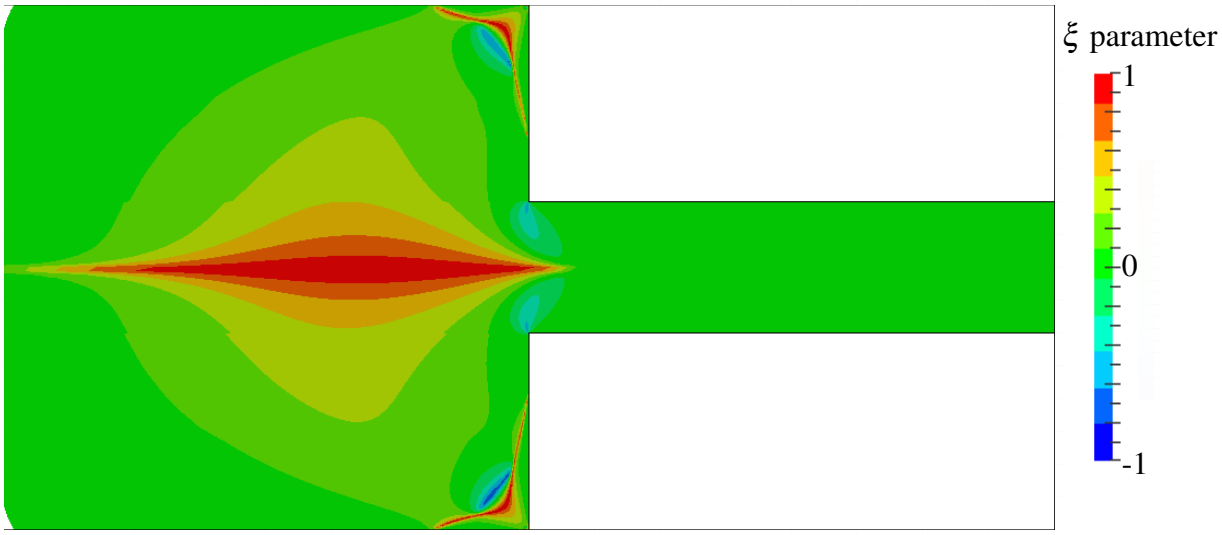

Source: Elaborated by the author.

Figure 12 – Zoom for the colour map visualization around the re-entrant corner with the Newtonian velocity field.

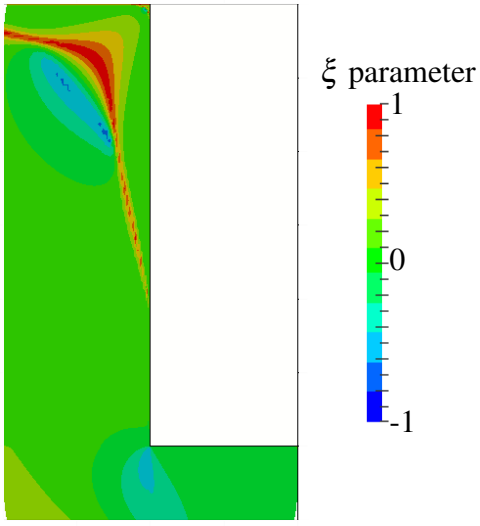

Source: Elaborated by the author.

first channel of the contraction, the solid-like rotation behaviour around the re-entrant corner and shear flow around the wall of the downstream channel and in the remainder of the upstream channel.

3.3.3 Spatial convergence near the singularity

We now compare the numerical and asymptotic results in the 4 : 1 contraction flow using the meshes presented in Table 1. As the main objective of this study was to add to existing literature a new benchmark test focusing on the re-entrant corner and the stress singularity behaviour, we have assumed the same flow condition employed in the asymptotic analysis described in (EVANS *et al.*, 2020), i.e., the numerical schemes were solved using $\nabla \cdot \mathbf{T} = 0$ in equation (2.8). The asymptotics results provided by (DEAN; MONTAGNON, 1949; MOFFATT, 1964) for the velocity field and hence the solvent stress are discussed in detail in (EVANS *et al.*, 2020) and give that in the vicinity of the re-entrant corner, the elastic stress tensor behaves as

$$\mathbf{T}^p = O(r^{-0.7420}), \qquad \lambda = O(r^{-1.8310}), \qquad \mu = O(r^{-0.2865}), \qquad \nu = O(r^{1.2580}). \quad (3.4)$$

In order to present a detailed comparison with the asymptotic results, the numerical solutions are plotted along radial lines for three different values of θ (see Figure 13), specifically $\theta = \pi/2$, π and $3\pi/4$. It is worth noting that the θ angle is measured from the downstream wall. Figure 14 shows that the NSF results are in excellent agreement with the asymptotic results given in (3.4) in contrast with those produced by CSF. According to the first column of Figure 14, we can see that the CSF converges slower to its asymptotics than the NSF evidencing the need for a very fine mesh for this formulation to capture the correct asymptotics. In particular, for $\theta = \pi$, the CSF struggles with the T^{yy} component. These results confirm the accuracy of the NSF in re-entrant corner flows, as demonstrated initially by Renardy (RENARDY, 1994).

Figure 13 – Illustration of the selected angles for studying the asymptotic behaviour near the singularity.

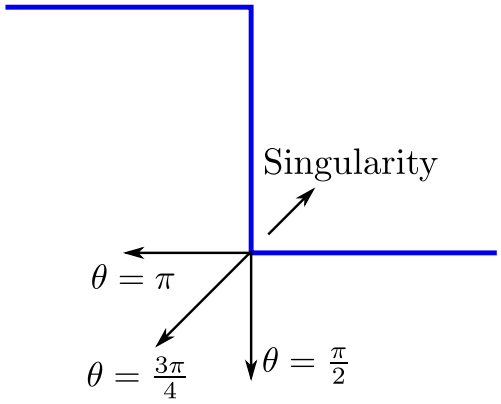

Source: Elaborated by the author.

3.3.4 Boundary layer structures

We may further explore the stress singularity by examining numerically the boundary layer structures at the walls local to the re-entrant corner. For this, we compare the absolute

Figure 14 – Asymptotic variation near the singularity. Variation of T^{xx}, T^{xy}, T^{yy} using CSF (left), and variaton of λ, μ and ν using NSF (right).

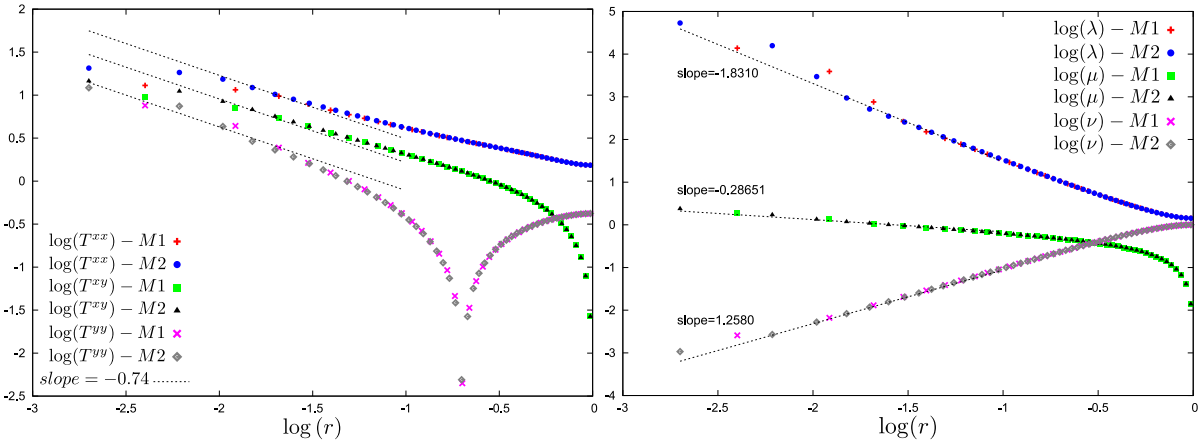

(a) $\theta = \frac{\pi}{2}$

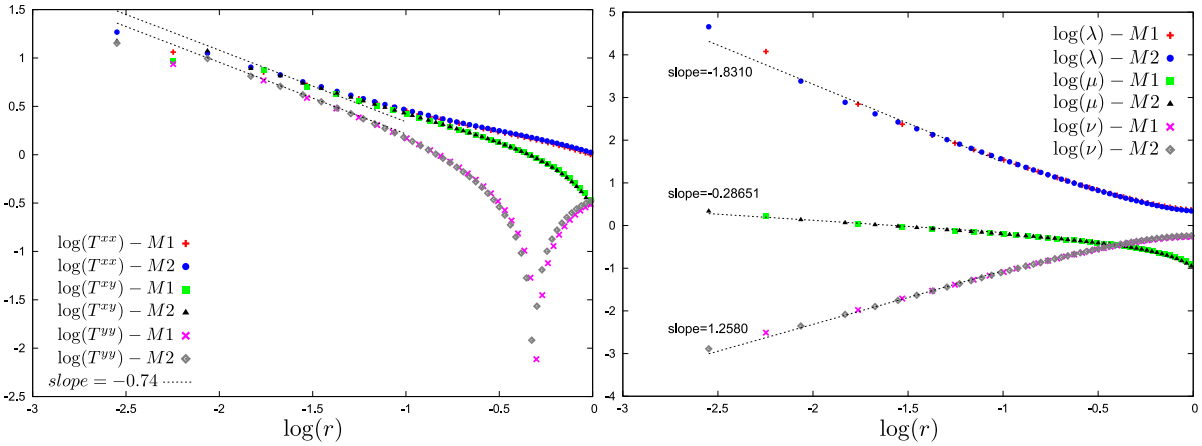

(b) $\theta = \frac{3\pi}{4}$

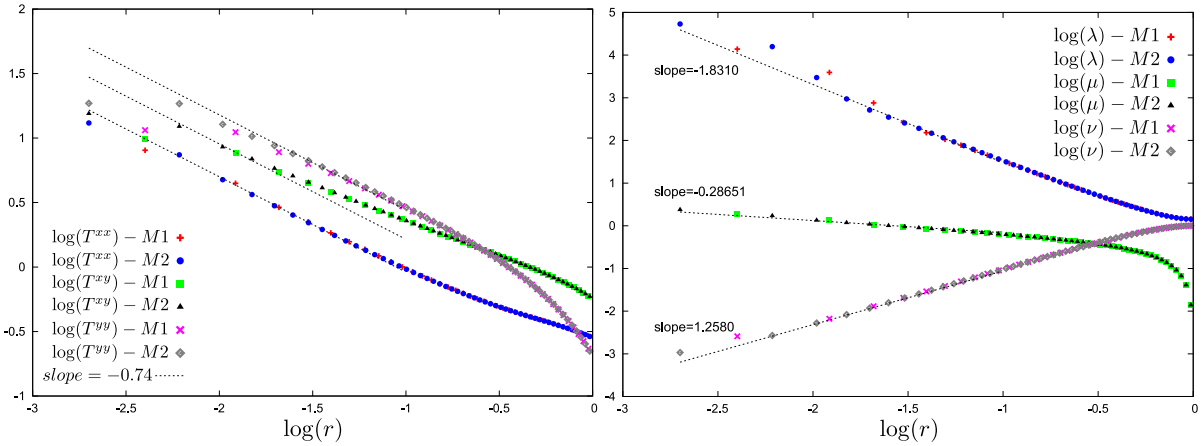

(c) $\theta = \pi$

Source: Elaborated by the author.

magnitude of the main groups of terms in the constitutive equations (2.10), i.e., we investigate

$$\max\left(\frac{|\mathbf{T}^{ij}|}{Wi}, |\overset{\triangledown}{\mathbf{T}}^{ij}|, \frac{2(1-\beta)}{Wi}|\mathbf{D}^{ij}|\right), \tag{3.5}$$

for each of the three components $ij = xx$, xy and yy separately. This study is also conducted for NSF since the elastic extra-stress tensor $\mathbf{T}$ can be recovered from NS variables using the relationships (2.25)-(2.27). Results are presented in Figure 15, in which we have considered a specific region near the singularity, with the maps being labeled without the presence of the modulus sign for convenience. In the first column of this figure, results for CSF are described for each component while in the second column we have results using the NS variables. Notice that for component xx, as described in Figures 15a and 15b by blue representations, both formulations show the dominance of the upper convective polymer stress derivative in the vicinity of the geometrical singularity. Comparing Figures 15c and 15e with Figures 15d and 15f, we can see that the NSF more adequately captures the boundary layer structures, since very close to the singularity, the term $\overset{\triangledown}{\mathbf{T}}$ more strongly dominates for the components xy and yy. For both formulations, the stress boundary layers are evident at both upstream and downstream walls, where either rate of strain or the relaxation terms dominate, as must be required for viscometric behaviour. In summary the results are in agreement with the expected asymptotic results described in (EVANS *et al.*, 2020).

3.4 Results in the true viscoelastic velocity case

3.4.1 Temporal convergence

We now study simulations considering the true viscoelastic velocity field, that is, the term $\nabla \cdot \mathbf{T}$ is no longer dropped in equation (2.8). Again, the mesh adopted for this study is $M1$. As well explained in (EVANS; FRANÇA; OISHI, 2019), the pure NSF imposes a severe space step restriction in simulations combining the true viscoelastic velocity field with a small viscosity ratio $\beta = 1/9$. Therefore, for the viscoelastic velocity field simulations, we have adopted the hybrid version proposed in (EVANS; FRANÇA; OISHI, 2019), which uses the traditional CSF formulation in a very narrow band of cells close to the singularity. Figure 16 shows that both formulations are convergent and that the oscillations present in some time steps for the Newtonian velocity case are corrected. Of particular note are the faster convergence rate of the NSF stresses.

3.4.2 Global behaviour

Figures 17(a) and (c) confirm, as in the Newtonian velocity case, that both formulations produce practically identical results for u and $T^P_{22} - T^P_{11}$. However, as presented in figure 17 (b), it is evident that the profile for the pressure field is highly dependent on the formulation in the viscoelastic case. As expected, the solutions for both CSF and NSF in the viscoelastic velocity field increase the values of the pressure drop as compared with those using the Newtonian velocity field.

According to figure 18, we note that both CSF and NSF formulations in the viscoelastic

Figure 15 – Dominance of the groups of terms for components *xx*, *xy* and *yy* within the Cartesian constitutive equation in a Newtonian velocity field: first column for CSF and second column for NSF.

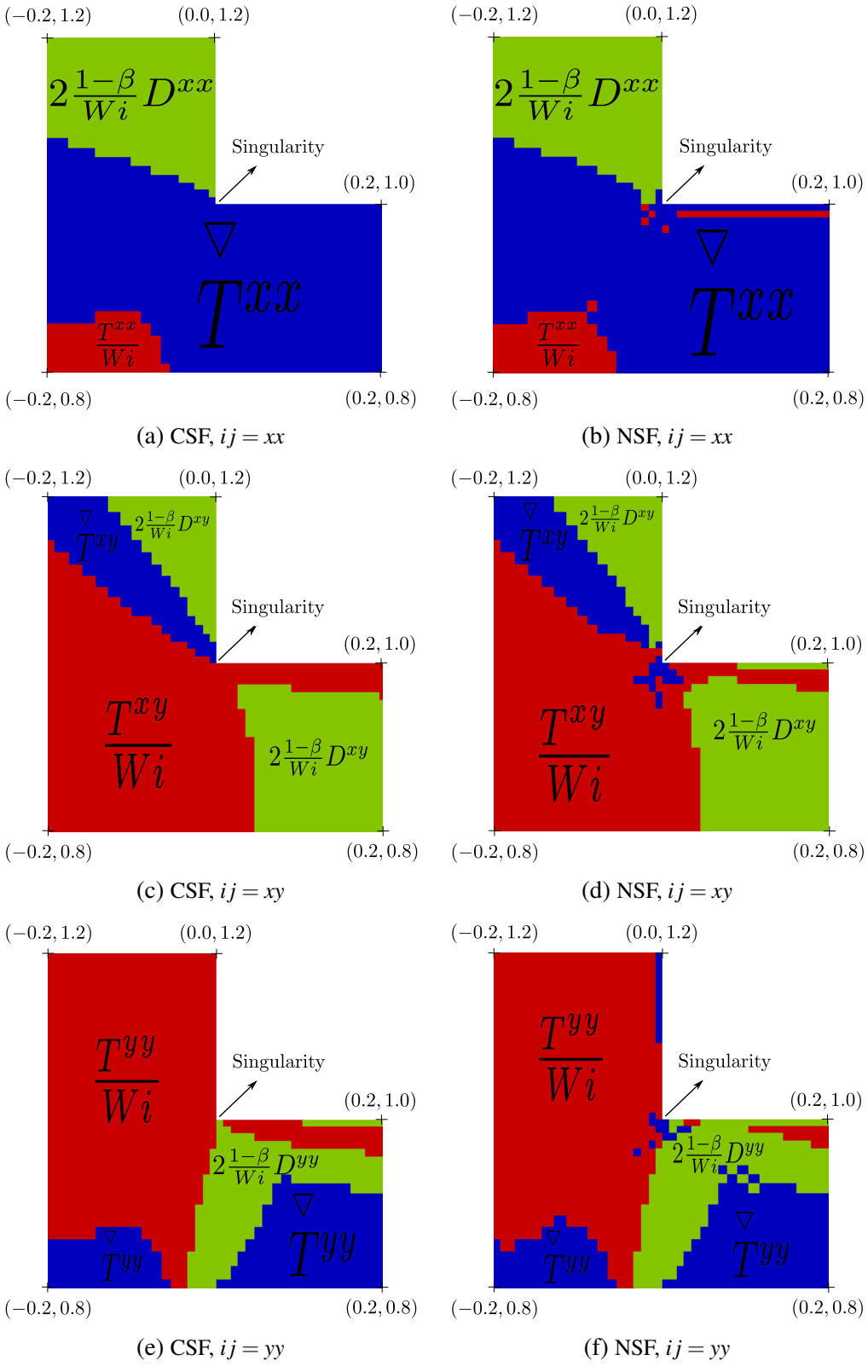

velocity field produce similar results to those plotted in figure 11 for the Newtonian velocity. However, a noteworthy difference can be seen in the narrower channel, where extension now

Figure 16 – Time variation of the CSF and NSF local residuals near the singularity using the viscoelastic velocity field.

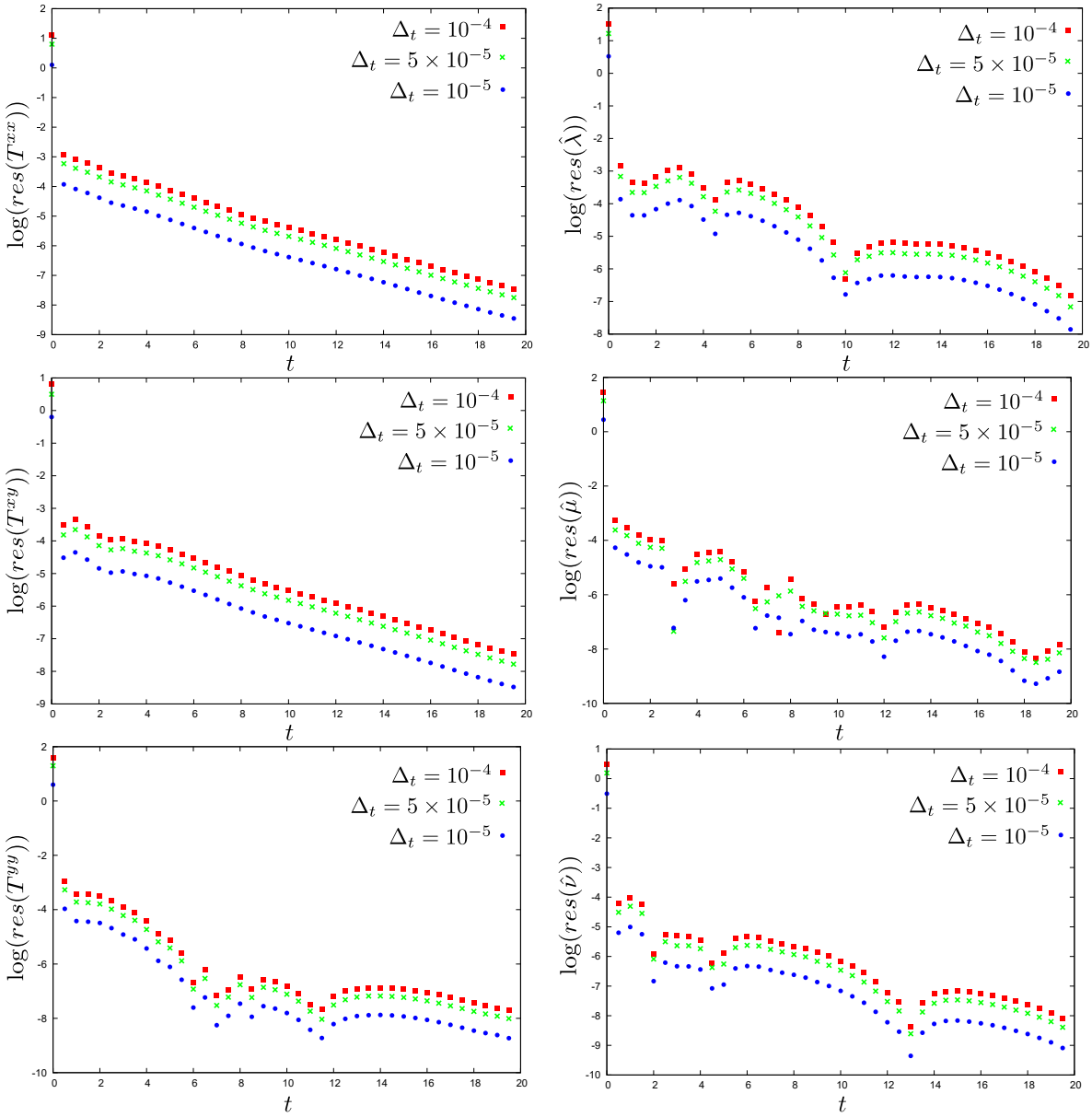

Source: Elaborated by the author.

remains high along the centre of the channel. Moreover, as we can see in the zoomed views in figures 12 and 18, there are noticeable differences between the application of the two different velocity fields around the salient and re-entrant corners. In particular, the NSF hybrid version with viscoelastic velocity increases the solid-like rotation flow type around the singularity in the re-entrant corner.

3.4.3 Boundary layer structures

A comparison between numerical (CSF and NSF) and asymptotic results near the singularity in the viscoelastic velocity field was presented in (EVANS; FRANÇA; OISHI, 2019). We

Figure 17 – Horizontal profiles ($y = 0$) of u, p and $T_{22}^P - T_{11}^P$ at the steady-state for CSF and NSF considering the true viscoelastic velocity fields. For the viscoelastic velocity field, it was considered the hybrid version of the NSF (EVANS; FRANÇA; OISHI, 2019), denoted as Hyb. NSF.

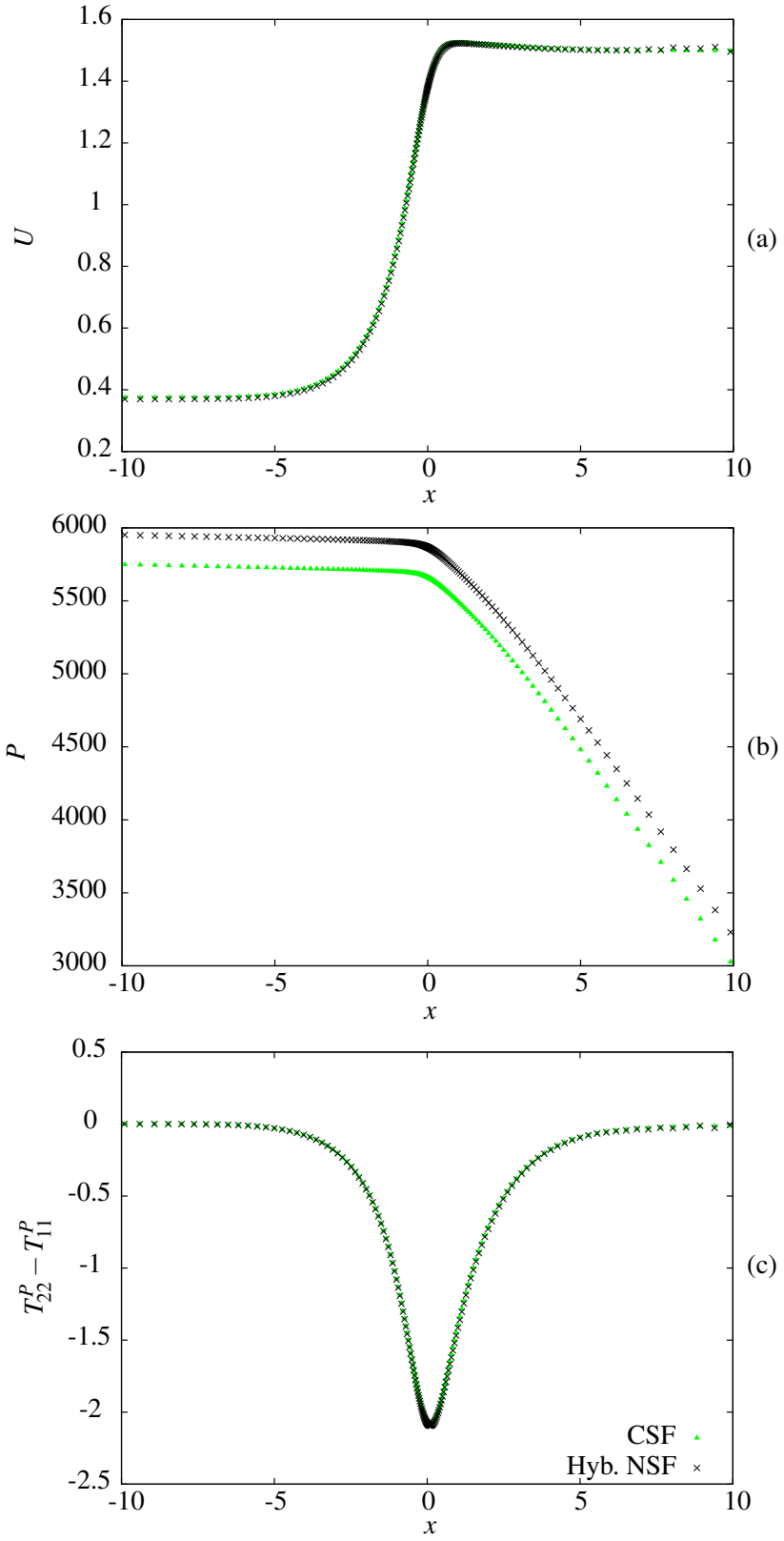

Source: Elaborated by the author.

Figure 18 – Visualization of the colour map for the flow classification parameter in a viscoelastic velocity field. a) CSF and b) Hybrid NSF.

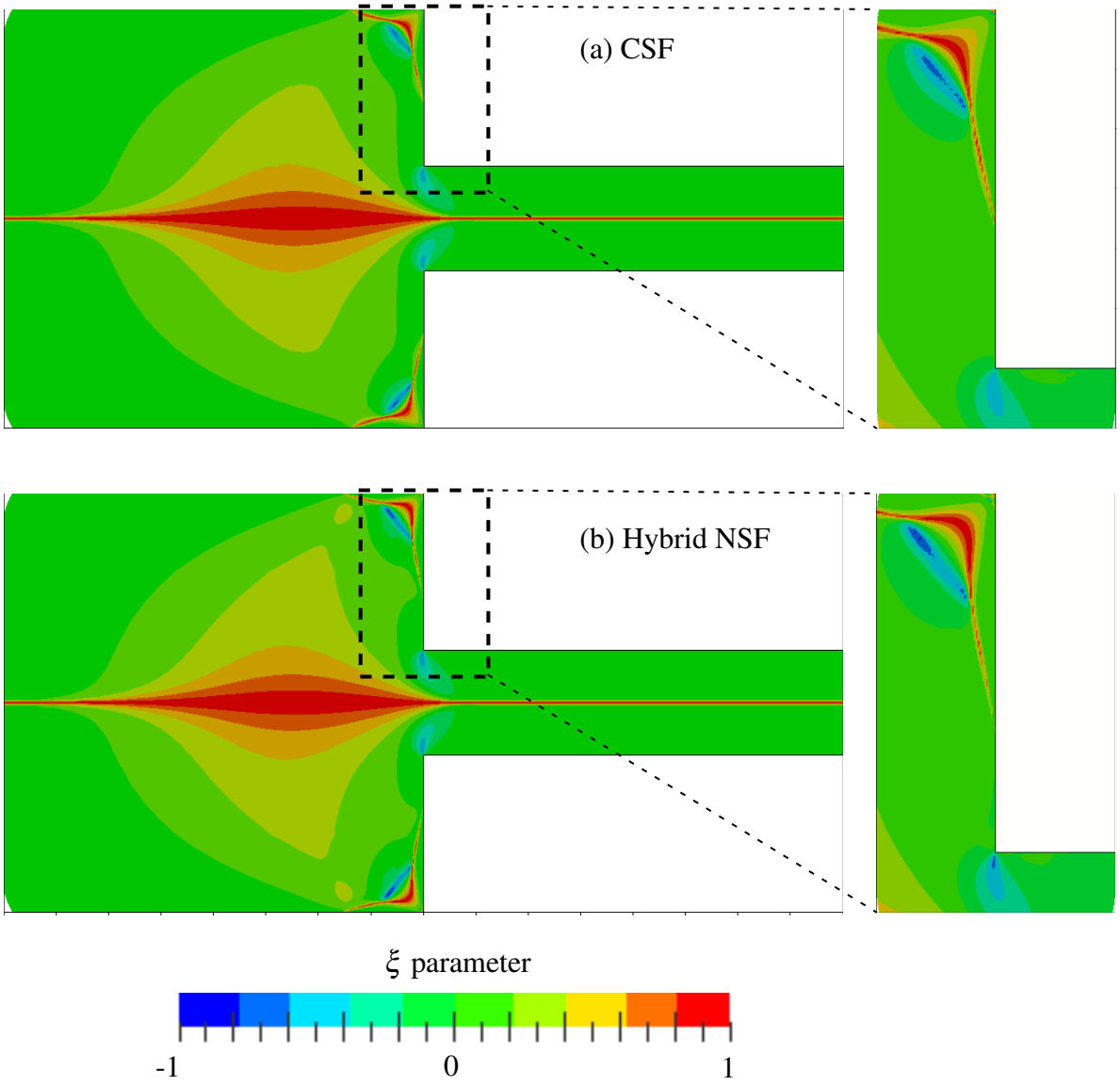

Source: Elaborated by the author.

augment those results here by presenting the maps for the boundary layer structures.

Figure 19 shows better agreement with the theoretical asymptotic structure for CSF than in the Newtonian velocity case. It is still noteworthy that NSF produces a larger region of dominance for the upper convected stress derivative than CSF (which is still relatively absent for the *yy* component of CSF, whilst it is correctly caught for this components by NSF). In both formulations, evidence of the stress boundary layers at the walls are again indicated through the dominance of the rate-of-strain or relaxation terms (both being required for correct viscometric behaviour).

Figure 19 – Dominance of the groups of terms for components 11, 12 and 22 within the Cartesian constitutive equation using the viscoelastic velocity field: first column for CSF and second column for NSF.

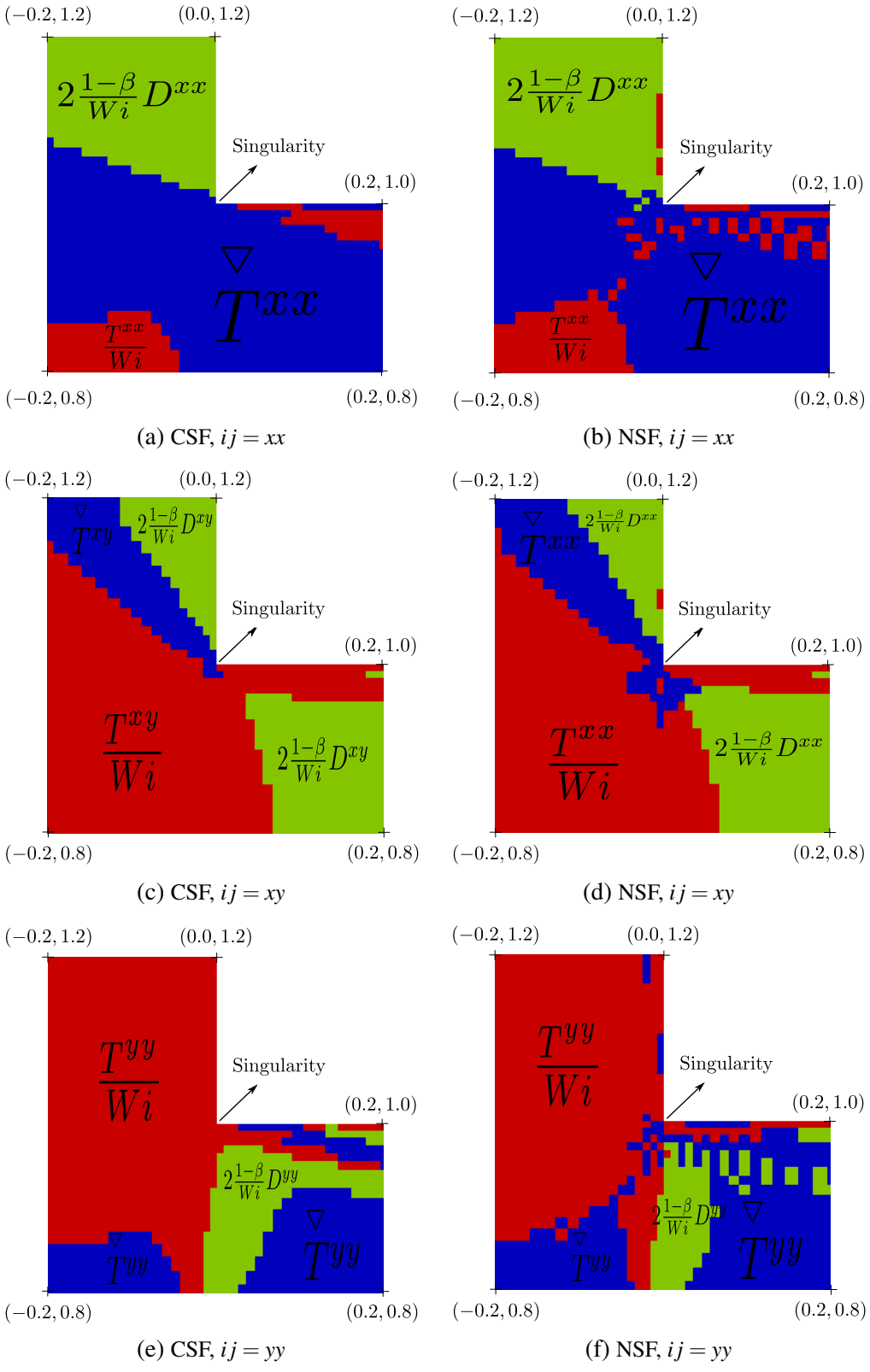

(a) CSF, $ij = xx$

(b) NSF, $ij = xx$

(c) CSF, $ij = xy$

(d) NSF, $ij = xy$

(e) CSF, $ij = yy$

(f) NSF, $ij = yy$

3.5 Conclusions

We have considered here two different viscoelastic formulations of the Oldroyd-B equations, and assessed these in a contraction flow problem under a Newtonian velocity field. The motivation for the fixed kinematics being that it is an intermediate case that decouples the constitutive and momentum equations.

In the context of the contraction flow, the numerical comparisons have been performed for Weissenberg unity, our intention being to compare the temporal and spatial convergence of the two formulations, particularly near the re-entrant corner stress singularity. The method of matched asymptotic expansions has been used to determine the structure and form of the singularity, the details presented here completing the initial analysis by Renardy (RENARDY, 1993). The numerical results indicate that the NSF is able to capture more accurately, not only the stress singularity, but also the asymptotic structure local to the corner, including the stretching region (where the upper convected derivative of stress dominates) and the boundary layers at the walls.

We have noted that the stress behaviour of both formulations for Newtonian velocities share many similar flow characteristics to the viscoelastic velocity case. The re-entrant corner stress singularity is markedly different however, as it is stronger in the Newtonian velocity field. However, the global stress similarities between the two flow fields are expected to reduce as the Weissenberg number increases. In particular, the viscoelastic velocity field induces the appearance of a lip vortex at slightly higher Weissenberg numbers (ALVES; OLIVEIRA; PINHO, 2003), which is never present for Newtonian velocities.

CHAPTER

4

SHEAR-THINNING AND VISCOELASTIC BINARY DROPLET COLLISION

4.1 Introduction

Binary collision of droplets is an important and challenging problem in Fluid Mechanics. Examples of applications where drop collision is a key aspect of the phenomenon are the cloud and raindrop formation, droplet manipulation in microfluidics, and functional interfaces. In addition, the processes where the spray motion is present, such as insecticide spraying, spray painting, spray combustion, and others, the dynamics of droplet collision play a role that determines the process output. In some of the applications mentioned above, the main fluid in the process can exhibit non-Newtonian features.

Experimental investigations are responsible for important developments in the understanding of the variety of outcomes associated with this problem (ASHGRIZ; POO, 1990; JIANG; UMEMURA; LAW, 1992; QIAN; LAW, 1997). This approach does not need to deal with the difficulties that numerical schemes must overcome in order to handle complex free-surface problems. These works established important grounds for subsequent experimental and numerical analyses (NOBARI; JAN; TRYGGVASON, 1996; NOBARI; TRYGGVASON, 1996; QIAN; LAW, 1997; GOTAAS *et al.*, 2019; PAN; LAW; ZHOU, 2008; NIKOLOPOULOS; THEODORAKAKOS; BERGELES, 2009; LI; FRITSCHING, 2011; PLANCHETTE *et al.*, 2017; AL-DIRAWI; BAYLY, 2019; AL-DIRAWI *et al.*, 2021).

The role of the surface tension between the liquid and the surrounding gas in the case of these systems is a clear central point of the physics of the phenomenon. Besides that, even the first studies recognized the importance of evaluating the common case of non-frontal drop collisions. In this regard, two dimensionless groups were selected to evaluate critical aspects of

problem. The Weber number, We, given by

$$We = \frac{\rho U^2 L}{\gamma}, \tag{4.1}$$

defined as the ratio of inertial and surface tension effects. The impact parameter, B, is given by

$$B = \frac{b}{D}, \tag{4.2}$$

where D is the diameter of the droplets and b is the center-to-center relative distance. The impact parameter is a dimensionless normalized quantity that captures how non-frontal the collision is, i.e. $B = 0$ represents head-on collision and $B = 1$ indicates grazing collision. Figure 21 provides further information with respect to this quantity.

The dimensionless parameters, We and B, create a two-dimensional space for a collision output map, where the different scenarios after collision can be located. Usually, these scenarios are roughly classified into four main categories: *Bouncing*, where the drops rebound from each other; *Coalescence*, where two drops merge and stay at this configuration; *Separation*, where after a coalescence, the drops separate; and *Splashing*, where a breakage after collision results in multiple smaller droplets. Important theoretical analyses, resulted in models for boundary lines that separate the categories cited above in the $\{We, B\}$ space. In this regard, the reader is referred to the important review made by Sommerfield and Pasternak (SOMMERFIELD; PASTERNAK, 2019).

It is worth noticing that neither the Weber number, nor the impact number take into account the droplets viscosity. In order to capture its influence the Ohnesorge number is generally employed and this effect is also evaluated in the literature (GOTAAS *et al.*, 2019; FINOTELLO *et al.*, 2017; AL-DIRAWI *et al.*, 2021). Other evaluated output quantity is the evolution of the droplet diameters, with special emphasis to the maximum diameter achieved (PLANCHETTE *et al.*, 2017).

From the numerical perspective, the problem of binary droplet collision is extremely complex, mainly due to the topological changes involved. Methods that represent the interface purely implicitly, e.g. Volume-of-Fluid (VoF), automatically join the two droplets when they get close to each other, resulting in coalescence (FINOTELLO *et al.*, 2017). This implicit approach is used in the works of Li et al. (LI; FRITSCHING, 2011) and Nikolopoulos et al. (NIKOLOPOULOS; THEODORAKAKOS; BERGELES, 2009) among others. On the other hand, methods that describe the interface explicitly, e.g. Front-Tracking, in general do not join the two droplets in an automated manner, which causes them to favour the bouncing output (see (NOBARI; TRYGGVASON, 1996; NOBARI; JAN; TRYGGVASON, 1996)).

Most of the studies analyze the droplet collision in the low/intermediate-Weber-number range, where the *Splashing* outcome is avoided. Variations with respect to the basic problem include: i) droplets with different sizes (TANG *et al.*, 2016); ii) droplets with different fluids

(FOCKE *et al.*, 2013); iii) ternary drop collision (HINTERBICHLER; PLANCHETTE; BRENN, 2015); iv) different rheological properties of the droplet fluid.

The investigations of binary droplets collision with non-Newtonian fluids are mainly restricted to numerical approaches with Carreau-type viscosity functions with special emphasis on the shear–thinning branch (FOCKE; BOTHE, 2011; SUN *et al.*, 2015; HIRSCHLER *et al.*, 2017; XU; TANG; YU, 2020; QIAN; CONG; ZHU, 2020). An emblematic exception is the experimental work of Finotello et al. (FINOTELLO *et al.*, 2018). Focke and Bothe (FOCKE; BOTHE, 2011) employed a modified power-law viscous function and the VoF to handle the surface problem. They evaluated the drop diameter evolution in head-on collisions, comparing with the corresponding Newtonian outcome. Interestingly, they report that a constant viscosity that recovers the Newtonian dynamics can be found *a posteriori*. Sun et al. (SUN *et al.*, 2015) found significant differences between shear–thinning and Newtonian results for head–on collision, with the shear–thinning fluid deforming more substantially. A Smoothed Particle Hydrodynamics (SPH) approach was employed by Hirschler et al. (HIRSCHLER *et al.*, 2017) to capture the interface dynamics. While the shear–thinning results did not differ that much from the Newtonian ones, they found higher discrepancy with respect to the Newtonian case for the shear-thickening fluids, which exhibit lower deformations. Xu et al. (XU; TANG; YU, 2020) also employed SPH method to handle the interface problem, which was analyzed for head-on cases solely. They considered the surrounding gas in droplet collision, modelling this interaction with a van der Waals force. The VoF technique was employed with a Level-Set (LS) function by Qian et al. (QIAN; CONG; ZHU, 2020) to solve the binary collision of power-law fluids where surrounding gas is also considered. The authors used an effective Ohnesorge number in order to compare Newtonian and shear–thinning effects analyzing the energy evolution in time broken in kinetic, interface, and viscous dissipation contributions. Their analyses indicate that it is harder to separate polymeric liquids after coalescence than Newtonian ones.

The experimental investigation conducted by Finotello et al. (FINOTELLO *et al.*, 2018) explores the droplet collision of a Xanthan solution of 500ppm in water. The authors fitted the shear–thinning viscosity function with a Carreau model and provided a map of outputs in the $\{We, B\}$ space, providing the Newtonian case for comparison. An important remark highlighted in (FINOTELLO *et al.*, 2018) is the role of the extensional viscosity in the problem. Droplet collisions are far from leading to viscometric motions, specially for low values of B. The Trouton ratio for a Xanthan solution of 500ppm in water is reported to be $Tr \approx 100$ (see (FULLER *et al.*, 1987)). In this regard, a Generalized Newtonian Fluid with a shear–thinning viscosity (employed in most of the numerical drop collision works of non–Newtonian fluids) would not be able to capture the extensional response present in this problem, motivating the investigation of viscoelastic models more complex than the Oldroyd-B.

In the present work, we examine the binary droplet collision in non-Newtonian fluids using the Mark and Cell (MAC) approach combined with a Front-Tracking technique in order to

capture the interface dynamic of the free surface problem. We analyze a viscous shear–thinning Carreau-Yasuda equation and the viscoelastic constitutive models of Oldroyd–B and Phan–Thien–Tanner (PTT). Since the droplet collision motion has an extensional component, the PTT model can be more appropriate to capture the mechanical response of the droplets, since it combines shear–thinning and extensional–thickening effects.

The work that will be described in this chapter is published in the following article:

- França, H.L.; Oishi, C.M.; Thompson, R.L. Numerical investigation of shear-thinning and viscoelastic binary droplet collision. Journal of Non-Newtonian Fluid Mechanics, v. 302, p. 104750, 2022.

4.2 Governing equations and nondimensionalization

The governing equations for the isothermal incompressible flow, are the continuity and momentum equations (2.1) and (2.2) given in chapter 2. In this section we will consider two cases for the fluid rheology: shear-thinning materials and viscoelastic materials.

4.2.1 Shear-thinning materials

In the shear–thinning cases, the extra-stress tensor assumes the form of a generalized Newtonian liquid as

$$\boldsymbol{\tau} = 2\eta(\dot{\gamma})\mathbf{D}, \tag{4.3}$$

where $\mathbf{D} = \frac{1}{2}\left(\nabla\mathbf{u} + (\nabla\mathbf{u})^T\right)$ is the rate-of-strain tensor and $\eta(\dot{\gamma})$ is a viscosity function of the deformation rate, $\dot{\gamma} \equiv \sqrt{0.5tr\left[(2\mathbf{D})^2\right]}$. In this paper, we use two different models for the viscosity function. The first is the Carreau-Yasuda model given by

$$\eta(\dot{\gamma}) = \eta_\infty + \eta_{thinning}(\dot{\gamma}) = \eta_\infty + (\eta_0 - \eta_\infty)\left[1 + (\lambda_{cu}\dot{\gamma})^a\right]^{\frac{n-1}{a}}, \tag{4.4}$$

where η_0 and η_∞ are the Newtonian viscosities plateaus in the limits of $\dot{\gamma} \to 0$ and $\dot{\gamma} \to \infty$, respectively, λ_{cu} is the Carreau characteristic time, n is a power-law index, and a is a fitting parameter. The second model is the Cross model, given by

$$\eta(\dot{\gamma}) = \eta_\infty + \eta_{thinning}(\dot{\gamma}) = \eta_\infty + \frac{\eta_0 - \eta_\infty}{1 + K\dot{\gamma}^m}, \tag{4.5}$$

where K and m are two constants representing the shear-thinning nature of the Cross-model fluid.

A non-dimensionalization can be performed by scaling the variables as follows

$$\mathbf{x} = L\bar{\mathbf{x}}, \quad t = \frac{L}{U}\bar{t}, \quad \mathbf{u} = U\bar{\mathbf{u}}, \quad p = \rho U^2\bar{p}, \quad \eta_{thinning} = \eta_\infty\bar{\eta}_{thinning}, \quad \mathbf{g} = g_0\bar{\mathbf{g}}, \tag{4.6}$$

using the relative impact velocity U and initial droplet diameter L as characteristic velocity and length, respectively, and g_0 as a characteristic source term.

Substituting (4.3) and (4.6) in (2.1) and removing, for convenience, the upper bars, the non-dimensional governing equations for a shear-thinning fluid are given by

$$\frac{\partial \mathbf{u}}{\partial t} + \nabla \cdot (\mathbf{uu}) = -\nabla p + \frac{1}{Re}\nabla^2 \mathbf{u} + \frac{1}{Re}\nabla \cdot \left(2\bar{\eta}_{thinning}(\dot{\gamma})\bar{D}\right) + \frac{1}{Fr^2}\mathbf{g}, \tag{4.7}$$

$$\nabla \cdot \mathbf{u} = 0, \tag{4.8}$$

with non-dimensional groups: Reynolds number (Re) and Froude number (Fr) defined as

$$Re = \frac{\rho U L}{\eta_\infty}, \quad Fr = \frac{U}{\sqrt{g_0 L}}. \tag{4.9}$$

4.2.2 Viscoelastic materials

In the case of viscoelastic fluids, the extra-stress tensor $\boldsymbol{\tau}$ is composed of a solvent $\boldsymbol{\tau}^s$ and a polymeric $\boldsymbol{\tau}^p$ contributions as described in equation (2.3). The constitutive equation for $\boldsymbol{\tau}^p$ is given by the PTT model as in equation (2.5). For all Newtonian simulations in this section, the viscosity ratio is assumed $\beta = 1$, while for the viscoelastic models we have fixed $\beta = 1/9$.

Here we observe that the simulations with the PTT model are governed by the following dimensionless numbers: Re, Wi, ε, β, Fr, and We. Preliminary studies revealed that the Froude number, defined as $Fr = U/\sqrt{g_0 L}$ with g_0 a characteristic source term, and the viscosity ratio had little impact on the outputs. In this regard, we focused our analysis on the role played by the other dimensionless numbers. It is worth noticing that the Ohnesorge number is sometimes regarded as an independent dimensionless parameter (replacing the Reynolds number) and it can be computed as $Oh = \sqrt{We}/Re$. Because of this tradition, in some situations we disclosed the Oh value when it was considered convenient.

4.2.3 Discretization and numerical coalescence

The entire spatial domain is discretized using a uniform mesh. As described in section 2.4.3, each cell receives a classification indicating if it is located fully inside, fully outside or on the interface of a droplet. Figure 20 shows a grid example with all its cells classified according to the fluid location. The Front-Tracking representation of the interface can also be seen through the connected marker particles.

We note that, in figure 2.4.3a the droplets are far from each other, which gives the underlying mesh a natural band of EMPTY cells between the droplets. When the droplets approach each other and touch, this band disappears and we obtain a fully connected region of FULL cells that is shared between the two droplets. However, the Front-Tracking interface still contains two separate droplets, which contradicts the information of the underlying mesh that indicates a single body of fluid. When this is detected in our algorithm, we have the choice of artificially modifying the Front-Tracking interface to promote a coalescence of the droplets, which is done by connecting the two lists of marker particles. The result of this is illustrated in

Figure 20 – Examples of cell classification in a free surface simulation with coalescence.

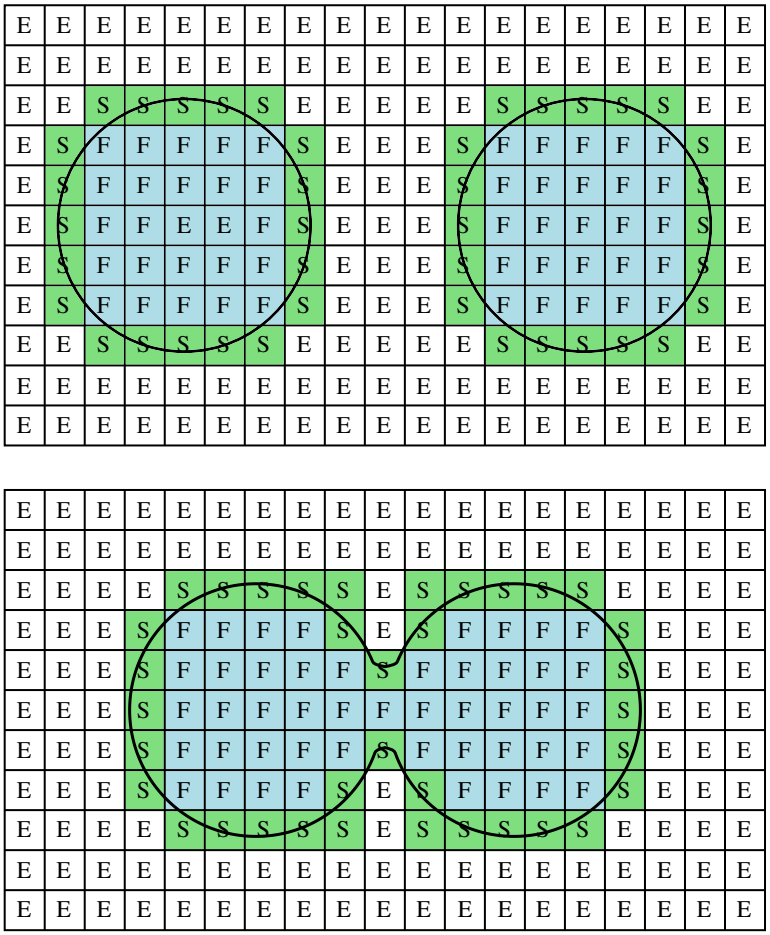

Source: Elaborated by the author.

figure 2.4.3b. If the artificial coalescence of the Front-Tracking interface is not performed, the droplets will always eventually bounce away from each other.

4.2.4 Computational geometry

Figure 21 presents a schematic of the problem considered. Both droplets with the same diameter are initialized with given velocities $\mathbf{u}_1$ and $\mathbf{u}_2$, respectively, and the initial geometry can be defined by a single impact parameter B (see figure 21). Recall that $B = 0$ represents head-on impact, while $B = 1$ indicates a grazing collision. The characteristic length and velocity quantities, employed in the construction of the dimensionless formulation are the diameter (D) and relative velocity ($|\mathbf{u}_r|$), respectively.

In experiments such as described in (AL-DIRAWI; BAYLY, 2019; FINOTELLO *et al.*, 2018), the droplets often are launched from a certain distance until they impact. Computationally, however, it is more convenient to initialize them already next to each other. This initial setup is created with the following steps:

Figure 21 – Schematic of the geometry used in the binary droplet collision simulations.

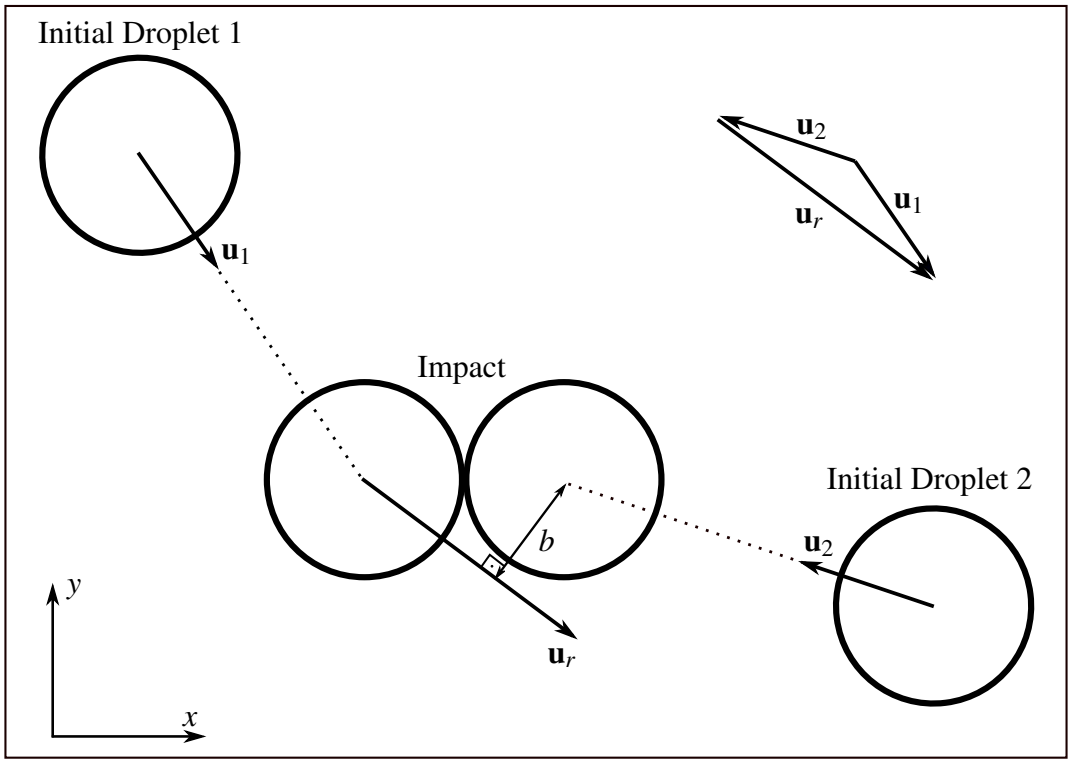

Source: Elaborated by the author.

1. Create two droplets next to each other horizontally, such as in Figure 22. Since D is the characteristic length, computationally the droplets have diameter equal to unity.

2. Choose a value of $B \in [0,1]$.

3. Find the angle $\theta \in [0, \pi/2]$ that results in the segment with length B such as in Figure 22. We can see in the same figure that this angle will be given by equation

$$\sin\theta = \frac{\text{opposite}}{\text{hypotenuse}} = \frac{B}{1} = B. \tag{4.10}$$

4. Using the angle θ, obtain the velocity vectors of each droplet from Figure 22. They are given by

$$\mathbf{u}_1 = \frac{1}{2}[\cos(-\theta),\ \sin(-\theta)], \tag{4.11}$$

$$\mathbf{u}_2 = \frac{1}{2}[\cos(\pi-\theta),\ \sin(\pi-\theta)]. \tag{4.12}$$

   Note that, in this manner, the two droplets will always have exactly opposite directions. We also employed a 0.5 factor in equations (4.11)-(4.12) so that the relative vector will have $||\mathbf{u}_r|| = 1$.

A computational domain with $10D \times 10D$ based on a uniform mesh with dimensionless mesh size $h = 0.025$ is adopted in the simulations. In particular, the droplets are located in a two-dimensional coordinate system.

Figure 22 – Initial geometry setup for a binary droplet collision simulation. In this computational setup, the dimensionless lengths were defined using the droplet diameter, D, as characteristic quantity.

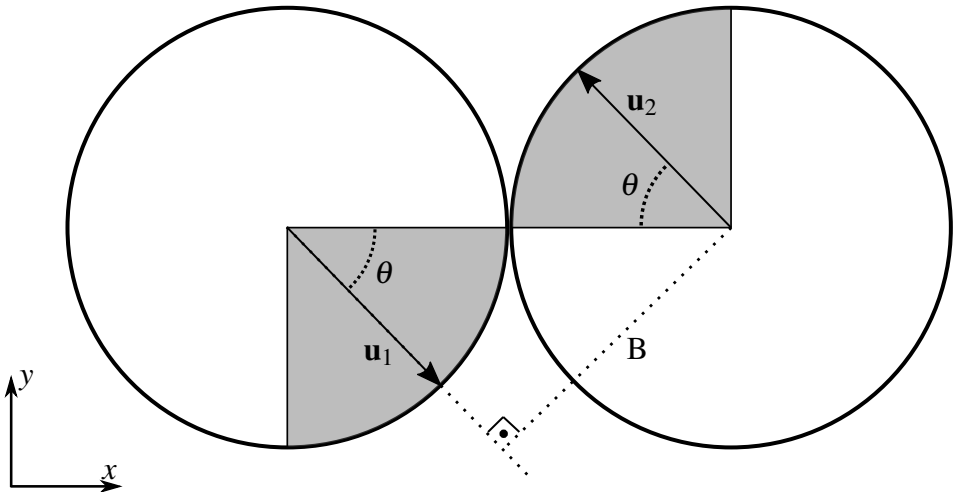

Source: Elaborated by the author.

4.3 Validation of the numerical methodology

4.3.1 Newtonian fluids

The first validation test was made comparing numerical results obtained with our code with experimental predictions for Newtonian fluids. In particular, following the work of Planchette et al. (PLANCHETTE *et al.*, 2017), we have captured the ratio of two time scales, t_{Dmax}/t_{oscill}. In this case, t_{Dmax} is the time needed for the coalesced droplet to reach its maximal diameter $Dmax$; the quantity $t_{oscill} = \sqrt{\rho D^3/\gamma}$ is the oscillation time scale. In Fig. 23, we present results for the numerical predictions of t_{Dmax}/t_{oscill} as a function of We (blue stars) together with the semi-empirical fit described by Planchette et al. (PLANCHETTE *et al.*, 2017) (solid orange line). Both results show a high decay of the ratio t_{Dmax}/t_{oscill} with respect to We for low values of the Weber number ($We \leq 10$) and a less intense decay for higher values of We. We can notice a higher agreement for low values of the Weber number in the regime where capillary forces dominate. When inertial effects become more significant the two curves detach from each other. While the numerical results present a more asymptotic behavior near $t_{Dmax}/t_{oscill} = 0.47$, in the experimental fit, this ratio keeps decreasing, although less intensely, for values between 0.3 and 0.4 in the range $We \in [20, 50]$. Part of the explanation for this discrepancy can be attributed to 3D effects not captured by the 2D numerical simulations. The oscillation time in the 2D case increases, since it scales with $\sqrt{\rho L D^2/\gamma}$, where L is the height of the cylinder. In addition it seems that the time to achieve D_{max} would be lower, due to a less resistant surface tension force, with only one curvature, since the other would vanish.

We perform a numerical experiment for an additional important validation which is the reproduction of experiment outcomes (like bouncing, coalescence, stretching separation) in

Figure 23 – Comparison between the numerical results and the semi–empirical time scale of Planchette et al. (PLANCHETTE *et al.*, 2017) for the ratio t_{Dmax}/t_{oscill} versus We. Parameters (S.I. units): $D = 0.0005$, $\rho = 948$, $\eta_s = 0.03$, $\sigma = 0.02$ and U is varied in the interval $[0.02, 2.90]$. The dimensionless numbers fixed in the simulations are $B = 0$ and $\beta = 1$.

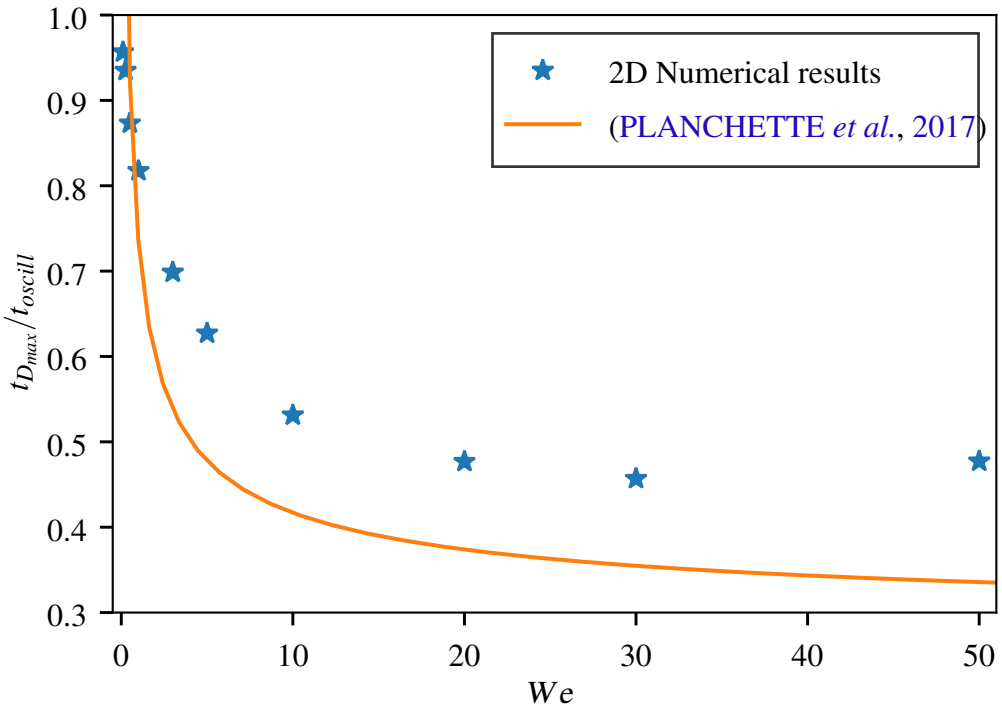

Source: Elaborated by the author.

the map of parameters B and We. Based on the recent experimental results of Al-Dirawi and Bayly (AL-DIRAWI; BAYLY, 2019), we have simulated a Newtonian fluid considering the physical properties of a 4 % HPMC material: $\rho = 998\text{kg m}^{-3}$, $\gamma = 45.8\text{mNm}^{-1}$ and $\mu = 8.2\text{mPa s}$. In our simulations, we have adopted the droplet diameter as $D = 3.75 \times 10^{-4}\text{m}$. According to the 4 % HPMC regime map presented by Al-Dirawi and Bayly (AL-DIRAWI; BAYLY, 2019), it is expected a bouncing effect for the pair $(B, We) = (0.2, 10)$, a coalescence result for $(B, We) = (0, 30)$ and the separation of the droplets with $(B, We) = (0.5, 70)$. From Fig. 24, we can verify that the corresponding expected outcomes are well captured by our numerical methodology in these cases. In order to further validate the code using a mesh refinement study, we have also included in Fig. 24 results for two different meshes, e.g. black line for the non-dimensional value $h = 0.025$ and red line for the non-dimensional value $h = 0.0125$. It is worth noticing that the results for both meshes are very similar for the selected simulation times. Therefore, from now on, in our simulations we will adopt the dimensionless mesh size of $h = 0.025$ since the results in Fig. 24 attest the numerical convergence of the method.

Figure 24 – Transient dynamic of the interface for three different outcomes: bouncing (left), coalescence (middle) and separation (right). The black interfaces represent the results for the mesh size $h = 0.025$ while the red interfaces describe the results for the mesh size $h = 0.0125$. Parameters (S.I units): $D = 0.000375$, $\rho = 998$, $\eta_s = 0.0082$, $\sigma = 0.0458$, $\beta = 1$ and U is varied as U=$\{1.106,\ 1.916,\ 2.926\}$. The non-dimensionals are $Oh = 0.063$, while We and Re are taken as the pairs $(We, Re) = (10, 50.49), (30, 87.45), (50, 133.58)$.

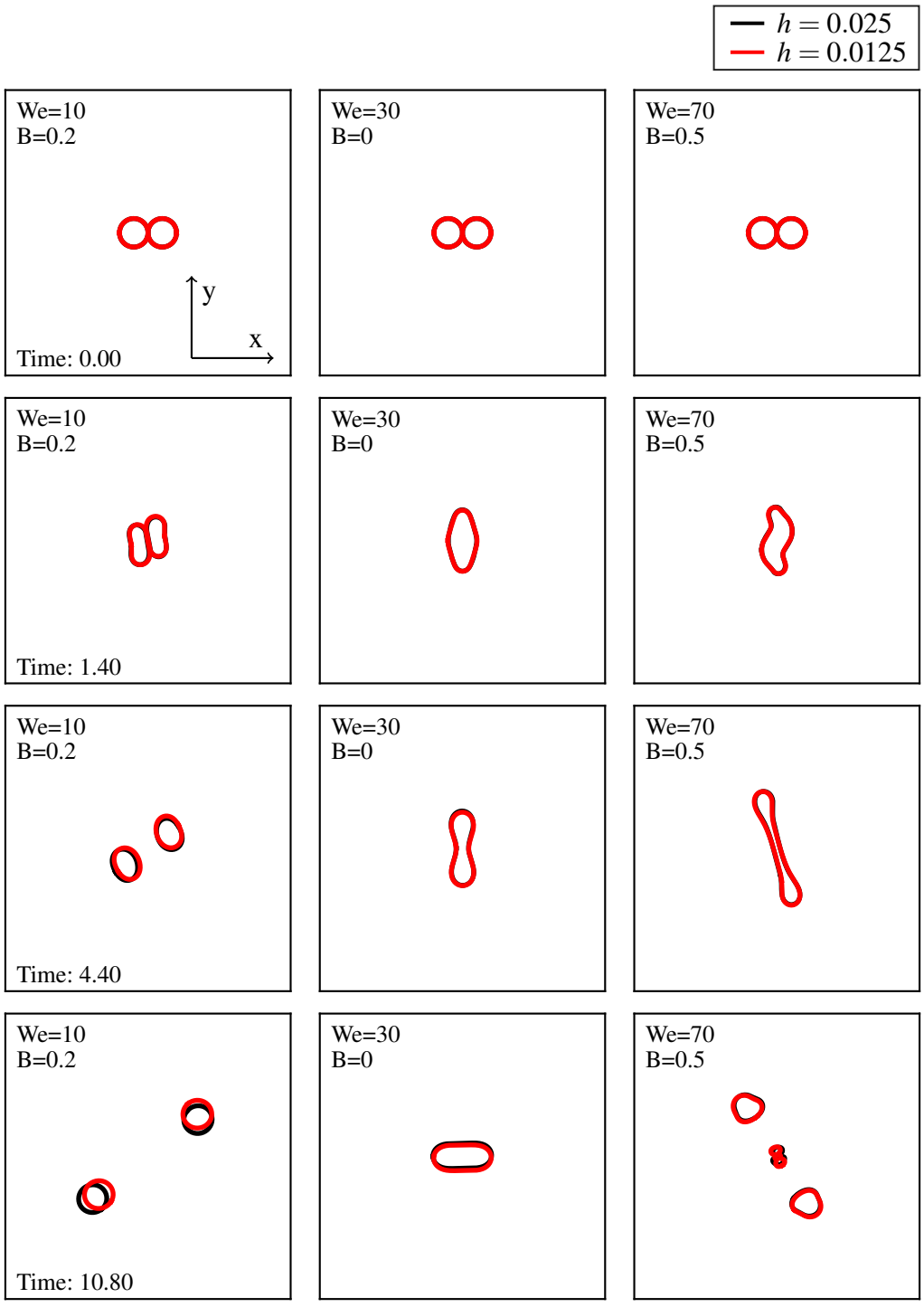

Source: Elaborated by the author.

4.3.2 Shear-thinning fluids

In the second round of validations, we have reproduced numerical results considering the coalescence case of shear-thinning fluids. A numerical–numerical comparison was performed between the modified SPH of Xu et al. (XU; TANG; YU, 2020) and the front-tracking/marker-and-cell approach of this current work. For this comparison, we simulated the head-on binary collision using the same viscosity function adopted in (XU; TANG; YU, 2020), the Cross fluid model, with the same parameters: $\eta_0 = 1$, $\eta_\infty = 0.1\eta_0$, $K = 1$, and $m = 0.1$. The dimensionless numbers adopted in the simulation were $Re = 26.7$ and $We = 7.5$. We can see from Fig. 25 that the time variations of the thickness along the y-axis and the x-axis obtained by both methods exhibits quite similar behaviours. Since the Smoothed Particle Hydrodynamics and the front-tracking/marker-and-cell are very different approaches, we can consider that the validation was successful.

Figure 25 – 'on of the x and y-thickness: blue curves are used to represent the numerical results for the current work while the results for the modified SPH scheme of (XU; TANG; YU, 2020) are plotted using orange curves. These simulations assume the cross-model for the viscosity function. Parameters (reduced units): $D = 25.04$, $U = 0.6$, $\rho = 1.78$, $\sigma = 2.13$, $\eta_0 = 1$, $\eta_\infty = 0.1$, $K = 1$, $m = 1$. The non-dimensionals are: $Re = 26.74$, $We = 7.53$ and $Oh = 0.102$.

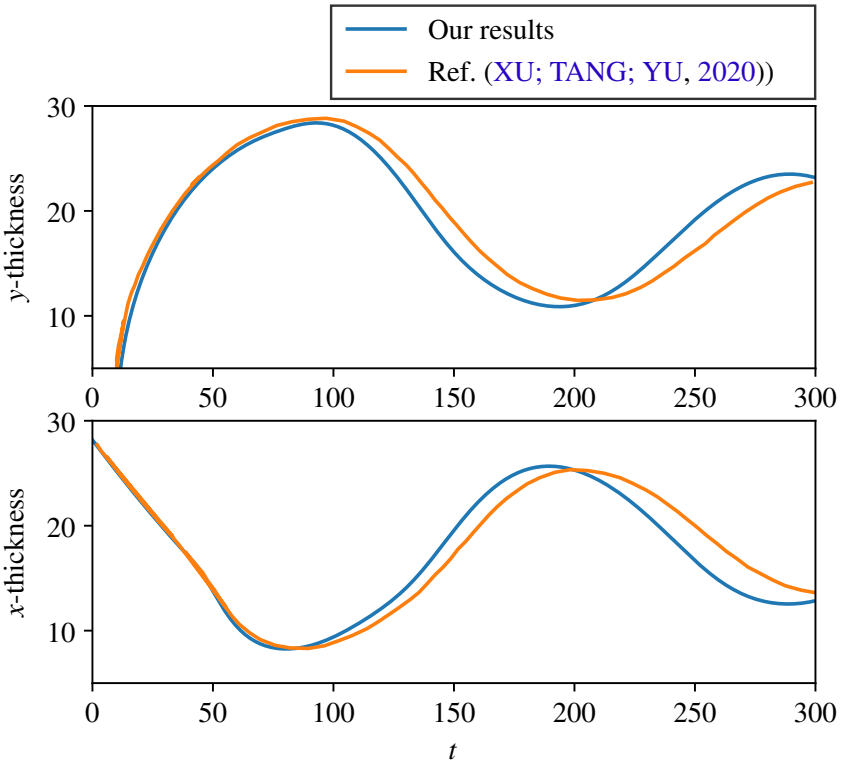

Source: Elaborated by the author.

As a further qualitative study, the code was checked against the experimental results described by Finotello et al. (FINOTELLO *et al.*, 2018). In that work, the authors used the Carreau-Yasuda (CY) model to fit the viscosity function response of a Xanthan solution, assuming

the following rheological parameters: $\eta_0 = 0.228$Pa s, $\eta_\infty = 0.0025$Pa s, $\lambda_{cu} = 3.29$s, $n = 0.4$ and $a = 9.4$. The surface tension of the material was considered as $\gamma = 72.2$mNm^{-1} while $\rho = 1000$kg m^{-3} and $D = 1.02 \times 10^{-3}$m. For a comparison, we simulated a GNF model with the CY viscosity function with the same values for λ, n, η_0, and η_∞. Figure 26 shows output categories in a map in the $\{We, B\}$ space obtained with our simulations, right subfigure, together with the experimental outputs (FINOTELLO *et al.*, 2018), left subfigure. We can notice that, for low values of the Weber number, where capillary effects are more significant, the numerical simulations captured quite well the outcomes of *Bouncing* and *Coalescence*. However, for high *We* values, where the surface tension effects are less important, the boundary between *Coalescence* and *Separation* was predicted for higher values of B in the numerical case. The reasons for this discrepancy can be associated with a variety of sources. First, from the comparison with the Newtonian case illustrated in Fig. 23, we observed that the difference between 2D and 3D approaches becomes more significant as the Weber number gets higher. In addition, it is important to notice that the fluid employed by Finotello et al. (FINOTELLO *et al.*, 2018) exhibits other non-Newtonian effects besides shear–thinning. Elasticity is important at least as far as extensional properties are concerned, as highlighted by the authors. In this regard, it would be interesting to advance towards more sophisticated viscoelastic models that exhibit shear–thinning effects, but can also predict extensional–thickening as well as other features of a viscoelastic solutions.

Figure 26 – Experimental (left) and numerical (right) regime map for the CY model considering $n = 0.4$. The experimental results were obtained from (FINOTELLO *et al.*, 2018). Parameters (S.I. units): $D = 0.00102$, $\rho = 1000$, $\sigma = 0.072$, $\eta_0 = 0.228$, $\eta_\infty = 0.0025$, $\eta_{app} = 0.0038$, $\lambda = 3.29$, $a = 9.4$, $n = 0.4$, $U \in [0.838,\ 2.653]$. The non-dimensionals are $Oh = 0.014$, while We and Re are taken as the pairs $(We, Re) = (10, 225.88)$, $(20, 319.44)$, $(30, 391.23)$, $(45, 479.16)$, $(55, 529.73)$, $(90, 677.63)$, $(100, 714.29)$.

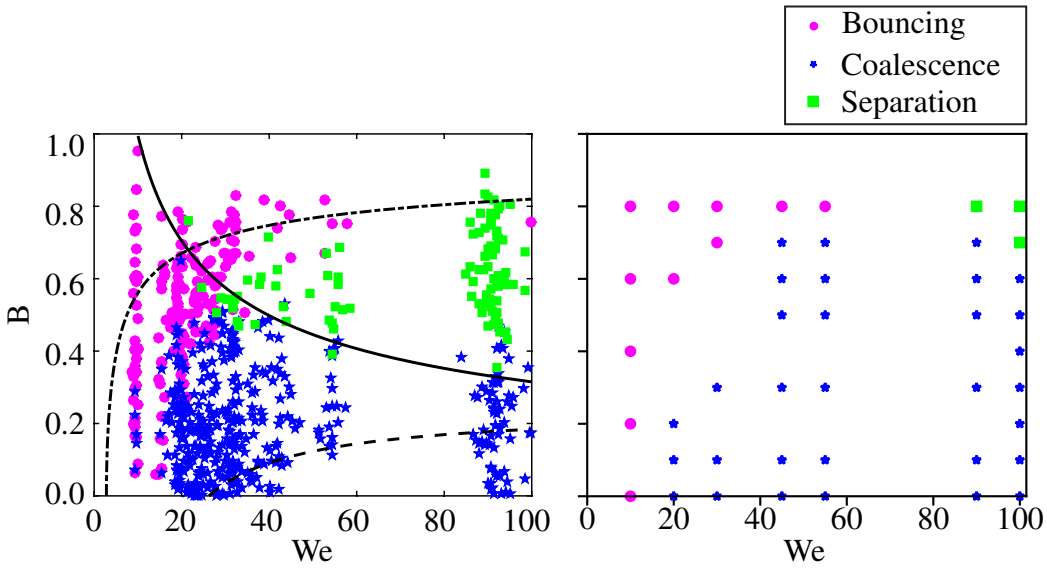

Source: Elaborated by the author.

4.4 Results

4.4.1 Shear–thinning

The study of Finotello et al. (FINOTELLO *et al.*, 2018) did not consider the effect of the changing the power law index, maintaining $n = 0.4$ for all experiments. In Fig. 27 we show the outputs associated with *Bouncing*, *Coalescence*, and *Separation* for four values of the power–law index, $n = 0.1$, $n = 0.4$, $n = 0.7$, and $n = 1$.[1] We notice that, for $We <\approx 60$, there are no differences among the maps. For $We \geq 90$, however, we can notice a trend to increase the tendency of *Separation* as n decreases and we get farther from the Newtonian case. Although the outcomes between the cases of $n = 0.7$ and $n = 1$ were the same, from the perspective of the collision dynamics, the two droplet collisions evolve in a different manner (not shown here). The comparison between $n = 0.4$ and $n = 0.1$ shows a decrease in the critical value of B where there is a transition from *Separation* to *Coalescence*, for the more shear–thinning case.

In order to illustrate the interface dynamic for different values of n, we have plotted in Fig. 28 the evolution of the binary droplet collision for $n = 0.1$, $n = 0.4$, and $n = 0.7$, where each frame corresponds to different instant. For time=1.20, we notice that the two drops are coalesced forming an approximately unique configuration. In time=3.20 we observe a stretched configuration with some discrepancy between the different cases. Here we notice that the more shear–thinning case ($n = 0.1$) exhibits a more stretched configuration, while the less shear–thinning case ($n = 0.7$) shows the opposite trend. This happens because as the fluid becomes more shear–thinning, there is a decrease in the associated viscous dissipation enabling more energy to induce stretching. In the next frame, at time=5.30, the $n = 0.1$ shear–thinning fluid breaks forming two separated structures. This outcome is observed for the intermediate case of $n = 0.4$ at time=6.90. Even letting time evolve, we do not see a *Separation* outcome for $n = 0.7$.

4.4.2 Oldroyd–B

The Oldroyd–B model was employed to capture viscoelastic effects in the binary droplet collision problem. In Fig. 29, we show the outcomes corresponding to *Bouncing*, *Coalescence*, and *Separation* in the $\{Wi, We\}$ space for three values of B, $B \in \{0; 0.4; 0.8\}$. The *Bouncing* output is obtained for the lower value of We in all the B cases analyzed. For the head–on collision, no *Separation* was found. As the collision becomes more oblique, more *Separation* outputs occur. This tendency affects higher values of Weber and low values of Weissenberg. This result can be explained by the fact that not only surface tension, but also the fluid elastic character acts to maintain the integrity of the resulting drop after collision. For an even higher value of the impact factor, $B = 0.8$, we notice that *Separation* is the rule, even for high values of Wi. The exception

[1] Since the space displayed here is the $\{We, B\}$ space, the criticism raised by (THOMPSON; OISHI, 2021) with respect to the changes in n does not apply to the present analysis

Figure 27 – Outcomes of *Bouncing* (magenta), *Coalescence* (blue), and *Separation* (green) in the $\{We, B\}$ space for shear thinning case with different levels of power-law index, corresponding to $n = \{0.1; 0.4; 0.7; 1\}$. Parameters (S.I. units): $D = 0.00102$, $\rho = 1000$, $\sigma = 0.072$, $\eta_0 = 0.228$, $\eta_\infty = 0.0025$, $\eta_{app} = 0.0038$, $\lambda = 3.29$, $a = 9.4$, $U \in [0.838,\ 2.653]$ and n is indicated above each map. The non-dimensionals are $Oh = 0.014$, while We and Re are taken as the pairs $(We, Re) = (10, 225.88)$, $(20, 319.44)$, $(30, 391.23)$, $(45, 479.16)$, $(55, 529.73)$, $(70, 597.61)$, $(80, 638.88)$, $(90, 677.63)$, $(100, 714.29)$.

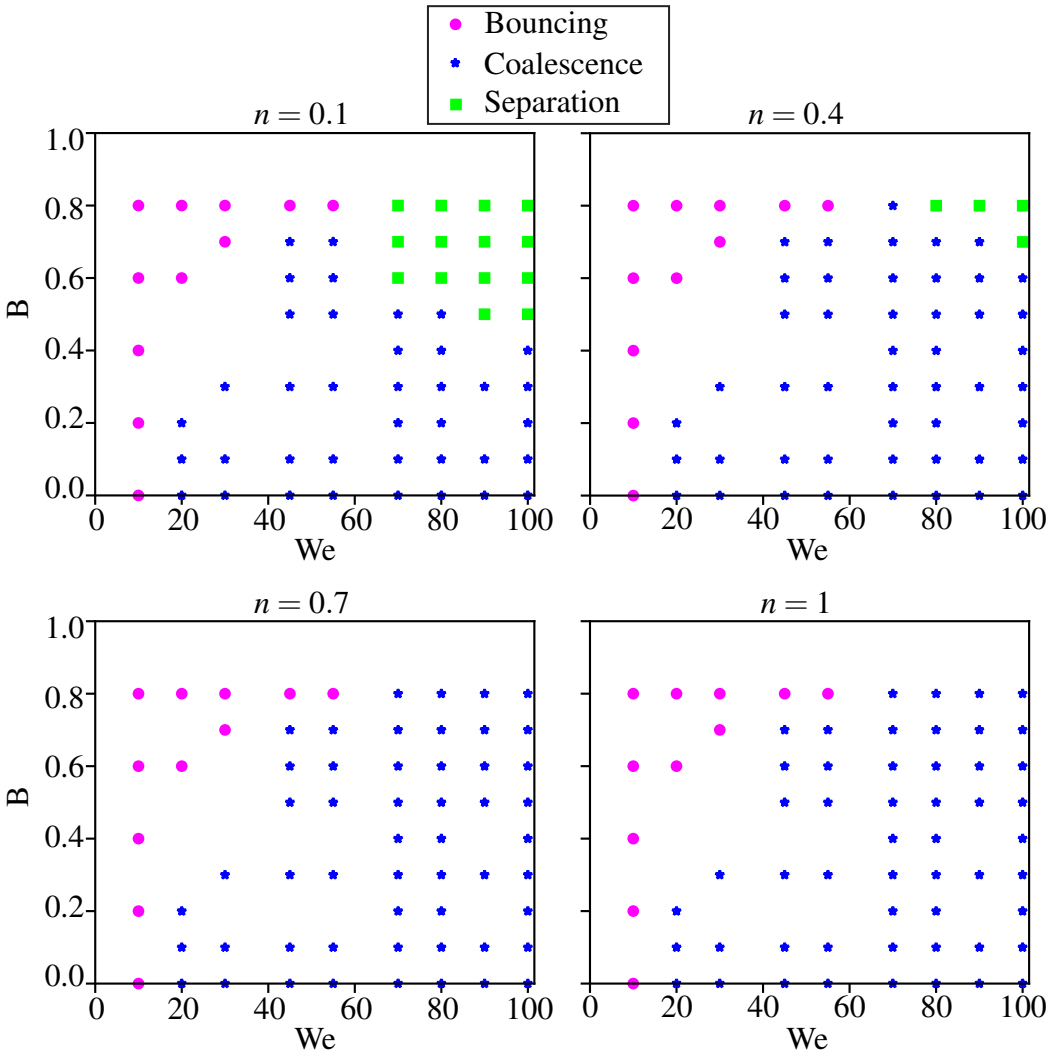

Source: Elaborated by the author.

occurs for low values of We solely, where surface tension effects are significant and the merged drop formed after collision is maintained.

This tendency is seen from a perspective that highlights the role of elasticity in Fig. 30. This figure maintains the usual $\{We, B\}$ for each value of Wi. The Newtonian map in the top–left subfigure is transformed onto other maps as elastic effects become more intense, with $Wi = 1$ (top–right subfigure), $Wi = 2$ (bottom–left subfigure) and $Wi = 3$ (bottom–right subfigure). We can notice again that the increase of elastic effects inhibits the *Separation* output. This effect appears first in cases of low values of B and low values of We, since more oblique collisions

Figure 28 – Transient dynamics of the interface for $B = 0.8$, $Re = 714.29$, $We = 100$, $Oh = 0.014$ and different values of n: $n = 0.1$ (black), $n = 0.4$ (red), and $n = 0.7$ (blue). Other parameters (S.I. units): $D = 0.00102$, $\rho = 1000$, $\sigma = 0.072$, $\eta_0 = 0.228$, $\eta_\infty = 0.0025$, $\eta_{app} = 0.0038$, $\lambda = 3.29$, $a = 9.4$, $U = 2.653$.

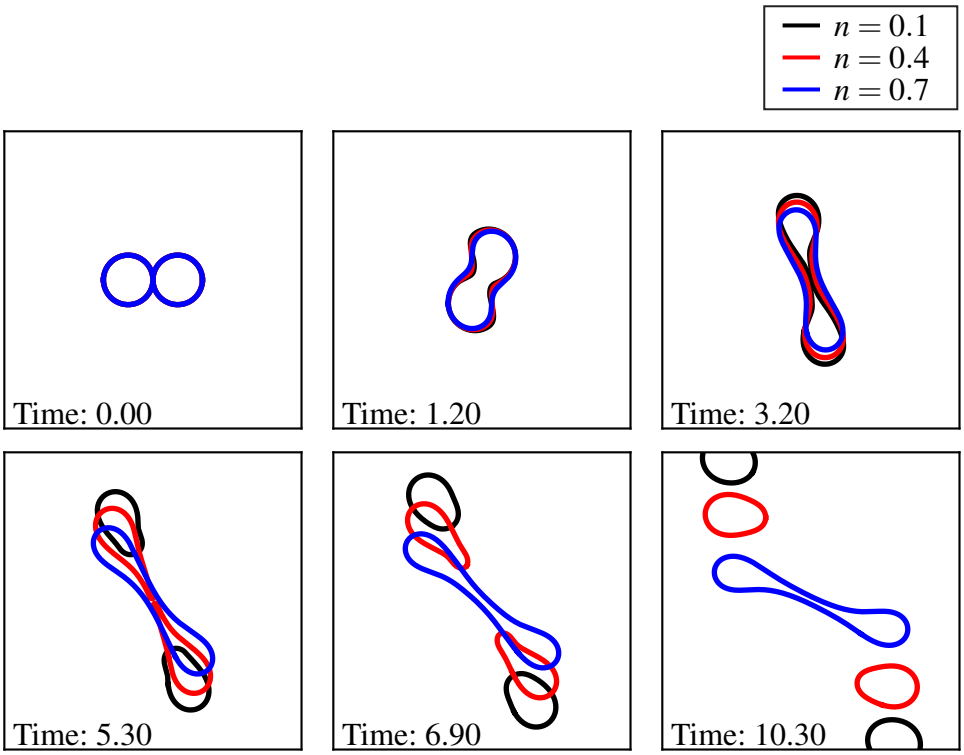

Source: Elaborated by the author.

favour *Separation* and higher values of surface tension favour the maintenance of the integrity of the coalesced drop.

The interface evolution in time of the droplet collision of Oldroyd–B fluid is illustrated in Figs. 31 and 33. The bouncing regime is shown in Fig. 31 in a side-by-side comparison between a Newtonian and the Oldroyd–B simulation with $Wi = 5$. Although both fluids exhibit similar qualitative behaviors, the viscoelastic droplets experience larger deformations during the whole trajectory in time. This happens because the elastic character of the fluid turns it more flexible leading to elastic deformations not present in the Newtonian case. To illustrate this more clearly, Fig. 32 shows the maximum radius of one of the droplets over time. The viscoelastic droplet clearly deforms more at the moment of impact. In addition, the elastic nature of the fluid induces oscillations of higher amplitude and for much longer times, showing less influence of dissipative terms. On the other hand, the Newtonian droplet quickly stabilizes into a circular shape, due to the high surface tension and dissipation.

Figure 33 shows the interface dynamics in coalescence/separation regimes for $Wi = \{1.5; 3.0\}$ and the Newtonian case for comparison. The Weber and impact numbers are fixed at $\{We, B\} = \{40, 0.6\}$. There, we can see how elasticity affects the outcome. Until time=5.30,

Figure 29 – Outcomes of the Oldroyd–B droplet collision corresponding to *Bouncing*, *Coalescence*, and *Separation* in the $\{Wi, We\}$ space for different values of the impact factor, $B = \{0; 0.4; 0.8\}$. Non-dimensional parameters: $\beta = 1/9$, $Wi = \{0,1,2,3,4,5\}$, $B = \{0, 0.4, 0.8\}$, $Oh = 0.063$, Re and We are taken as the pairs $(We, Re) = (10, 50.49)$, $(30, 87.45)$, $(40, 100.98)$, $(50, 112.89)$, $(60, 123.67)$, $(70, 133.58)$.

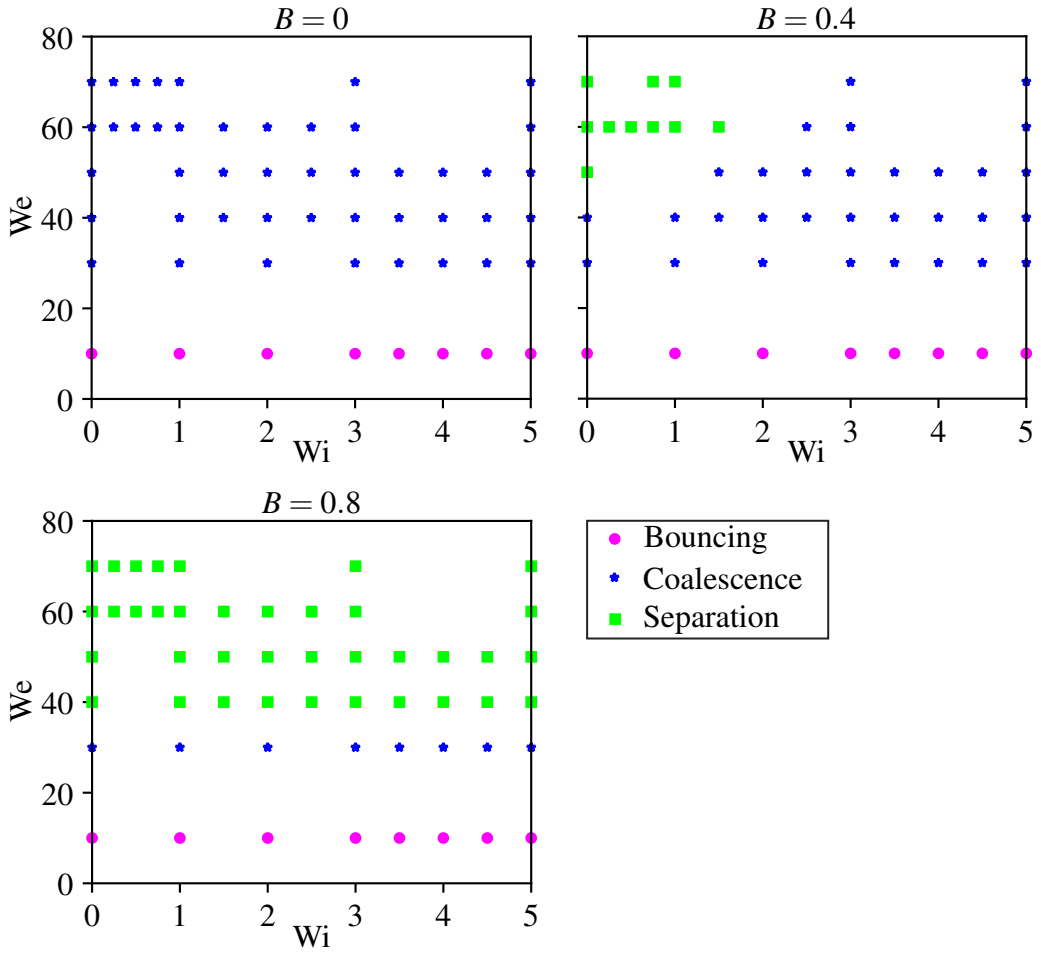

Source: Elaborated by the author.

the three cases are more or less coincident. At time=7.90, we can see that the Newtonian case presents a more stretched configuration, while the elastic effects of the Oldroyd–B fluid impose some resistance to this stretching. At the subsequent frame, corresponding to time=9.0, the Newtonian case exhibits a *Separation* into two droplets, while both viscoelastic cases show a single structure. At time=12.90, we can see that the structures associated with the viscoelastic cases have changed their orientation, revealing a retraction and a subsequent stretching in this other direction.

4.4.3 PTT

In Fig. 34 we show Phan-Thien-Tanner results for the head–on binary droplet collision ($B = 0$) with two values of the extensibility parameter, $\varepsilon = 0.05$ and $\varepsilon = 0.25$ for the map

Figure 30 – The $\{We, B\}$ map of outputs in the collision of two identical droplets of an Oldroyd–B fluid for different values of Wi. Non-dimensional parameters: $\beta = 1/9$, $Wi = \{0,1,2,3\}$, $B = \{0, 0.2, 0.4, 0.6, 0.8\}$, $Oh = 0.063$, Re and We are taken as the pairs $(We, Re) = (10, 50.49)$, $(30, 87.45)$, $(40, 100.98)$, $(50, 112.89)$, $(60, 123.67)$, $(70, 133.58)$.

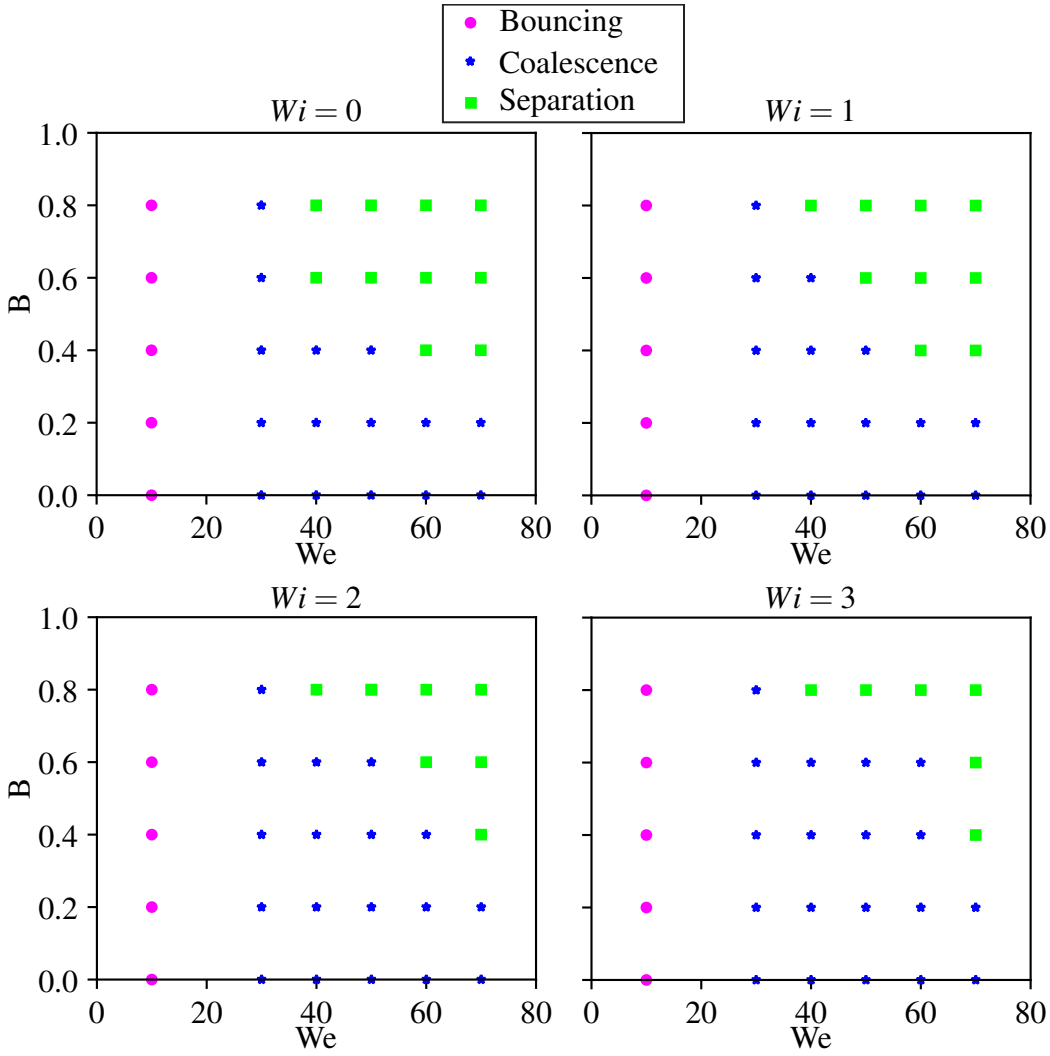

Source: Elaborated by the author.

$\{Wi, We\}$. Here we can notice that increasing ε favours the *Separation* outcome, specially for low values of the Weissenberg number and high values of the Weber number. This fact is in accordance with the previous results. Firstly because elastic and surface tension effects inhibit *Separation* and secondly because shear–thinning effects, as reported previously, favour *Separation*. Since in the PTT model the viscosity function becomes more shear–thinning for higher values of ε, an increase in the extensibility factor induces the obtained outcome.

A comparison between the interface dynamics considering the same two values of the extensibility parameter, $\varepsilon = 0.05$ and $\varepsilon = 0.25$, are presented in Fig. 35, but now with an oblique collision of $B = 0.3$. Weber and Weissenberg numbers were set to $We = 50$ and $Wi = 2.5$, respectively. We can notice that for time $t \approx 6.8$, the higher extensibility parameter case, $\varepsilon = 0.25$,

Figure 31 – Transient dynamic of the interface for the Oldroyd–B case with fixed values of $B = 0.2$, $We = 10$, $Re = 50.49$, $Oh = 0.063$, $\beta = 1/9$. Black: Newtonian and red: Oldroyd-B with $Wi = 5$.

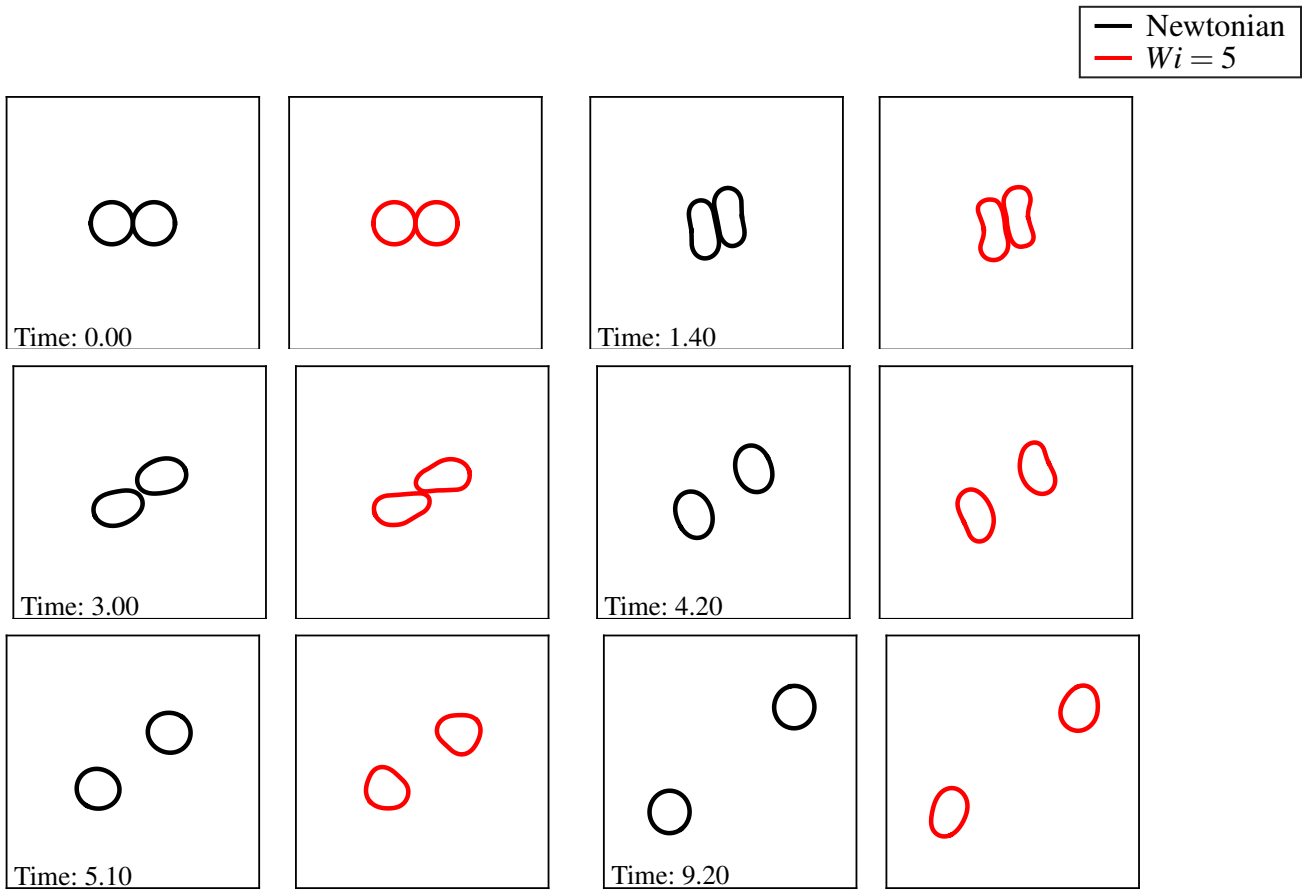

Source: Elaborated by the author.

is more stretched, leading to an eventual rupture in $t \approx 7.7$. On the other hand, for $\varepsilon = 0.05$, after achieving a maximum stretched configuration with no *Separation*, the merged drop experiences a retraction motion and a subsequent stretching in another direction. Again, the role of ε seems to be associated with a higher shear–thinning effect, causing less viscous dissipation and promoting more stretching and hence, increasing the tendency of *Separation*.

Another set of results concerning the droplet collision of a PTT fluid, but now including oblique collision is shown in Fig. 36 for $\varepsilon = 0.25$. The outcome maps are again displayed in the $\{Wi, We\}$ space. While in general, the increase of the impact factor induces the *Separation* outcome, as can be noticed when we compare the maps corresponding to $B = 0$ and $B = 0.3$, a non-monotonic behavior is also revealed. Looking at the $We = 40$ row, we can notice that while from $B = 0$ to $B = 0.1$ the *Coalescence* outcomes corresponding to $Wi = 2.5$ and $Wi = 2$ turned into *Separation* outcomes, increasing again to $B = 0.2$, reversed these changes. A subsequent increase to $B = 0.3$ turned again these cases into *Separation* outcomes. A similar trend occurred for $We = 30$. The gradual retraction of the *Coalescence* outcomes increasing B from 0.0 to 0.2

Figure 32 – Max radius over time for a bouncing simulation with fixed values of $B = 0.2$, $We = 10$, $Re = 50.49$, $Oh = 0.063$, $\beta = 1/9$. Black: Newtonian and red: Oldroyd-B with $Wi = 5$.

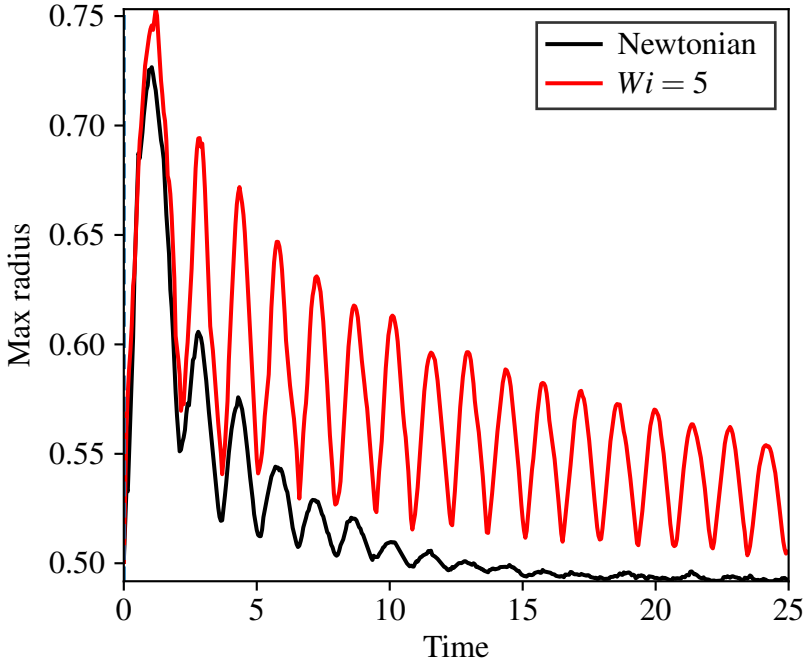

Source: Elaborated by the author.

was reversed when B was set 0.3. This nonlinear response with respect to the impact factor seems to be associated with the competing effects of shear–thinning and elasticity that are present in the PTT model and absent in pure shear–thinning and purely elastic models previously analyzed. Above a certain critical Weber number, the elastic effects are stronger when B is increased. However, when We is low, it seems that the elasticity increase does not have the same effect since the surface tension is already handling a certain level of integrity of the merged drop. Hence, in this scenario, the shear–thinning effects are more pronounced.

Finally, we concluded our numerical investigations illustrating the dynamic interfaces of two pair of droplet of PTT fluids with the same rheology and characteristic velocity, but with different impact factors, $B = 0.0$ and $B = 0.3$. Figure 37 shows how the angle at the impact can be determinant to induce *Separation* or *Coalescence*, even when surface tension ($We = 30$) and elastic effects ($Wi = 4$) are significant. The oblique case has already given signs of superior stretching at time $t \approx 4.20$, and at time $t \approx 5.70$ we can see a *Separation* outcome. In a different manner, the head-on case exhibited a *Coalescence* outcome, preserving the integrity of the merged drop throughout its evolution.

4.5 Conclusions

In the present work we investigated the binary droplet collision problem for different non–Newtonian fluids: a generalized Newtonian fluid with the Carreau-Yasuda viscosity function, the Oldroyd–B viscoelastic model, and the Phan-Thien-Tanner viscoelastic model.

Figure 33 – Transient dynamic of the interface for the Oldroyd–B case with fixed values of $B = 0.6$, $We = 40$, $Re = 100.98$, $Oh = 0.063$, $\beta = 1/9$. The black interfaces represent the Newtonian limit case, while the red and blue interfaces correspond to $Wi = 1.5$ and $Wi = 3$, respectively.

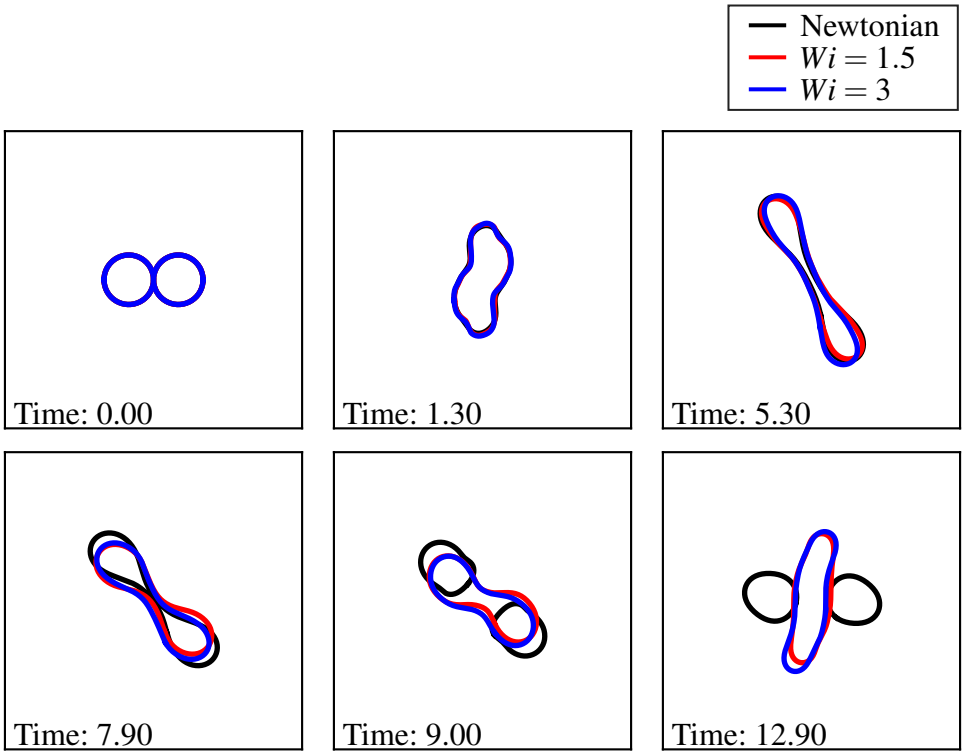

Source: Elaborated by the author.

The parameters of the Carreau-Yasuda model were taken from the experimental work developed by Finotello et al. (FINOTELLO *et al.*, 2018). The comparison of the outcomes, *Bouncing*, *Coalescence*, and *Separation*, in the $\{We, B\}$ map between numerical and experimental results had a better agreement in the low Weber range, where capillary forces are more significant. A part of the discrepancy can also be attributed to the fact that our formulation is 2D. For intermediate and high values of We, the numerical frontier between *Coalescence* and *Separation* occurs for higher values of the impact factor. We found that more shear–thinning fluids are less able to keep in the *Coalescence* regime, since shear–thinning fluids have less viscous dissipation, what in turn leads to more stretched configurations, which are more likely to experience a rupture. This explanation was corroborated by the evaluation of the interface dynamics of the CY droplets.

Examining the Oldroyd–B fluid simulations, we could observe that, as surface tension effects, elasticity tends to keep the integrity of the coalesced drop, avoiding *Separation*, by containing the drops stretching. This result corroborates some findings in the literature (e.g. (OISHI; THOMPSON; MARTINS, 2019a)), where elastic effects in viscoelastic fluids can play the role of surface tension effects in inelastic ones. Again, the interface dynamics support this conjecture, showing less stretched configurations for higher elastic fluids, as captured by the Weissenberg number.

Figure 34 – The $\{We, Wi\}$ map of outputs in the collision of two identical droplets of a PTT fluid for different values of ε. Non-dimensional parameters: $B = 0$, $\beta = 1/9$, $Wi = \{0, 1, 2, 3, 3.5, 4, 4.5, 5\}$, $Oh = 0.063$, $\varepsilon = \{0.05, 0.25\}$, Re and We are taken as the pairs $(We, Re) = (10, 50.49)$, $(30, 87.45)$, $(40, 100.98)$, $(50, 112.89)$, $(60, 123.67)$, $(70, 133.58)$.

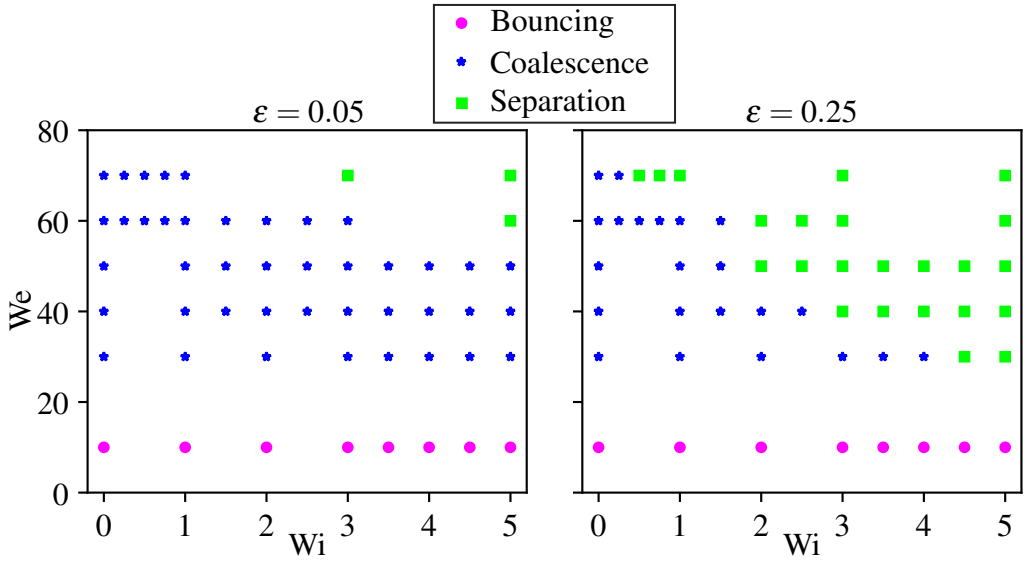

Source: Elaborated by the author.

Finally, the performance of the PTT model was also analyzed in this problem. Previous results concerning shear–thinning and elastic effects were reinforced by the PTT simulations. In addition, we found some non-monotonic behavior increasing the impact parameter that can be explained by this dual character of the PTT model, where shear-thinning and elasticity have opposite effects on the tendency to separate the merged drop formed after collision. This aspect of the results needs further investigation in order to address the influence of each effect more systematically.

Due to the lack of experiments, our numerical results can be considered as an alternative form to study bouncing, coalescence, and separation of viscoelastic binary droplets undergoing off-center collisions. Despite the employment of a two-dimensional formulation, the current study is the first initiative to understand the role of elasticity in this problem by considering cases with and without shear–thinning effects. Hence, this investigation can be helpful to provide means for choosing among different fluids in processes that can be optimised if a certain outcome (bouncing, coalescence, separation) is the most desirable.

Figure 35 – Transient dynamic of the interface for the PTT case with fixed values of $B = 0.3$, $We = 50$, $Re = 112.89$, $Oh = 0.063$, $\beta = 1/9$ and $Wi = 2.5$. The black and red interfaces correspond to $\varepsilon = 0.05$ and $\varepsilon = 0.25$, respectively.

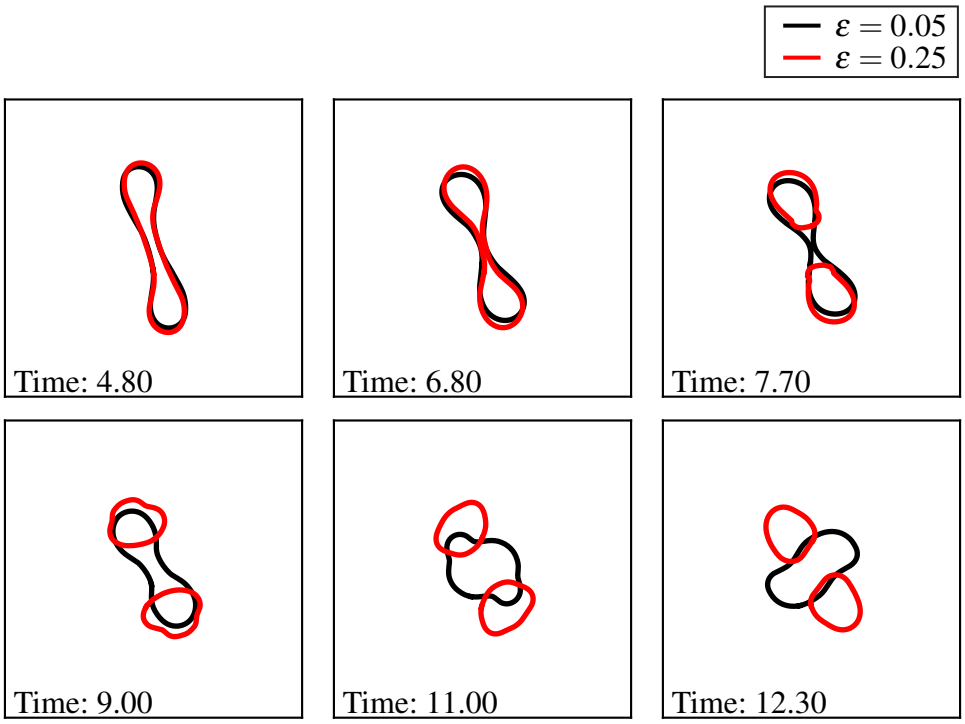

Source: Elaborated by the author.

Figure 36 – The $\{We, Wi\}$ map of outputs in the collision of two identical droplets of a PTT fluid for different values of B. Non-dimensional parameters: $B = \{0, 0.1, 0.2, 0.3\}$, $\beta = 1/9$, $Wi = \{0, 1, 2, 3, 3.5, 4, 4.5, 5\}$, $Oh = 0.063$, $\varepsilon = 0.25$, Re and We are taken as the pairs $(We, Re) = (10, 50.49),\ (30, 87.45),\ (40, 100.98),\ (50, 112.89),\ (60, 123.67),\ (70, 133.58)$.

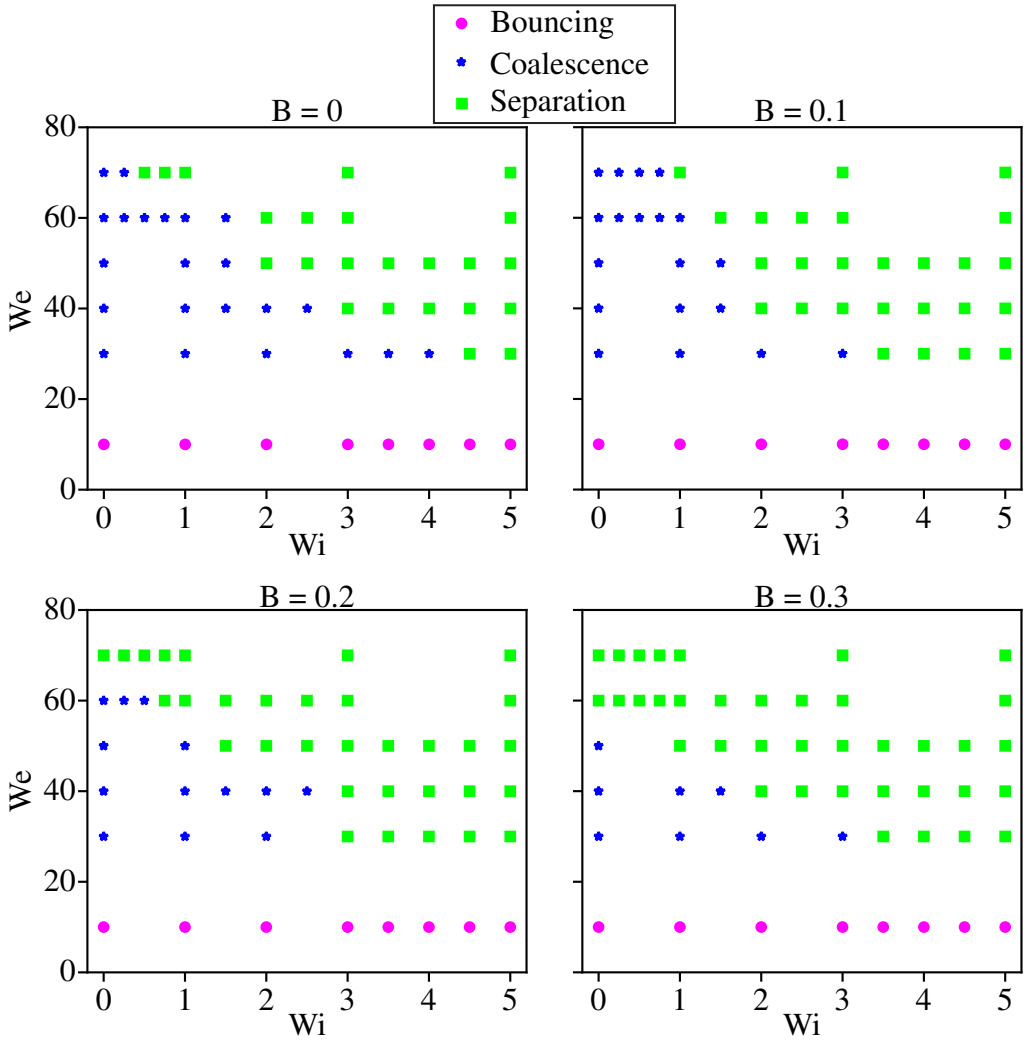

Figure 37 – Transient dynamic of the interface for the PTT case with fixed values of $\varepsilon = 0.25$, $\beta = 1/9$, $We = 30$, $Re = 87.45$, $Oh = 0.063$ and $Wi = 4$. The black and red interfaces correspond to $B = 0$ and $B = 0.3$, respectively.

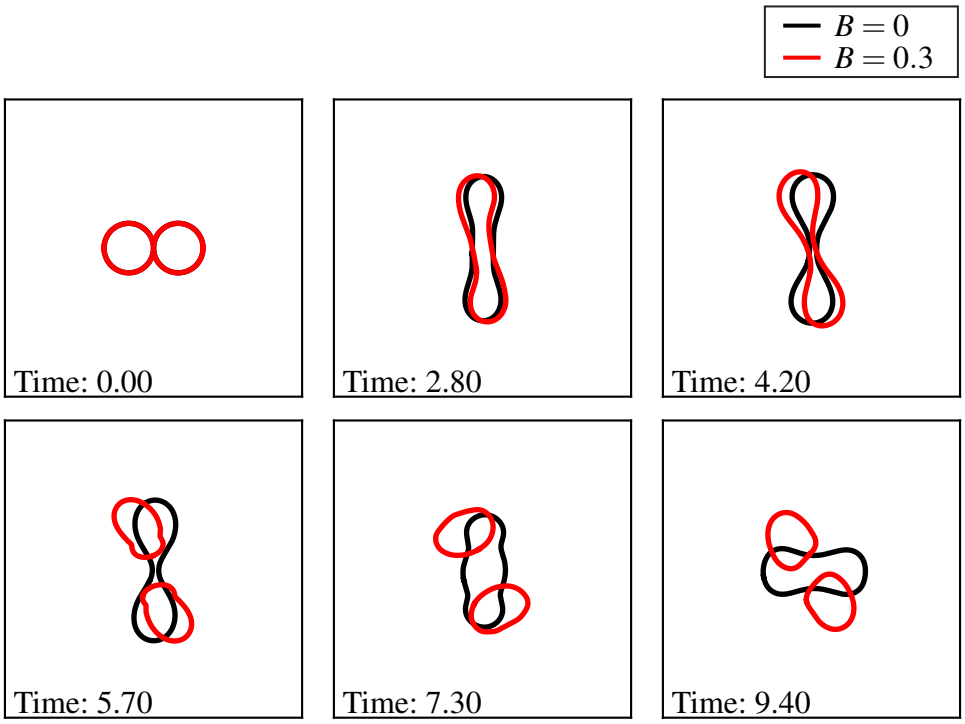

Source: Elaborated by the author.

CHAPTER

5

A MACHINE LEARNING STRATEGY FOR COMPUTING INTERFACE CURVATURE IN FRONT-TRACKING METHODS

The Front-Tracking (FT) scheme (GLIMM *et al.*, 1986; UNVERDI; G.TRYGGVASON, 1992) is considered a powerful methodology for solving complex fluid flows involving free surface/interface dynamics. Roughly speaking, the implementations on FT frameworks use a set of discrete markers (Lagrangian points) to represent the interface, and the surface tension effects can be numerically computed using the geometrical information from this data structure. Important progresses and improvements on FT implementations have been presented in the last decades for multi-phase codes (POPINET; ZALESKI, 1999; TRYGGVASON *et al.*, 2001) as well as for single-phase problems (MANGIAVACCHI *et al.*, 2005; TRYGGVASON; SCARDOVELLI; ZALESKI, 2011).

A particularly common strategy in the construction of FT codes is to choose a type of continuous curve (e.g., piecewise parabolic, cubic splines, etc) that will fit the discrete marker points. The analytical expression of this curve can be used to approximate the curvature. In contrast to classical implicit or Eulerian formulations (POPINET, 2018), e.g. Volume-of-Fluid (VOF) (HIRT; NICHOLS, 1981) and Level-Set (LS) (OSHER; SETHIAN, 1988), the estimation of the interface curvature in FT schemes is generally not considered a computational challenge. Particularly, in order to numerically compute the interface curvature in a FT framework, we can adopt approximation techniques using the Lagrangian markers, e.g., Frenet based methods (FEBRES; LEGENDRE, 2018) or curve approximation schemes (MANGIAVACCHI *et al.*, 2005; TAVARES *et al.*, 2020). However, some authors have already pointed out drawbacks on the accuracy (DU *et al.*, 2006) and stability (MANGIAVACCHI *et al.*, 2005) of curve approximation schemes. Therefore, new approaches to compute the curvature in FT schemes are still desirable in order to further improve the classical strategies.

Recently, an alternative strategy for computing curvature based on Machine Learning (ML) algorithms has been employed in the context of VOF schemes. The VOF-ML idea was originally presented by Qi et al. (QI *et al.*, 2019) to deal with two-dimensional problems while Patel el al. (PATEL *et al.*, 2019) have extended the method for solving 3D fluid flows. In VOF-ML frameworks, a neural network is modeled which receives local volume fractions as inputs, and then the interface curvature is predicted as an output. This network is trained using a large synthetic dataset composed from circles and spheres. The numerical results of Qi et al. (QI *et al.*, 2019) and Patel et al. (PATEL *et al.*, 2019) highlighted that these machine learning strategies can be considered as alternative tools for simulating surface-tension-driven flows. Following the ideas of Qi et al. (QI *et al.*, 2019), a Level-Set Deep Learning approach has been developed and used by Larios-Cárdenas and Gibou (LARIOS-CÁRDENAS; GIBOU, 2021; LARIOS-CáRDENAS; GIBOU., 2021) in order to calculate curvature more accurately based on the implicit level-set functions. In addition, a machine learning methodology has been also employed in (LIU; MORITA; ZHANG, 2020) to improve the simulations of multiphase flows in the context of the particle method.

According to the best of our knowledge, these learning strategies have never been employed for directly calculating the curvature of FT schemes. Therefore, our main motivation in this work is to present a simple adaptation of the VOF-ML scheme by Qi et al. (QI *et al.*, 2019) resulting in a FT-ML methodology. In order to further demonstrate the applicability of this strategy for solving a complex fluid flow, we have adopted the FT-ML in our Marker-And-Cell (MAC) in-house code (MARTINS *et al.*, 2015; EVANS; FRANÇA; OISHI, 2019; OISHI; THOMPSON; MARTINS, 2019b) to investigate the outcomes in binary collisions of droplets.

The work that will be described in this chapter is published in the following article:

- França, H.L.; Oishi, C.M. A machine learning strategy for computing interface curvature in Front-Tracking methods. Journal of Computational Physics, v. 450, p. 110860, 2022.

5.1 Learning curvature and testing

In this section we describe a new machine learning scheme used to approximate curvature of 2D curves given by the Front-Tracking representation.

In the VOF-ML method (QI *et al.*, 2019), the curvature was approximated on a given grid cell (i, j). Analogously, in our Front-Tracking representation, the curvature will be computed on a marker particle p_i. The curvature on the marker p_i is approximated by a function with parameters F_i, each related to one of the $2N$ line segments around p_i, as illustrated in Figure 38a.

Following this idea, the discrete curvature κ_i is given by

$$h \cdot \kappa_i = C\left(\begin{bmatrix} F_{i-1} & F_{i-2} & \cdots & F_{i-N} \\ F_i & F_{i+1} & \cdots & F_{i+N-1} \end{bmatrix}\right), \tag{5.1}$$

where C is a selected function. Since the curvature has dimension one over length, we adopt a non dimensional curvature by multiplying by h, where h is the mean length of the $2N$ line segments used.

Each parameter F_i is defined as a set of two values (see Figure 38b):

- Value 1: the angle between the positive x axis and the outwards normal vector of the segment $[p_{i+1}, p_i]$.
- Value 2: same as value 1 for the oriented tangential vector.

Figure 38 illustrates the parameters used for a given point p_i using $N = 3$. Note that the function C in (5.1) is actually a function of $4N$ scalar parameters, since each F_i has two elements.

Figure 38 – Description of the parameters F_i used to approximate the curvature at the point p_i.

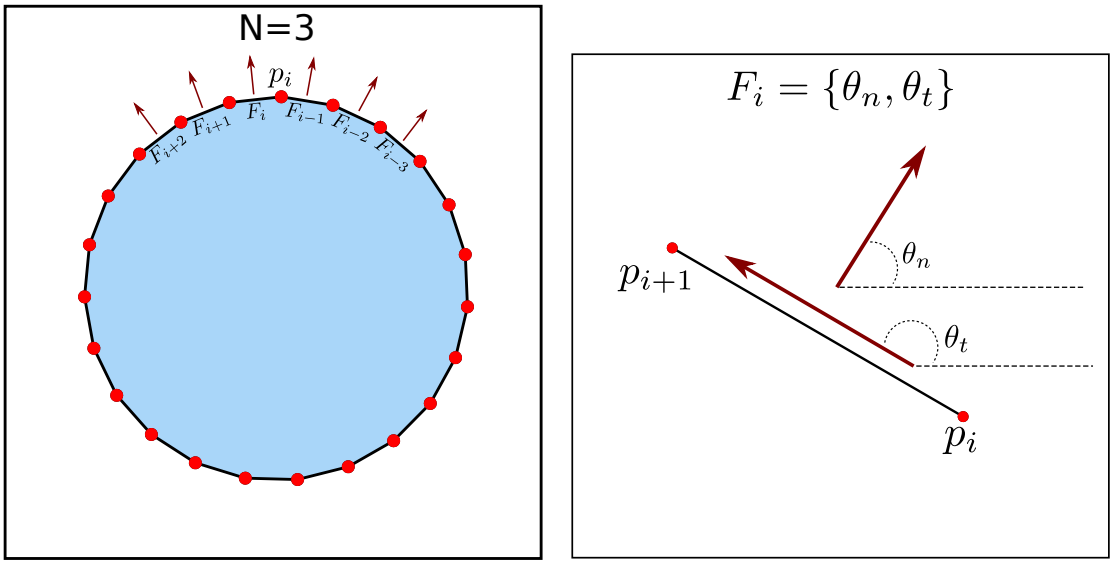

(a) Normal vectors associated with the point p_i

(b) Components of one parameter F_i, that is, angle of the normal and tangential vectors for the line segment $\overline{p_i p_{i+1}}$

Source: Elaborated by the author.

In the current work, the function C will be represented by a neural network with 4N scalar inputs and one output, as shown in Figure 39.

To train this network, we require a dataset with entries associated to curves with known curvature (see (QI *et al.*, 2019)). Different types of curves with analytical expressions for the curvature could be used to generate this dataset. The process to generate the dataset can be summarized as follows:

1. We generate 65 circles with radii varying from 0.00225 to 0.475. An exponential function is used to sample points in this interval, such that we have more circles with smaller radii

Figure 39 – Neural network used to describe the function C.

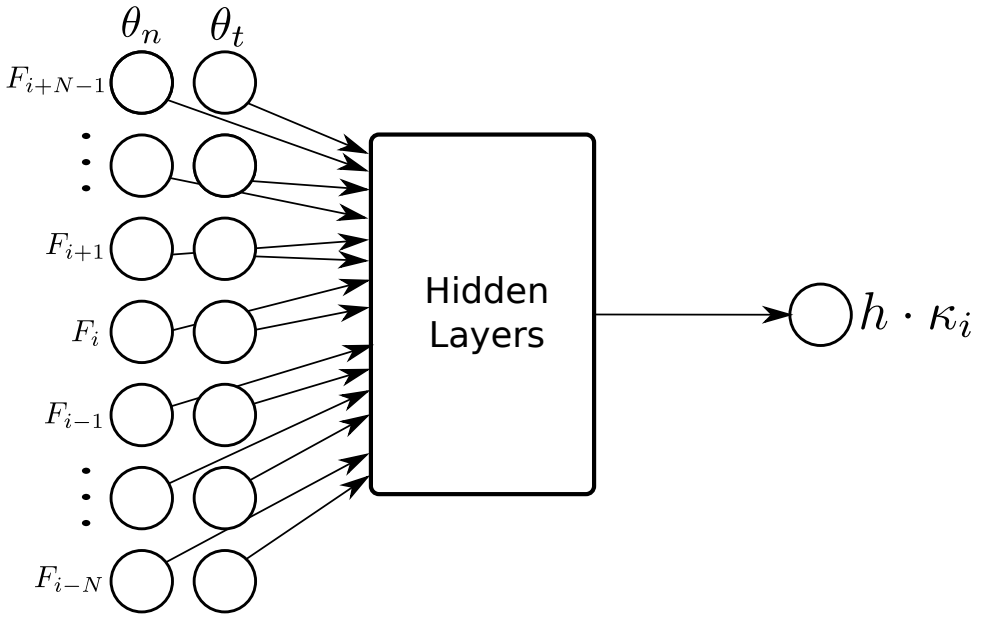

Source: Elaborated by the author.

(closer to 0.00225). The curvature of each circle is trivially given by $\kappa = \frac{1}{R}$, where R is the circle radius.

2. All circles are discretized using line segments with the same constant size h, which is a chosen parameter (discussed later). For $h = 0.0004$, the smallest circle will have 35 segments, for example. The marker particles for these segments are initially created in counter-clockwise order.

3. We iterate over each marker particle of each circle and, for each marker, two entries will be generated in the dataset:

   a) one entry is created with normals pointing outside of the circle and assuming positive curvature $h \cdot \frac{1}{R}$, as illustrated in Figure 40 (left);

   b) the second entry is created with normals pointing into the circle and assuming negative curvature $-h \cdot \frac{1}{R}$, as illustrated in Figure 40 (right).

4. The three steps above are repeated but, in the second step, the markers are generated in clockwise order.

Executing the steps above we obtain a dataset with thousands of entries. The exact number of entries depends on the value of h chosen.

From now on we will use a neural network with the following structure and training parameters:

- Number of hidden layers: 3 layers with 200 neurons each;

Figure 40 – Dataset generation for the Front-Tracking method: (Left) normals pointing outside of the circle and (Right) normals pointing into the circle in which negative curvature is assumed.

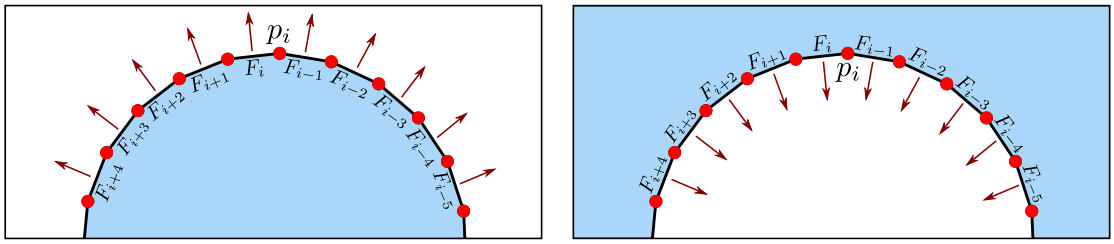

Source: Elaborated by the author.

- Activation function: reLU for hidden layers and linear for output layer;
- Loss function: mean squared error;
- Optimization algorithm: gradient descent with learning rate 0.01;
- Number of training epochs: 3000.

The training of this network was performed in Python via the Keras-Tensorflow module. The total dataset is split into a training set (80%) and a test set (20%). We did not encounter any significant issues regarding overfitting during our tests, so we chose to simply use a fixed number of epochs instead of using a validation set to measure convergence. After training, we employ the test dataset to evaluate how well the model is predicting curvatures. We note that our model and training set are defined by two hyperparameters: the number of segments around a marker (N) and the length of segments used in the training circles (h). Notice that there is a connection between these parameters since both N and h affect the total length of segments around a marker point p_i. We tested different values for both parameters and we show here results for $N = \{3,5,7\}$ and $h = \{0.0004, 0.0001\}$. These results are shown in Figure 41 as a scatter plot of predicted values versus exact values. If the fit were perfect, all points would lie on the identity line. According to Figure 4, we can observe better results for $h = 0.0004$ and smaller values of N. It makes sense especially for the smaller circles, in which too many segments would already take a big portion of their perimeter. From a qualitative point-of-view, according to Figures 41(b) and (e), we can also see an inaccurate fitting for the tuples $(N,h) = (3, 0.0001)$ and $(N,h) = (7,\ 0.0004)$ respectively. In order to further investigate the accuracy of the scheme, we have quantified in Table 2 the relative mean squared error for the same points plotted in Figure 41. Based on the results described in Table 2, we can note that most combinations give reasonably good results with similar order of magnitude, with the exception of $(N,h) = (3, 0.0001)$ and $(N,h) = (7,\ 0.0004)$.

We can now compute the curvature of other curves using the network that was previously trained only with data from circles. Following the test performed in (QI *et al.*, 2019), we have

Figure 41 – Scatter plots of the exact curvature versus the machine learning predicted curvature for each entry in the test dataset (generated from circles). Three values of N and two values of h are used to compare results. In this figure, the curvature values on the axis scaling are given by $\kappa = \pm 1/R$, with R varying from 0.00225 to 0.475.

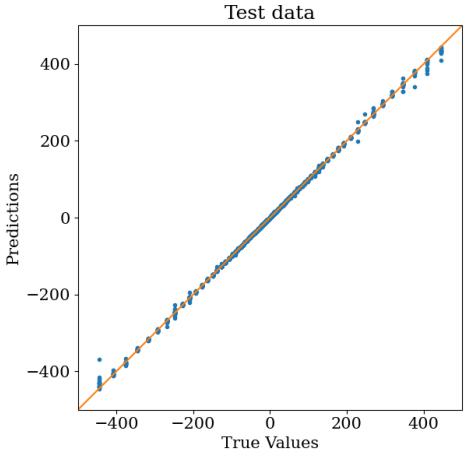

(a) $N = 3$ and $h = 0.0004$.

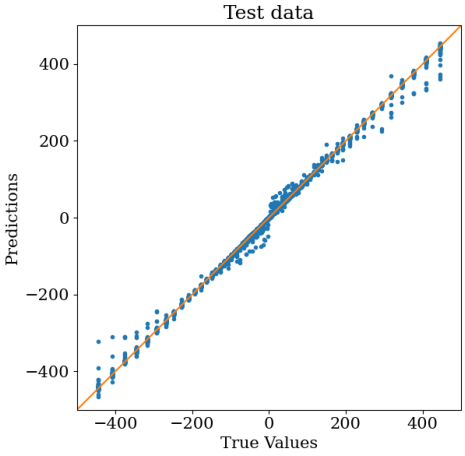

(b) $N = 3$ and $h = 0.0001$.

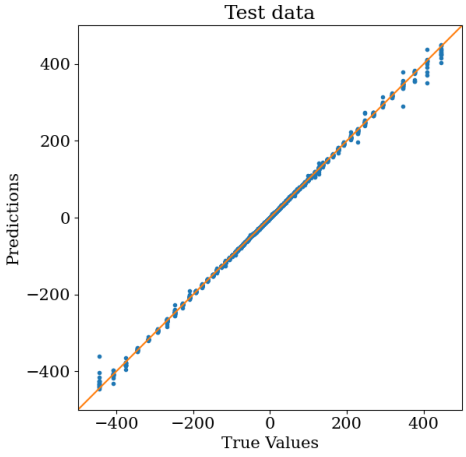

(c) $N = 5$ and $h = 0.0004$.

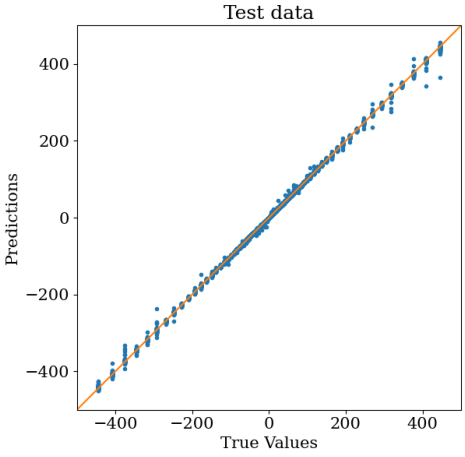

(d) $N = 5$ and $h = 0.0001$.

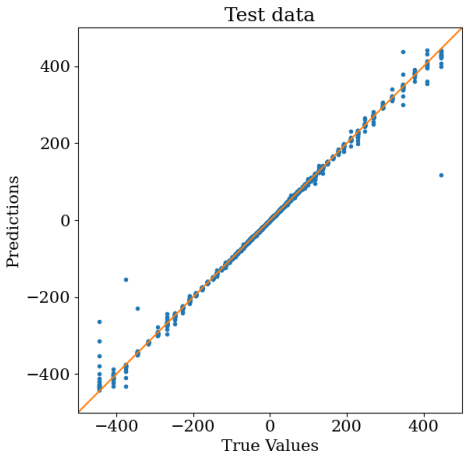

(e) $N = 7$ and $h = 0.0004$.

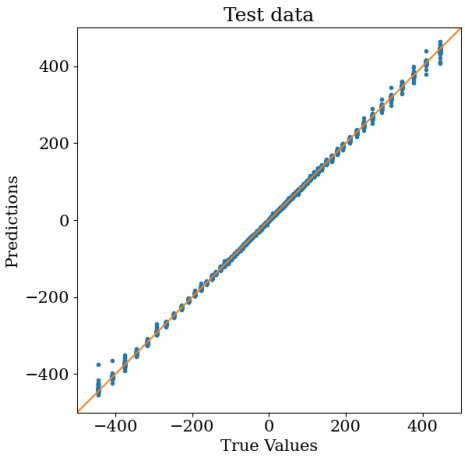

(f) $N = 7$ and $h = 0.0001$.

Source: Elaborated by the author.

Table 2 – Mean squared error in the test dataset generated with circles.

	$h = 0.0004$	$h = 0.0001$
$N = 3$	5.03E-04	9.00E-04
$N = 5$	6.41E-04	2.64E-04
$N = 7$	4.30E-03	2.41E-04

Source: Elaborated by the author.

computed the curvature of a sine wave. The wave was discretized on $x \in [-\pi, \pi]$ by 200 line segments, which gives us $h \approx 0.038$. Note that h is not required to be the exact same as the one used in training, since the output curvature was nondimensionalized by h. However, the discretization should be fine enough in order to obtain reasonable results in steep curves. We assume that the normal vectors are pointed upwards from the wave.

In Figure 42 we show the results obtained by using the model created and trained with $(N, h) = (3,\ 0.0004)$. On the left we plot the analytical and numerical curvatures computed over the x interval, and while slightly worse predictions are seen at the curvature peaks, generally good agreement is observed. On the right, we present the same results as a scatter plot of exact versus numerical curvatures for each point in the sine wave. According to the results described in Figure 5, we can see a good agreement between the analytical curvature and the predicted one.

Figure 42 – Results for the sine wave function. Left: plots of the exact and analytical curvature for $x \in [-\pi, \pi]$. Right: Scatter plot of the exact versus machine learning curvature according to the limits of sine wave curvature, e.g. $[-1, 1]$.

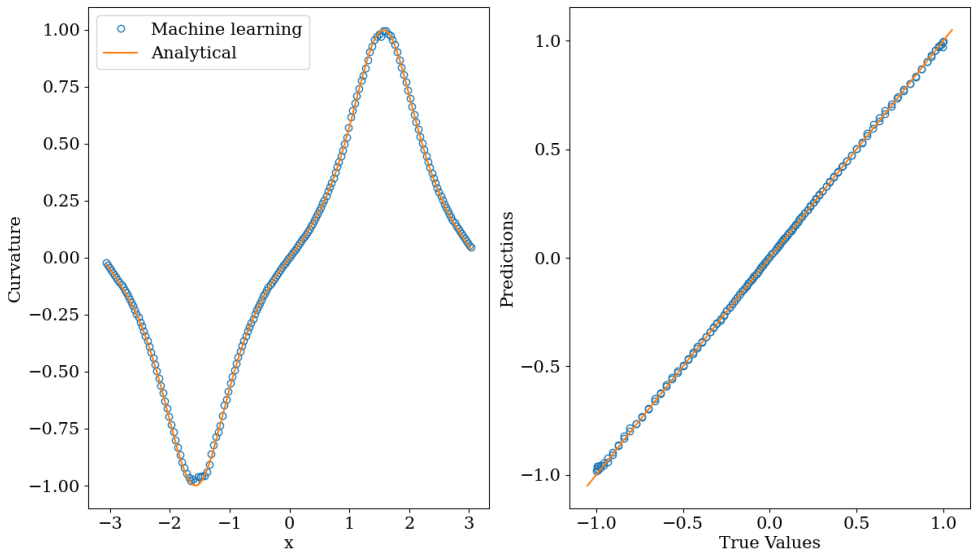

Source: Elaborated by the author.

In Table 3 we present the relative mean squared error for the sine wave curvature using the same variation of model and training parameters as before. While all variations produce reasonably good results, we note that the lowest error is obtained for $N = 3$ and $h = 0.0004$. For

all results shown in the following section, we will assume this combination of parameters.

Table 3 – Mean squared error in the test dataset generated for a sine function.

	$h = 0.0004$	$h = 0.0001$
$N = 3$	2.07E-04	2.50E-03
$N = 5$	6.27E-04	6.05E-04
$N = 7$	1.39E-03	1.70E-03

Source: Elaborated by the author.

5.2 Application of the scheme for solving a complex free surface flow

Our end goal with this formulation was to use the computed curvature to simulate fluid flows under the effects of surface tension. To test how the machine learning curvature works in these simulations, we decided to incorporate the trained network in our own in-house solver for free surface flows. After the network training is performed using the Python modules, all the network weights are exported into a simple text file, which is loaded into our solver (implemented in language C). The weights can then be easily used to re-evalute the network on our flow interfaces.

The nondimensional Navier-Stokes equations for a Newtonian fluid are given in chapter 2 by equations (2.8)-(2.10). We use a single-phase formulation, in which the free surface boundary conditions applied at the fluid interface are given by equations (2.38) and (2.39).

Equations (2.8) are solved numerically through a finite differences scheme based on the MAC formulation (MARTINS *et al.*, 2015; OISHI; THOMPSON; MARTINS, 2019b). The time-stepping is also performed by a simple finite differences Euler scheme, and a projection method is used to decouple the velocity and pressure updates. Finally, the marker particles $\mathbf{x}$ are updated at each time step by solving the advection equation

$$\dot{\mathbf{x}} = \mathbf{u}. \tag{5.2}$$

The flow chosen here to test the machine learning algorithm is the binary droplet collision, studied in depth in chapter 4. In this flow, two droplets initialized with given velocities $\mathbf{u}_1$ and $\mathbf{u}_2$, respectively, are launched against each other resulting in different outcomes. An important parameter in this simulation, named impact parameter B, is defined as

$$B = \frac{2b}{D_1 + D_2}, \tag{5.3}$$

where D_1 and D_2 are the drop diameters and b is the center-to-center relative distance.

In the literature there is a lot of interest in studying the post-collision outcomes of these droplets, which can be classified in three main regimes: coalescence, bouncing and separation.

We begin our tests comparing a classical FT and the FT-ML schemes for reproducing two experimental collisions reported in (PAN; LAW; ZHOU, 2008). According to the experiments, in one of these collisions the droplets are expected to coalesce and in the other to bounce. Figure 43a shows a side-by-side comparison between the numerical and experimental results for the coalescence case, while Figure 43b presents the same comparison for the bouncing simulation. In both cases we note the machine learning curvature is able to reproduce the experimental results with good qualitative agreement. In addition, in the figures for both numerical simulations we plot the interface obtained using the Machine Learning algorithm (blue) and using a traditional curve approximation scheme (red). We note that machine learning can capture the interface similarly to a traditional approach commonly adopted in FT schemes.

Figure 43 – Time sequence comparison between numerical and experimental droplet collisions in two cases: coalescence (a) and bouncing (b). In the numerical panels two interfaces are shown: interface obtained from the FT-ML curvature (blue) and from a traditional FT scheme (red). Panels from experimental results are reproduced from (PAN; LAW; ZHOU, 2008), with the permission of AIP Publishing.

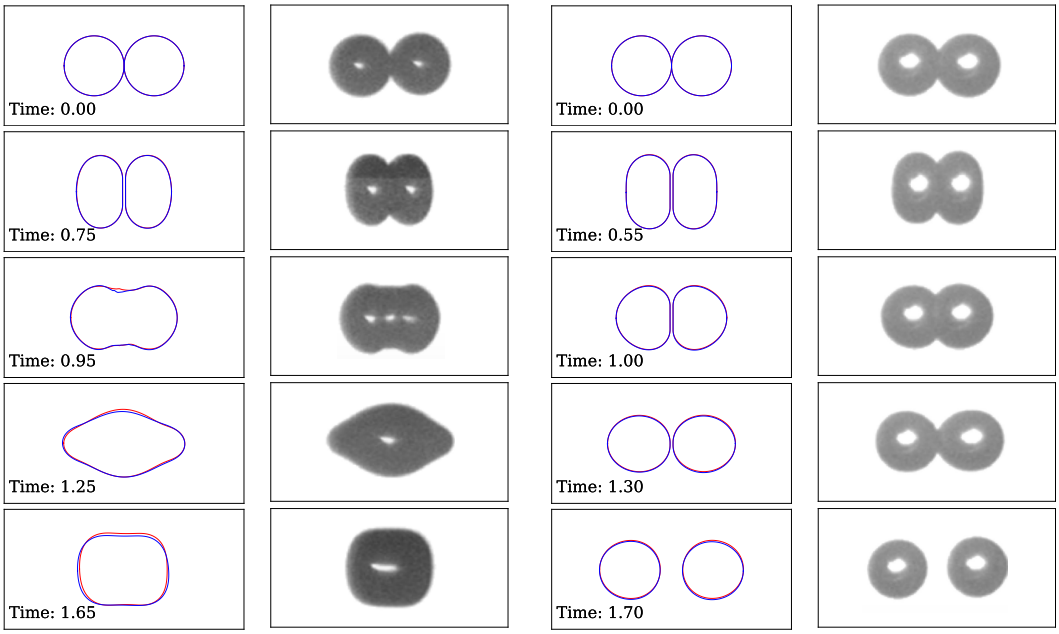

(a) Coalescence case: $We = 2.25$, $Re = 46.79$, $B = 0$.

(b) Bouncing case: $We = 2.27$, $Re = 59.32$, $B = 0$.

Source: Elaborated by the author.

In (AL-DIRAWI; BAYLY, 2019), a regime map is created indicating which outcome happens for different flow parameters, particularly B and We. In order to show our machine learning strategy works for a range of simulation parameters, we reproduced part of one of the maps shown in (AL-DIRAWI; BAYLY, 2019). Table 4 contains the parameters used in these simulations.

Table 4 – Fluid and simulation parameters used in the binary droplet collision simulations. These parameters correspond to the 4% HPMC fluid experiments performed in (AL-DIRAWI; BAYLY, 2019).

Nondimensional parameter	Value
Reynolds (Re)	{50.48, 87.45, 112.89, 151.46}
Weber (We)	{10, 30, 50, 70}
Impact parameter (B)	0, 0.2, 0.5, 0.8

Source: Elaborated by the author.

Figure 44 shows a comparison between the experimental map (taken from (AL-DIRAWI; BAYLY, 2019)) and the numerical map obtained using the machine learning curvature in our solver. We note that the solver is able to correctly capture the expected experimental results. In Figure 45, we depict selected frames for three different numerical simulations illustrating the possible outcomes: coalescence, separation and bouncing. It is worth to note that the topological changes that merge the droplets together do not happen naturally in an FT representation and need to be enforced. This enforcement was done at a certain simulation time prescribed at the beginning of the simulation, following the strategy proposed in (NOBARI; JAN; TRYGGVASON, 1996).

Figure 44 – Experimental (a) and numerical (b) regime maps for the Newtonian binary droplet collision.

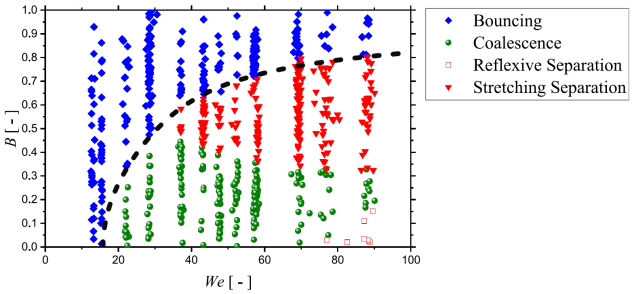

(a) Experimental map reproduced from (AL-DIRAWI; BAYLY, 2019), with the permission of AIP Publishing.

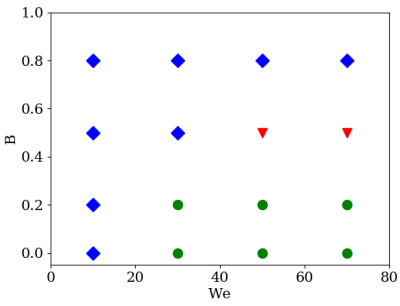

(b) Numerical map obtained from our solver.

Source: Elaborated by the author.

5.3 Conclusions

In this work we have shown that it is possible to use machine learning to compute the curvature of Front-Tracking interfaces. Using a very simple model and training strategy based only on circles, we were already capable of creating a function that can even be used to predict curvatures of complex interfaces arising from fluid simulations driven by surface tension. Finally, we highlight the importance of performing the present formulation by training the network with different elementary shapes. In addition, as a future work, we intend to conduct further studies on changing the network structure and including new investigations concerning data preprocessing mechanisms.

Figure 45 – Time sequence of three different simulations illustrating the possible outcomes: coalescence, bouncing and separation.

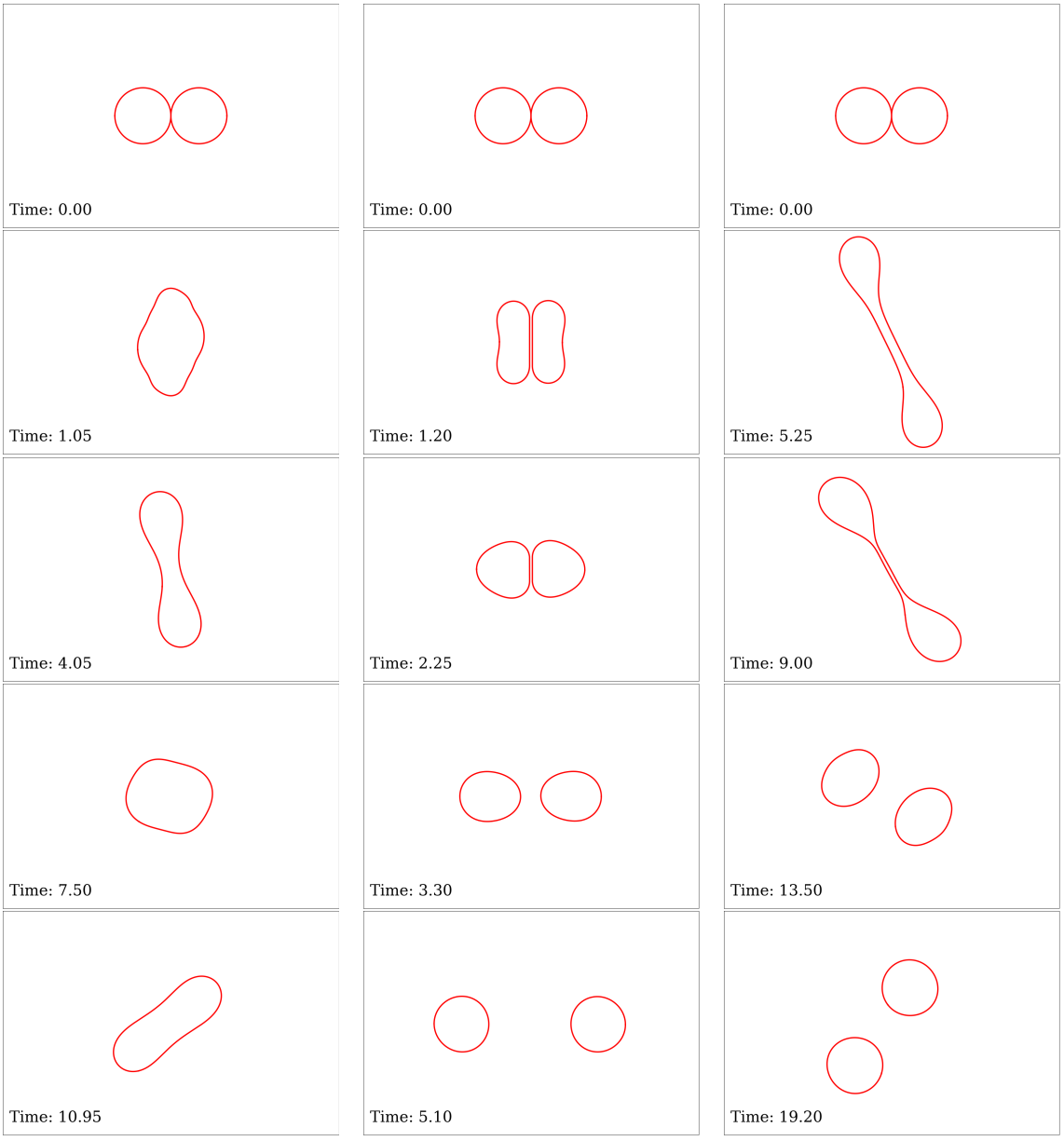

(a) Coalescence: $We = 30, B = 0.2$ (b) Bouncing: $We = 10, B = 0$ (c) Separation: $We = 50, B = 0.5$

Source: Elaborated by the author.

CHAPTER

6

ELASTOVISCOPLASTIC DROPLET SPREADING

6.1 Introduction

Understanding the behaviour of complex fluids is important in many fields of science and engineering, including chemical engineering, materials science, and biophysics. Mathematical models can be used to describe the rheology of complex fluids, and computer simulations can be implemented to study their properties and behaviour under different conditions. One class of these type of fluids are the elastoviscoplastic (EVP) materials which can exhibit both elastic and plastic properties, as well as viscous behaviour over time. In addition, these materials include time-dependent viscous behaviour that are commonly found in a variety of applications.

Some recent works have described the construction of mathematical models that are being incorporated in computational frameworks for describing the complex behaviour of EVP materials both in shear and elongational flows. For instance, Saramito (SARAMITO, 2007) revisited important contributions in the literature that proposed constitutive equations assuming the effect of the stress, strain, and/or strain rate of the material. Moreover, the works of Saramito (SARAMITO, 2007; SARAMITO, 2009) included descriptions of new EVP constitutive equations which combine classical viscoplastic models (Bingham and Herschel-Bulkley) with viscoelastic models (Oldroyd-B or PTT). Adopting a different perspective, de Souza Mendes (MENDES, 2011) used a generalized viscoelastic model where material properties are functions of the strain rate in order to incorporate the yielding behaviour of the material and also thixotropy effects. A thorough comparison of different EVP models is performed by Fraggedakis et al. (FRAGGEDAKIS; DIMAKOPOULOS; TSAMOPOULOS, 2016), where the authors comment on mathematical, physical and numerical properties of the models.

Since EVP models can be used in a variety of applications, the development of efficient computational frameworks is an essential step to solve complex flows of these fluids. In particular,

the combination of EVP models and moving interface problems includes additional complexity on the system and can depend on a variety of factors, such as the surface tension, elasticity and plasticity effects varying between phases. In this work, our main goal is to better understand the role of these material functions on the solution of the spreading of an EVP droplet.

The spreading of droplets is an important problem in fluid mechanics. Applications in which this problem is relevant include spray coating, inkjet printing and additive manufacturing (BARNES, 1999; DERBY, 2010; THOMPSON *et al.*, 2014; MACKAY, 2018). In cases such as 3D printing, it is common for droplets or filaments to be deposited over an already-existing layer of the same fluid, evidencing the importance of studying the dynamics of the spreading process for the design of such systems.

The spreading of Newtonian droplets over a fluid layer has been previously studied, see (BERGEMANN; JUEL; HEIL, 2018; JALAAL; SEYFERT; SNOEIJER, 2019) for example. While Newtonian droplets spread indefinitely until a completely flat film is obtained, viscoplastic droplets stop flowing at a non-flat final shape. This has been shown previously in (ROUSSEL; COUSSOT, 2005; BALMFORTH *et al.*, 2007; GERMAN; BERTOLA, 2009; JALAAL; BALMFORTH; STOEBER, 2015; LIU; MEI, 1989; CHEN; BERTOLA, 2017; LIU; BALMFORTH; HORMOZI, 2018). It has also been shown that elasticity can have an important role in droplet spreading problems. Luu and Forterre (LUU; FORTERRE, 2009) study the impact of droplets on rigid surfaces and notice significant changes between droplets of clay and Carbopol, with the latter presenting an intense recoil after spreading. This recoil is attributed to the elasticity in the material, which shows how elastic effects should be taken into account for droplet dynamics.

Computational studies involving EVP materials have also been performed in the past for other problems. Cheddadi et al. (CHEDDADI *et al.*, 2011) numerically solved the flow around a cylinder for an EVP material. They show that yield strain is the main nondimensional parameter that characterises the flow and that elasticity also has an important effect, which explain why previous experiments showed that stress does not depend simply on the shear rate. Nassar et al. (NASSAR; MENDES; NACCACHE, 2011) used an EVP model to simulate contraction-expansion flow. By performing a parametric study, they observe that elasticity significantly changes the shape and position of the resulting yield surface.

When it comes to interfacial problems involving droplets and capillary effects, numerical studies can also be found in the EVP literature. Oishi, Thompson and Martins have successfully used a numerical model that includes thixotropy into an EVP material. In (OISHI; MARTINS; THOMPSON, 2017), the authors solve the problem of a material being subject to gravity on an inclined plane. They are able to observe elastic behaviour and also to capture the so-called avalanche effect where a decrease in viscosity (triggered by a stress field) induces a motion that successfully creates another decrease in viscosity. In (OISHI; THOMPSON; MARTINS, 2019a), Oishi et al have also included the effects of surface tension to study how EVP droplets impact on a solid surface. They observe elastic effects can promote droplet spreading, while surface tension

acts against it. Izbassarov and Tamissola (IZBASSAROV; TAMMISOLA, 2020) investigated how an EVP droplet deforms inside a Newtonian medium under simple shear. They observe that the droplet deformation can present a non-monotonic behaviour as elasticity is changed. Moreover, in the limit of high yield-stress, elasticity can increase the droplet deformation significantly.

Jalaal et al. (JALAAL; STOEBER; BALMFORTH, 2021) developed an extensive experimental, theoretical and numerical study of a droplet spreading over a thin-film. The authors conduct experiments using droplets of Carbopol, which they model as a purely viscoplastic fluid. Good agreement is obtained between numerical simulations and theory, while experimental results show some discrepancy. Our goal in this work is to extend this numerical study by considering a rheology model that also includes elasticity.

In the present work, our main goal is to extend the numerical analysis peformed by Jalaal et al (JALAAL; STOEBER; BALMFORTH, 2021) to consider not only viscoplastic rheology, but also the addition of elasticity. By using Saramito's EVP model (SARAMITO, 2007), a parametric study will be carried over in order to understand how the addition of elasticity can affect the transient spreading dynamics and also the final shapes of elastoviscoplastic droplets.

6.2 Problem description: capillary spreading of a droplet

In this chapter we investigate the problem of an elastoviscoplastic droplet spreading over a thin-film. As illustrated in Figure 46a, a droplet is initially placed over a film and allowed to spread due to capillary and gravitational forces. Viscous forces oppose this spreading by slowing it down, and yield-stress is capable of stopping it completely as shown previously in (JALAAL; STOEBER; BALMFORTH, 2021). The role of elasticity in this process is less clear, and a numerical framework will be implemented in order to understand the behaviour of elastic droplets. The rheology of the EVP material will be modelled by the Saramito model, which generalizes both the Bingham viscoplastic and the Oldroyd-B viscoelastic models. Figure 46b shows a mechanical analog of this model.

Figure 46 – a) Sketch of the geometry of a spreading elastoviscoplastic droplet. We assume the droplet to be axisymmetric around the z-axis. b) Mechanical analog of Saramito's elastoviscoplastic model.

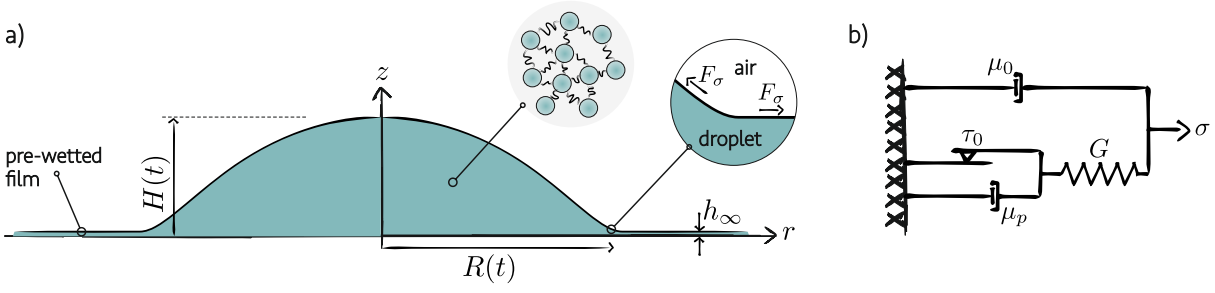

Source: Elaborated by the co-supervisor Maziyar Jalaal.

6.3 Governing equations

In this chapter we will use a different numerical platform to obtain our results as the one used in the previous chapters. The software Basilisk will be used to model the flow of an elastoviscoplastic fluid.

In Basilisk, the governing equations for the isothermal incompressible bi-phase flow, are the continuity and momentum conservation given by

$$\nabla \cdot \mathbf{u} = 0, \tag{6.1}$$

$$\rho \left(\frac{\partial \mathbf{u}}{\partial t} + \nabla \cdot (\mathbf{u}\mathbf{u}) \right) = -\nabla p + \nabla \cdot \boldsymbol{\tau} + \mathbf{f}_g + \mathbf{f}_s, \tag{6.2}$$

where $\mathbf{u}$ and p are the velocity and pressure fields. The gravitational force is defined as $\mathbf{f}_g = \rho \mathbf{g}$ where ρ is the fluid mass density. The surface tension force is defined as in (TRYGGVASON; SCARDOVELLI; ZALESKI, 2011) by $\mathbf{f}_s = \sigma \kappa \delta_s \mathbf{n}$ where κ is the curvature of the droplet-air interface, σ the constant surface tension coefficient, $\mathbf{n}$ is the interface normal, and δ_s is the Dirac delta function centered on the interface.

To represent the elastoviscoplastic rheology, we chose the model proposed by Saramito (SARAMITO, 2007), which is a generalization of the Oldroyd-B viscoelastic and the Bingham viscoplastic models. In Saramito's model, the extra-stress tensor $\boldsymbol{\tau}$ is composed of solvent $\boldsymbol{\tau}^s$ and polymeric $\boldsymbol{\tau}^p$ contributions such that

$$\boldsymbol{\tau} = \boldsymbol{\tau}^s + \boldsymbol{\tau}^p. \tag{6.3}$$

The solvent stress contribution presents a Newtonian behaviour given by

$$\boldsymbol{\tau}^s = 2\eta_s \mathbf{D}, \tag{6.4}$$

where η_s is the solvent viscosity and $\mathbf{D} = \frac{1}{2}\left[\nabla \mathbf{u} + (\nabla \mathbf{u})^T\right]$ is the strain rate tensor. For non-Newtonian fluids, the term $\boldsymbol{\tau}^p$ represents the polymeric contribution in the flow which, in this case, is modelled by a hyperbolic constitutive equation given by

$$\lambda_p \overset{\triangledown}{\boldsymbol{\tau}}^p + \max\left(0, 1 - \frac{\tau_0}{||\boldsymbol{\tau}^p||}\right) \boldsymbol{\tau}^p = 2\eta_p \mathbf{D}, \tag{6.5}$$

where λ_p is the relaxation time, η_p is the polymeric viscosity, $||\cdot||$ denotes the matrix norm defined as $||\boldsymbol{\tau}|| = \sqrt{\mathrm{tr}(\boldsymbol{\tau}^2)}$, and $\overset{\triangledown}{\boldsymbol{\tau}}^p$ is the upper-convected time derivative, given by

$$\overset{\triangledown}{\boldsymbol{\tau}}^p = \frac{\partial \boldsymbol{\tau}^p}{\partial t} + (\mathbf{u} \cdot \nabla)\, \boldsymbol{\tau}^p - (\nabla \mathbf{u})\boldsymbol{\tau}^p - \boldsymbol{\tau}^p (\nabla \mathbf{u})^T. \tag{6.6}$$

A dimensionless version of these equations can be obtained by scaling the variables as follows

$$\mathbf{x} = L\bar{\mathbf{x}}, \quad t = \frac{L}{U}\bar{t}, \quad \mathbf{u} = U\bar{\mathbf{u}}, \quad p = \frac{\eta_0 U}{L}\bar{p}, \quad \boldsymbol{\tau}^p = \frac{\eta_0 U}{L}\bar{\boldsymbol{\tau}}^p, \tag{6.7}$$

where $U = \sqrt{\frac{\sigma}{\rho_d L}}$ is the characteristic velocity (ρ_d is the droplet density), $\eta_0 = \eta_s + \eta_p$ is the total viscosity of the droplet, and the length scale is $L = [3V/(4\pi)]^{1/3}$ with V being the volume of the droplet (L can be seen as the radius of a corresponding spherical droplet with same volume V).

Removing, for convenience, the bars in (6.7), the dimensionless governing equations for the droplet phase is given by

$$\nabla \cdot \mathbf{u} = 0, \tag{6.8}$$

$$\frac{\partial \mathbf{u}}{\partial t} + \nabla \cdot (\mathbf{u}\mathbf{u}) = -\nabla p + \nabla \cdot (2\ \beta\ \mathrm{Oh}\ \mathbf{D}) + \nabla \cdot \boldsymbol{\tau}^p + \mathrm{Bo} \cdot \mathbf{g} + \kappa \delta_s \mathbf{n}, \tag{6.9}$$

$$\mathrm{Wi}\left(\frac{\partial \boldsymbol{\tau}^p}{\partial t} + (\mathbf{u}\cdot\nabla)\boldsymbol{\tau}^p - (\nabla \mathbf{u})\boldsymbol{\tau}^p - \boldsymbol{\tau}^p(\nabla \mathbf{u})^T\right) + \max\left(0, 1 - \frac{J}{||\boldsymbol{\tau}^p||}\right)\boldsymbol{\tau}^p = 2\ (1-\beta)\ \mathrm{Oh}\ \mathbf{D} \tag{6.10}$$

with the dimensionless groups: Ohnesorge number (Oh), Bond number (Bo), plastocapillary number (J), Weissenberg number (Wi), and viscosity ratio ($\beta \in (0,1]$) defined respectively as

$$\mathrm{Oh} = \frac{\eta_0}{\sqrt{\rho_d \sigma L}}, \quad \mathrm{Bo} = \frac{\rho_d g_0 L^2}{\sigma}, \quad J = \frac{\tau_0 L}{\sigma}, \quad \mathrm{Wi} = \lambda_p \sqrt{\frac{\sigma}{\rho_d L^3}}, \quad \beta = \frac{\eta_s}{\eta_0}. \tag{6.11}$$

We note that, now that we are using the multiphase formulation, we also have fluid motion in the air phase. Therefore, a set of equations similar to equations (6.8)-(6.9) is also solved in the air phase. Consequently, two other nondimensional parameters are also relevant in this problem: the density ratio between droplet and air (ρ_d/ρ_a) and viscosity ratio (η_0/η_a). Both of these ratios are kept constant with a value of 100.

Equations (6.8)-(6.10) have some limiting cases that are relevant to note, for instance:

- $J = 0$: in this case, we have a purely viscoelastic Oldroyd-B fluid.
- $\mathrm{Wi} = 0$: we have a purely viscoplastic Bingham fluid. Note that, substituting $\mathrm{Wi} = 0$, equation (6.10) simplifies to:

$$\max\left(0, 1 - \frac{J}{||\boldsymbol{\tau}^p||}\right)\boldsymbol{\tau}^p = 2\ (1-\beta)\ \mathrm{Oh}\ \mathbf{D}. \tag{6.12}$$

  Because the polymeric stress tensor $\boldsymbol{\tau}_p$ is colinear to the deformation rate tensor $\mathbf{D}$, we can write that $\frac{\boldsymbol{\tau}^p}{||\boldsymbol{\tau}^p||} = \frac{\mathbf{D}}{||\mathbf{D}||}$. With this, the yielded-case of equation (6.12) changes to

$$\boldsymbol{\tau}^p - J\frac{\mathbf{D}}{||\mathbf{D}||} = 2\ (1-\beta)\ \mathrm{Oh}\ \mathbf{D}, \tag{6.13}$$

  and, therefore,

$$\boldsymbol{\tau}^p = 2\left((1-\beta)\ \mathrm{Oh} + \frac{J}{2||\mathbf{D}||}\right)\mathbf{D}. \tag{6.14}$$

This confirms that, in the case of $\mathrm{Wi} = 0$, the EVP equations reduce to a Bingham generalized Newtonian model with extra-stress tensor given by

$$\boldsymbol{\tau} = \boldsymbol{\tau}_s + \boldsymbol{\tau}_p = 2\,\beta\,\mathrm{Oh}\,\mathbf{D} + 2\left((1-\beta)\,\mathrm{Oh} + \frac{J}{2||\mathbf{D}||}\right)\mathbf{D} = 2\left(\mathrm{Oh} + \frac{J}{2||\mathbf{D}||}\right)\mathbf{D}. \quad (6.15)$$

In practice, whenever our code receives the parameter $\mathrm{Wi} = 0$, we will completely ignore the EVP constitutive equation (2.10) and, instead, will simply solve a generalized Newtonian model with the apparent viscosity from equation (6.15) given by

$$\eta_{app} = \mathrm{Oh} + \frac{J}{2||\mathbf{D}||}. \quad (6.16)$$

In this case, equation (6.8) can be rewritten as:

$$\frac{\partial \mathbf{u}}{\partial t} + \nabla\cdot(\mathbf{u}\mathbf{u}) = -\nabla p + \nabla\cdot\left(2\left[\mathrm{Oh} + \frac{J}{2||\mathbf{D}||}\right]\mathbf{D}\right) + \mathrm{Bo}\cdot\mathbf{g} + \kappa\delta_s\mathbf{n} \quad (6.17)$$

- $J = 0$ and $\mathrm{Wi} = 0$: From equation (6.15) we see that, in this case, we have simply a Newtonian fluid with stress tensor

$$\boldsymbol{\tau} = 2\,\mathrm{Oh}\,\mathbf{D}. \quad (6.18)$$

This system of equations is closed with appropriate boundary conditions. At the solid wall under the droplet, we apply a no-slip condition, at the two boundaries distant from the droplet we apply an outflow condition and rotational symmetry is applied at the center of the droplet.

6.4 Numerical method

In this chapter we used the platform Basilisk C (POPINET; COLLABORATORS, 2013-2021) to solve the equations described in the previous section. A modification was done in their standard Oldroyd-B implementation in order to account for the yield-stress effects in Saramito's model. We note that Basilisk's Oldroyd-B implementation is based on the log-conformation stabilization approach, which allows us to run simulations at very high Weissenberg numbers (FATTAL; KUPFERMAN, 2004). An overview of the numerical procedure will be given in this section, but detailed descriptions of Basilisk can be viewed in (POPINET, 2015).

The simulation is setup by initializing a droplet according to the following nondimensional shape

$$h(r,0) = h_\infty + R_0 \max\left(0, 1-(r/R_0)^2\right), \qquad \text{with} \qquad R_0 = 1. \quad (6.19)$$

The droplet is placed in a square domain with dimensions $[0,5R_0]\times[0,5R_0]$ which is fully discretized with a non-uniform and adaptive quadtree grid. To accurately resolve the droplet

shape, we apply an increased refinement level near the droplet interface as shown in Figure 47. As the droplet spreads over time, the mesh is also adapted so that the refined region follows the interface.

The interface is represented implicitly by the Volume of Fluid (VOF) scheme (HIRT; NICHOLS, 1981), in which each mesh cell stores a value representing the fraction of droplet fluid inside it. Density and viscosity are locally determined based on the volume fraction $c(\mathbf{x},t)$ according to

$$\rho(c) = c\,\rho_d + (1-c)\rho_a, \tag{6.20}$$

$$\eta(c) = c\,\eta_d + (1-c)\eta_a. \tag{6.21}$$

where ρ and η represent the density and dynamic viscosity of a fluid, respectively. The subscripts d and a represent, respectively, the droplet and the air.

This volume fraction field c is then advected over time by solving the equation

$$\frac{\partial c}{\partial t} + \nabla\cdot(c\mathbf{u}) = 0. \tag{6.22}$$

The numerical code then solves the governing equations using a projection method and a multilevel Poisson solver. More details on the implementation of the Basilisk C solver can be seen in (POPINET, 2015).

6.4.1 Numerical regularization

As previously described, in the case of Wi = 0, our code automatically switches to a generalized Newtonian Bingham model. In this case, the apparent viscosity in equation (6.16) is actually replaced by the popular regularized Bingham-Papanastasiou viscosity (PAPANASTASIOU, 1987) given by

$$\eta_{app} = \mathrm{Oh} + \frac{J}{2||\mathbf{D}||}\left(1 - e^{-||\mathbf{D}||/\varepsilon_{vp}}\right), \tag{6.23}$$

where ε_{vp} is the regularization parameter. A thorough study on the effects of this regularization was performed by (FRIGAARD; NOUAR, 2005) and a short convergence test on this parameter will be provided in the next section.

When $\mathrm{Wi} \neq 0$, the full Saramito constitutive equations (2.10) are used. The software Basilisk already contains a well-tested implementation of the Oldroyd-B model for solving viscoelastic solvers given the parameters λ (relaxation time) and η_p (polymeric viscosity). To make use of this existing module, we re-wrote the Saramito constitutive equation (6.10) as

$$\frac{\mathrm{Wi}}{\alpha}\overset{\triangledown}{\boldsymbol{\tau}}^p + \boldsymbol{\tau}^p = 2\,\frac{(1-\beta)\,\mathrm{Oh}}{\alpha}\,\mathbf{D}, \qquad \text{where} \qquad \alpha = \max\left(\varepsilon_{evp}, 1 - \frac{J}{||\boldsymbol{\tau}^p||}\right), \tag{6.24}$$

and ε_{evp} is a small threshold parameter. We note that equation (6.24) has the same form as the traditional Oldroyd-B equations, but with non-constant relaxation time and polymeric viscosity coefficients. Therefore, we use the standard Oldroyd-B solver in Basilisk by dynamically setting these two coefficients according to the expressions in equation (6.24).

Figure 47 – Non-uniform grid generated for the spreading simulation. Cells are colored by their level of refinement. We note that this figure does not capture the entire domain, which continues both in the r and z directions.

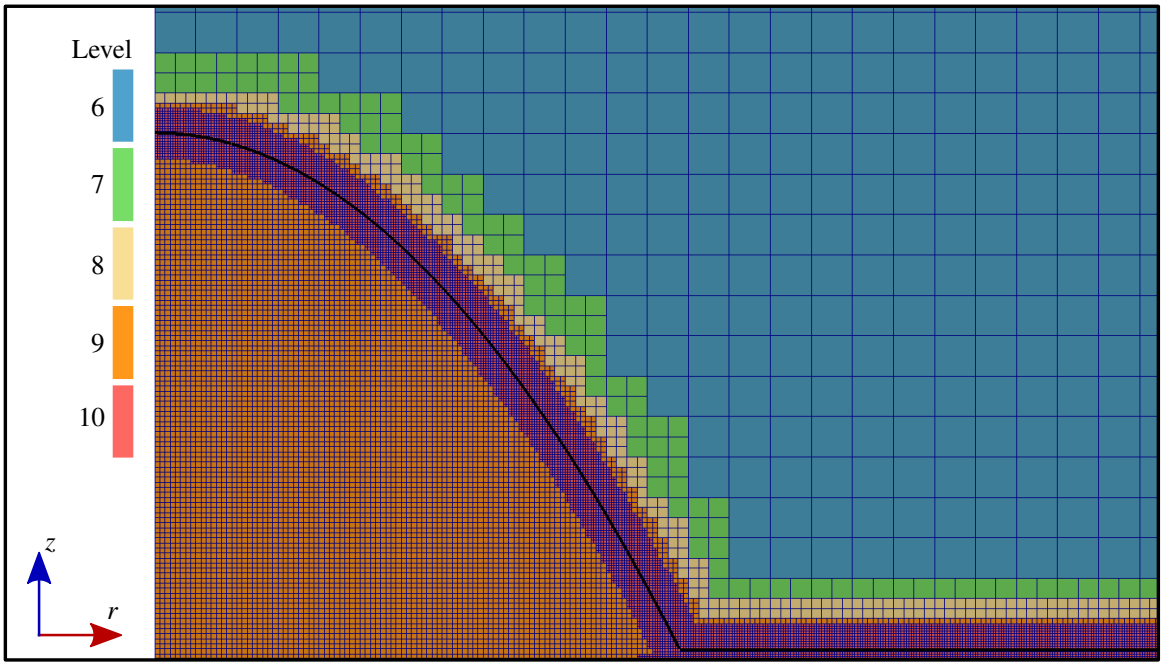

Source: Elaborated by the author.

6.5 Validation of the numerical methodology

6.5.1 Purely viscoplastic validation

We begin by validating the code in the purely viscoplastic case, that is, Wi = 0. As discussed in section 6.3, when Wi is zero we ignore the full Saramito constitutive equations for $\boldsymbol{\tau}^p$ and simply use a generalized Newtonian formulation with the apparent viscosity from equation (6.23).

Figure 48 shows a convergence test for the viscoplastic regularization parameter and for the mesh refinement. In all cases, the following parameters are fixed: $J = 0.18$, $Oh = 0.1$, $Wi = 0$, $Bo = 0$ and interface is captured at time $t = 10$. In Figure 48(a), we vary the value of the regularization parameter ε_{vp} with a fixed mesh level 10. We note that the solution has converged for values $\varepsilon_{vp} \leq 10^{-3}$. In Figure 48(b) the mesh refinement parameter is varied for a fixed $\varepsilon_{vp} = 10^{-3}$. We can see that the interface shape does not change significantly anymore for Level ≥ 10. With these results in mind, from now on all the viscoplastic simulations in this paper will be performed with $\varepsilon_{vp} = 10^{-3}$ and Level $= 10$.

Figure 48 – Convergence tests for the Bingham regularization parameter (left) and for the mesh refinement parameter (right). For the regularization tests, the mesh is fixed at Level = 10. For the mesh tests, the regularization is fixed at $\varepsilon_{vp} = 10^{-3}$.

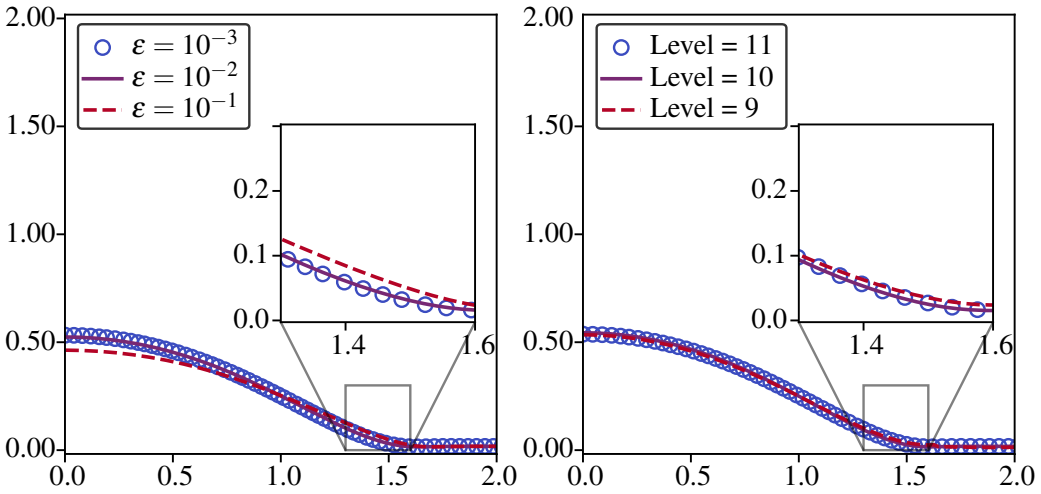

Source: Elaborated by the author.

6.5.2 Purely viscoelastic validation

We now perform a convergence test for the case of viscoelastic droplets ($J = 0$ and $Wi \neq 0$). In this situation, no viscoplastic regularization needs to be used, so we only check for mesh convergence. Figure 49 shows the radius and height of the droplet over time for different mesh levels with fixed Wi = 0.41. We note that little difference is observed with mesh levels above 9. For this reason, all the viscoelastic simulations performed in this work will use the mesh level 10.

6.5.3 Elastoviscoplastic validation

Figure 50 shows convergence tests for the EVP threshold parameter and for the mesh refinement parameter in a simulation with Wi = 0.816 and $J = 0.18$. We observe that ε_{evp} stops having an influence even at relatively large values. Regarding mesh convergence, we see that for refinement levels above 9, the results are already very similar. For all the following EVP simulations in this paper we will use the combination $\varepsilon_{evp} = 10^{-7}$ and Level = 10.

6.6 Results and discussion

6.6.1 Pure viscoplasticity

For viscoplastic materials, theoretical and experimental results for the droplet spreading have been previously presented in (JALAAL; STOEBER; BALMFORTH, 2021). We will also

Figure 49 – Numerical mesh convergence tests for purely viscoelastic simulations. Left: droplet radius over time for different mesh levels. Right: droplet height over time.

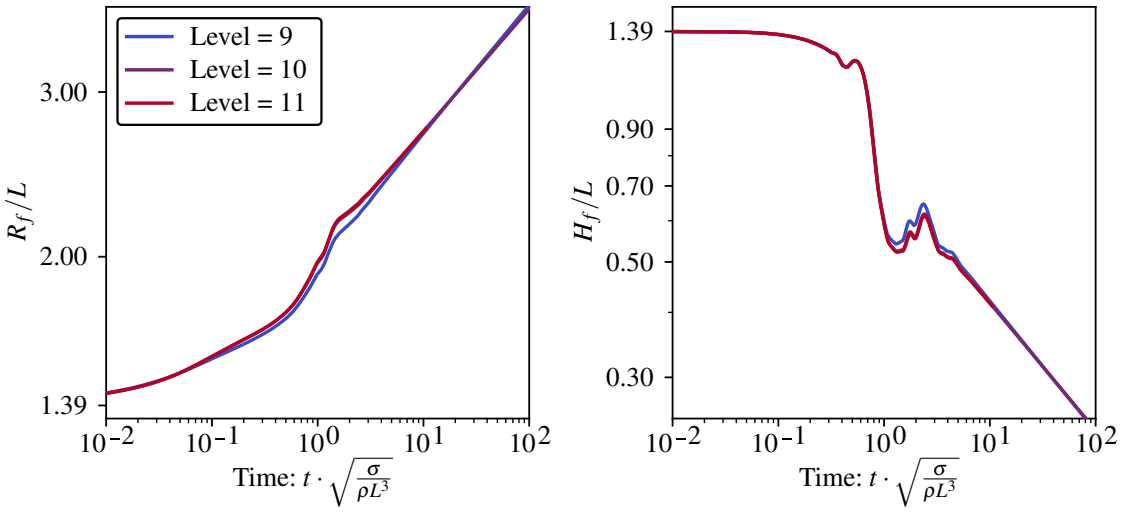

Source: Elaborated by the author.

Figure 50 – Convergence tests for the EVP regularization parameter (left) and for the mesh refinement parameter (right). In the regularization tests, we keep fixed the mesh level as 10 and in the mesh tests we fix the regularization $\varepsilon_{evp} = 10^{-7}$. All simulations are performed with Wi = 0.816 and $J = 0.18$.

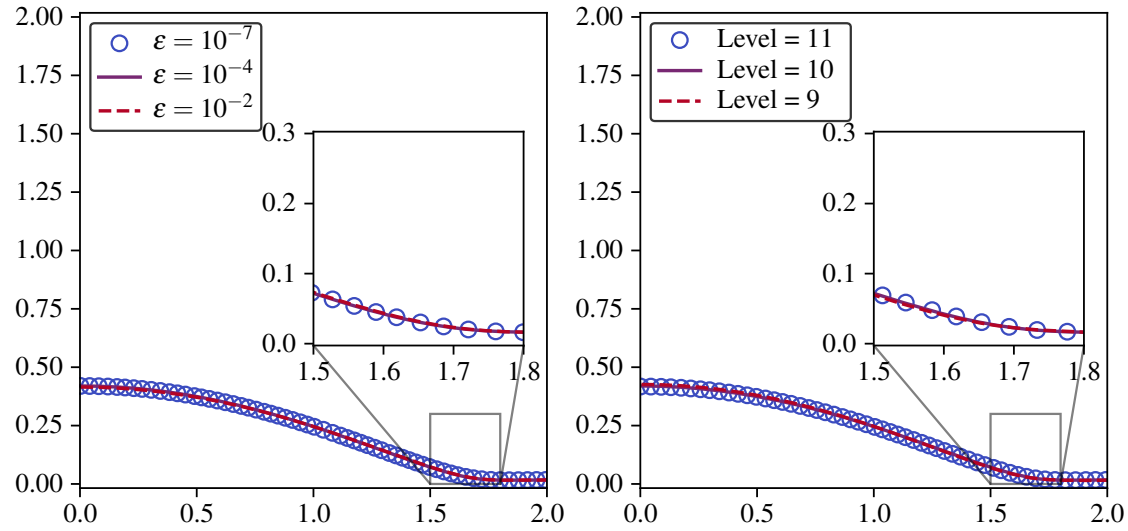

Source: Elaborated by the author.

validate our code by comparing their data with our simulation results. Unlike Newtonian droplets, it was found that droplets presenting yield-stress will eventually stop spreading at a final shape that is not flat. In (JALAAL; STOEBER; BALMFORTH, 2021) a theoretical scaling law was developed to relate the final shape of a droplet (its radius and height) as a function of the plastocappilary number J. To test our numerical results against this theory, we chose a stop

criteria for our simulations based on the kinetic energy of the droplet. The droplet shape is captured when the nondimensional kinetic energy E_k is smaller than 10^{-6}, where E_k is given by

$$E_k = \frac{1}{\sigma L^2} \int_V \frac{1}{2} \rho_d \, ||\mathbf{u}||^2 \, dV, \tag{6.25}$$

integrating over the entire droplet volume.

Figure 51 shows the final radius and height of our simulated droplets versus the plastocapillary number J. As expected, we see that the final radius decreases with higher J, while the final height increases. This happens because higher values of J mean higher influence of yield-stress, which makes the spreading stop closer to the initial shape. Another interesting observation is the fact that both quantities reach a plateau for high J. This happens because, after a certain J value, the droplets practically get stuck at whatever initial shape is created, since the capillary forces are not strong enough to overcome the yield-stress at all. Between the low yield-stress scaling law and the high yield-stress plateau regimes, we can see a transition region where the numerical results smoothly vary between regimes. In this region, the yield-stress is high enough so that the droplet never yields entirely, which makes the scaling law not work. At the same time, a portion of the droplet is still yielding, so it also does not get stuck in its initial shape either.

Figure 51 – Viscoplastic droplet final radius and height as a function of the plastocapillary number. The theoretical prediction is developed in (JALAAL; STOEBER; BALMFORTH, 2021). The gray line indicates the initial radius and height of the droplets.

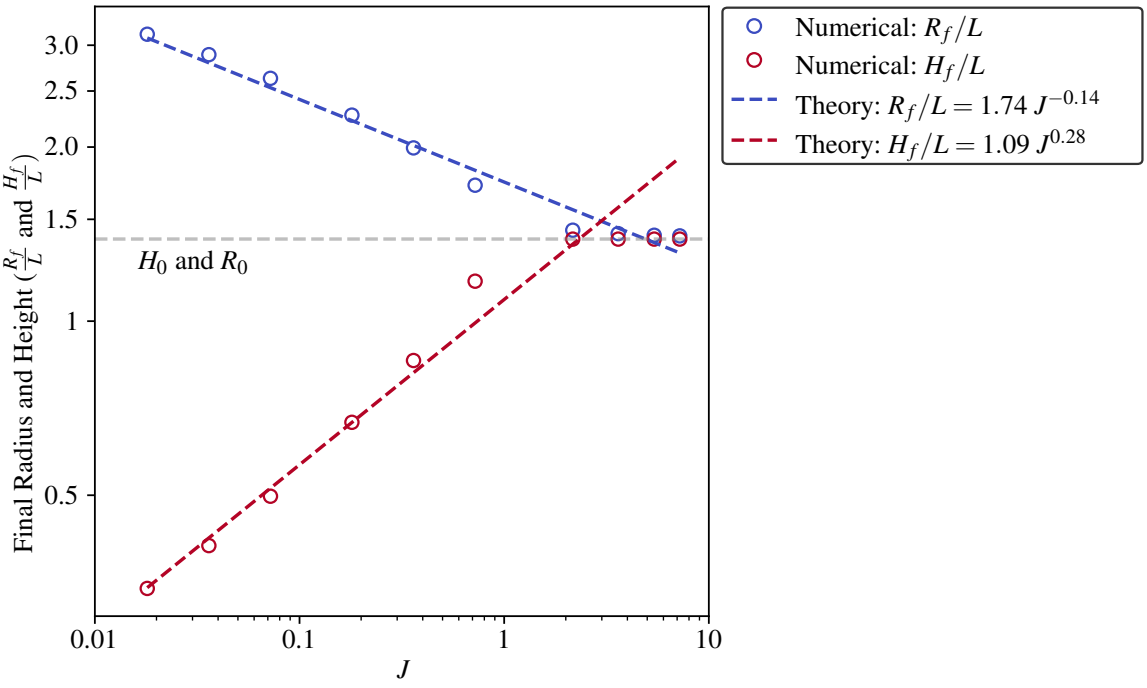

Source: Elaborated by the author.

6.6.2 Pure viscoelasticity

We continue our discussion by considering the case in which the material is viscoelastic, that is, $J = 0$. In this situation, the model reduces to an Oldroyd-B fluid. Figure 52 shows the droplet radius (top) and height (bottom) over time for different values of Wi. We note that, in the first moments, the droplet spreads considerably more as we increase Wi. This happens because the parameter Wi is related to the relaxation time of the polymers. When we increase the relaxation time (or Wi), the stresses take a longer time to develop when a shear rate is applied, consequently the droplet spreads more since the internal stress is smaller during this transient period. As a consequence of this, an interesting result it that the curves converge as $\mathrm{Wi} \to \infty$. In this limit, the polymeric stress tensor does not have enough time to develop at all in this timescale of the simulation and we actually recover a Newtonian droplet that only exhibits the solvent stress, i.e., we have a Newtonian simulation with Ohnesorge number $Oh_\infty = \beta$ Oh. We also observe that, for the Newtonian case ($Wi = 0$), the spreading eventually follows the rate predicted by Tanner's law, i.e, $R_f \propto t^{0.1}$ and $H_f \propto t^{-0.2}$.

Figure 52 – Spreading radius (top) and height (bottom) over time for different values of the Weissenberg number.

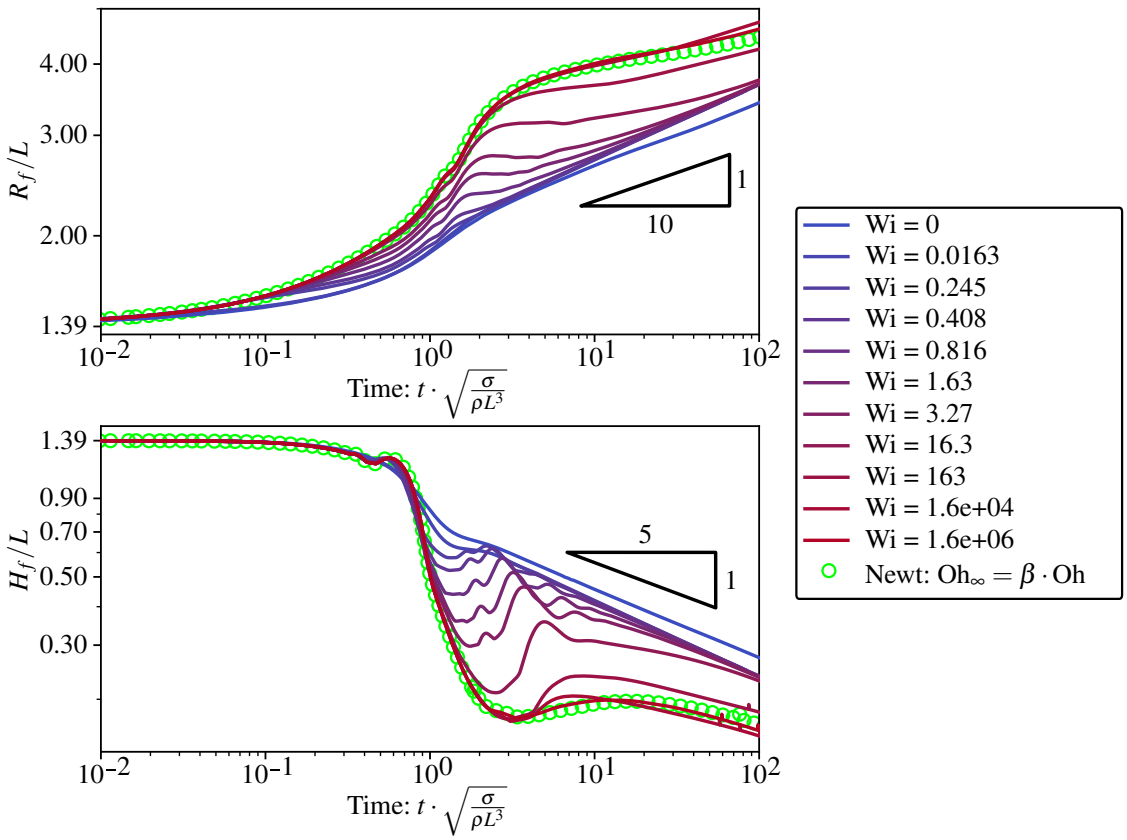

Source: Elaborated by the author.

The explanation given above for the increased spreading with Wi is based on the Oldroyd-B behaviour in a shear flow. To verify that the spreading is dominated by a shear deformation,

we can visualize the flow type parameter inside the droplet. This parameter is defined as

$$\xi = \frac{|\mathbf{D}| - |\mathbf{\Omega}|}{|\mathbf{D}| + |\mathbf{\Omega}|}, \tag{6.26}$$

where $\mathbf{D}$ and $\mathbf{\Omega}$ are the deformation rate and vorticity tensors, respectively,

$$\mathbf{D} = \frac{1}{2}\left[\nabla\mathbf{u} + (\nabla\mathbf{u})^T\right] \qquad \text{and} \qquad \mathbf{\Omega} = \frac{1}{2}\left[\nabla\mathbf{u} - (\nabla\mathbf{u})^T\right]. \tag{6.27}$$

The flow type parameter can vary in the range $\xi \in [-1, 1]$, where $\xi = 1$ represents a purely extensional flow, $\xi = 0$ shear flow and $\xi = -1$ indicates solid-like rotation. Figure 53 shows the value of ξ inside a viscoelastic droplet with $Wi = 0.245$ for different time frames. We can see a separation in two important regions: close to the symmetry axis the flow is predominantly extensional (red color), as one would expect, and close to the wall we get a shear region (gray). Since the spreading dynamics originate near the wall, this confirms that this is a mostly shear-dominated flow.

Figure 53 – Anatomy of the flow inside a viscoelastic droplet with Wi = 0.245 at different time stamps. Regions of $\xi = 0$ indicate purely shear flow, $\xi = 1$ extensional flow, and $\xi = -1$ solid-like rotation.

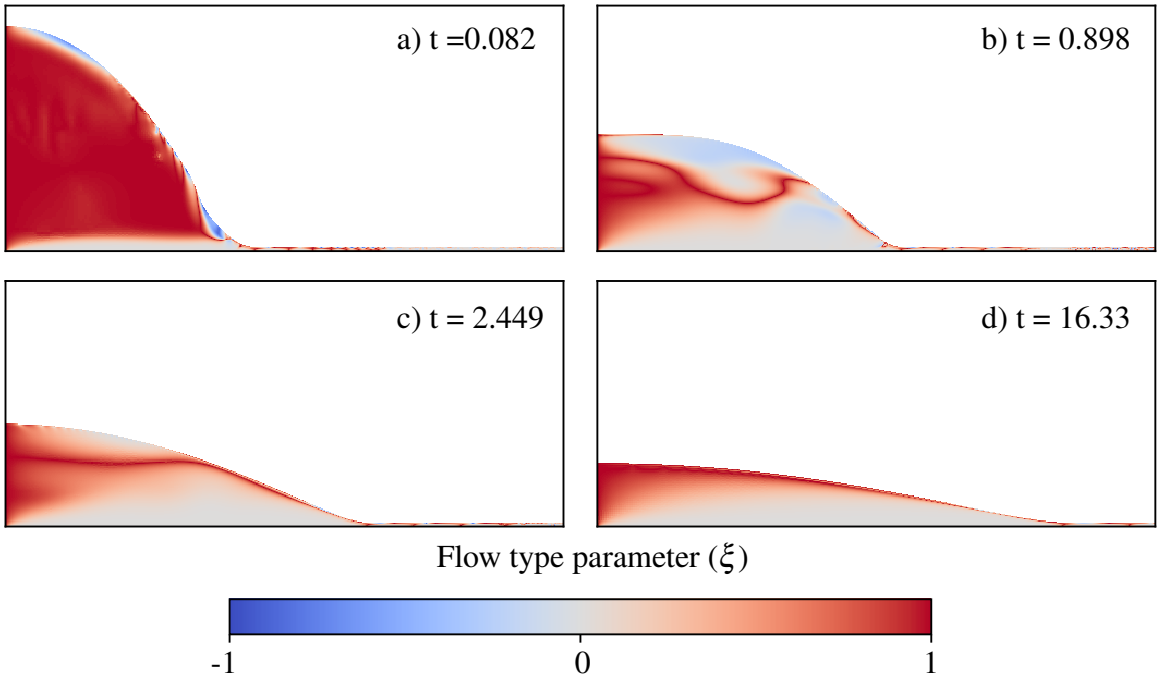

Source: Elaborated by the author.

6.6.3 Elastoviscoplastic spreading

We consider now elastoviscoplastic droplets, i.e, Wi and J are both non-zero. The complex feature of materials that exhibit a yield-stress is that they can contain regions that

dynamically transition between solid (unyielded) and fluid (yielded). Therefore, it is interesting to look at how the addition of elasticity can affect these transitions. This can be visualized by looking at the nondimensional polymeric stress $\boldsymbol{\tau}^p$ and observing in which regions this stress is above (yielded) or below (unyielded) the value of J.

Figure 54 shows the value of $\log(||\boldsymbol{\tau}^p||) - \log(J)$ at different time stamps inside a droplet with $J = 0.18$ and $Wi = 0.816$. Values above zero mean yielded regions, and below zero unyielded. As expected, the droplet is initially mostly unyielded (large blue region) since we assume there is no internal stress as our initial condition. The stress begins to increase from the contact point between the droplet and the film, which is the location of highest curvature. After some time, most of the droplet is yielded (red colors) with a particularly higher stress region near the wall and droplet edge. As time continues to increase, the stresses are dissipated and the droplet unyields once again, which eventually leads to a final shape.

Figure 54 – Distribution of the polymeric stress at different timestamps inside a elastoviscoplastic droplet with Wi $= 0.816$ and $J = 0.18$. Blue regions indicate stress below the plastocapillary number J (unyielded) and red regions are above J (yielded).

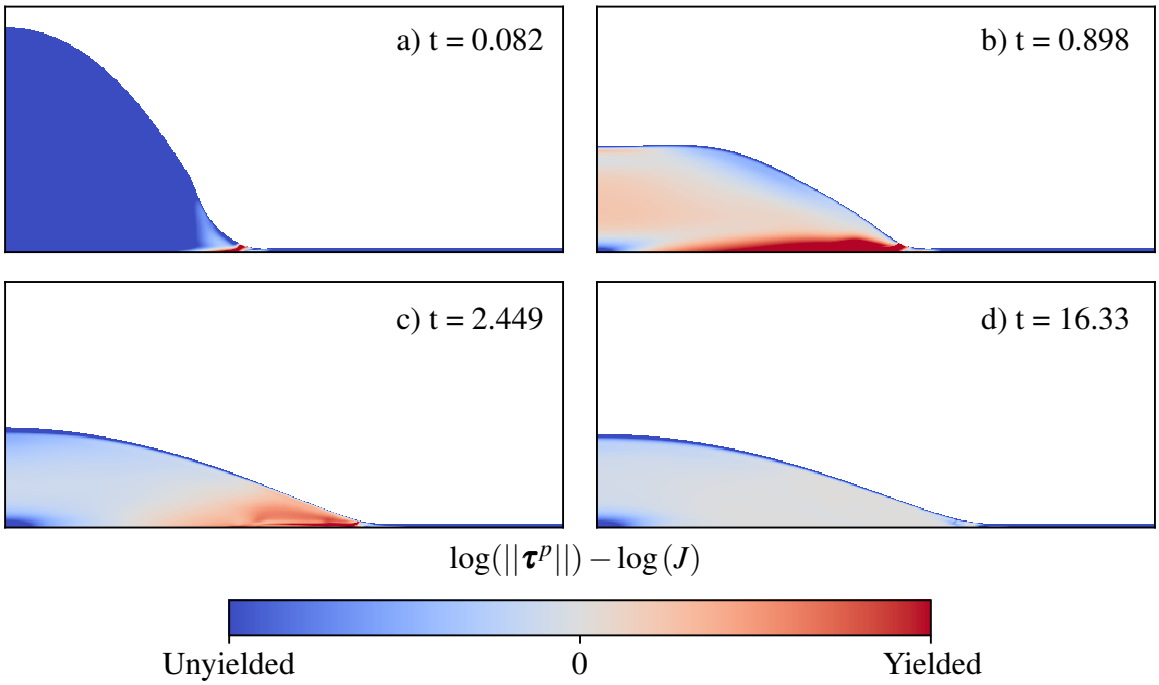

Source: Elaborated by the author.

We now extended this investigation by considering a variation of Wi and J. In Figure 55, we show the value of $\log(||\boldsymbol{\tau}^p||) - \log(J)$ at a fixed time for different combinations of J and Wi. We begin by confirming that increasing the value of J creates larger unyielded regions inside the droplet, which is expected as we increase the material yield-stress. A more interesting observation is the fact that increasing the Weissenberg number also generates larger unyielded

regions (in blue). Similarly to the explanation from section 6.6.2, increasing Wi makes the polymeric stress develop more slowly over time for a fixed shear rate, and this smaller value for $\boldsymbol{\tau}^p$ creates more regions below the yield-stress.

Looking at the high J cases (last row) in figure 55, it is also interesting to notice that, as you increase the elasticity, the droplet spreads significantly even though it is almost entirely solid. This happens due to the fact that Saramito's model describes the unyielded case as an elastic solid (as opposed to a Bingham rigid solid). This means that the material can experience deformation even in the solid state, which we see as Wi increases with a high value of J.

Figure 55 – Distribution of the polymeric stress inside the elastoviscoplastic droplet for different values of Wi and J. All snapshots are taken at time $t = 8.165$. Blue regions indicate stress below the plastocapillary number J (unyielded) and red regions are above J (yielded). We note that the colorbar limits do not include the total range of values present in the data, since we are only interested in visualizing regions that are above or below zero.

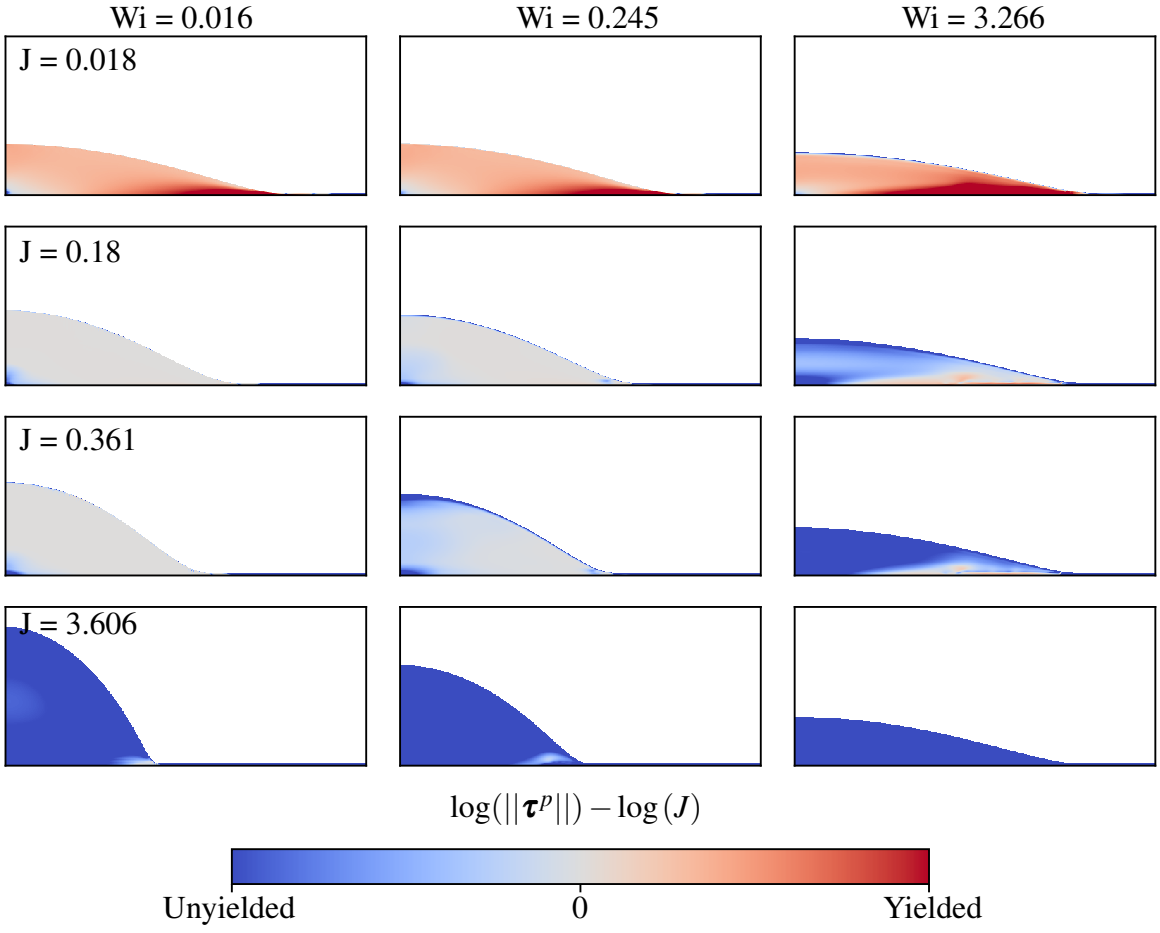

Source: Elaborated by the author.

We now perform a more quantitative study on how Wi and J affect the EVP droplet spreading. Figure 56 shows the droplet height over time for different values of J and Wi. Our first observation is that, for EVP droplets that have a yield-stress ($J > 0$) the spreading stops and a final shape is reached similarly to the purely Bingham case. Similarities to the pure viscoelastic case can also be seen, particularly in the local overshoot that is observed for most cases with the

higher Wi values shown. Another interesting observation is that the Weissenberg number seems to be more impactful for high values of J, since the curves at late times are much further from each other in the $J = 0.18$ case than in the $J = 0.018$. This indicates that the elasticity is much more influential in the solid state than in the fluid state.

Figure 56 – Time evolution of the spreading height of an elastoviscoplastic droplet for different plastocapillary and Weissenber numbers.

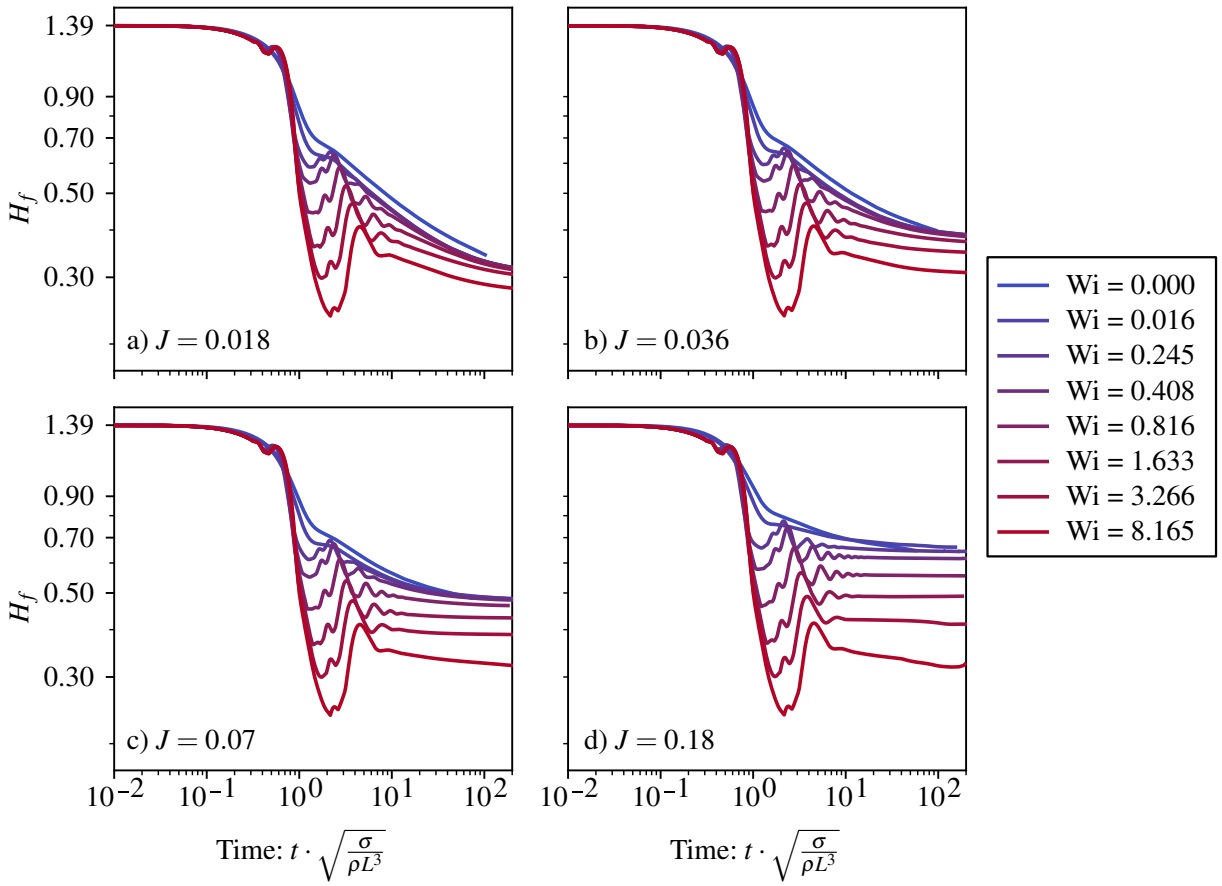

Source: Elaborated by the author.

Finally, we can investigate how the Weissenberg number changes the scaling law validated in section 6.5.1 for purely viscoplastic droplets. In Figure 57 we show the final radius versus J for different values of Wi. The limit $J = 0$ corresponds to a viscopalstic Bingham fluid shown in section 6.5.1 and the gray line represents the theoretical scaling for this case. As Wi increases we can see that the droplet spreads more, particularly for higher values of J. For higher Wi values we also see a decrease in the critical value of J from which the spreading stays constant. This happens because, as we saw earlier, the elasticity promotes unyielded droplets and, for droplets that are already unyielded, further increasing the value of J does not introduce any changes in the equations.

Figure 57 – Final spreading radius (top) and height (bottom) of an elastoviscoplastic droplet as a function of the plastocapillary and Weissenberg numbers.

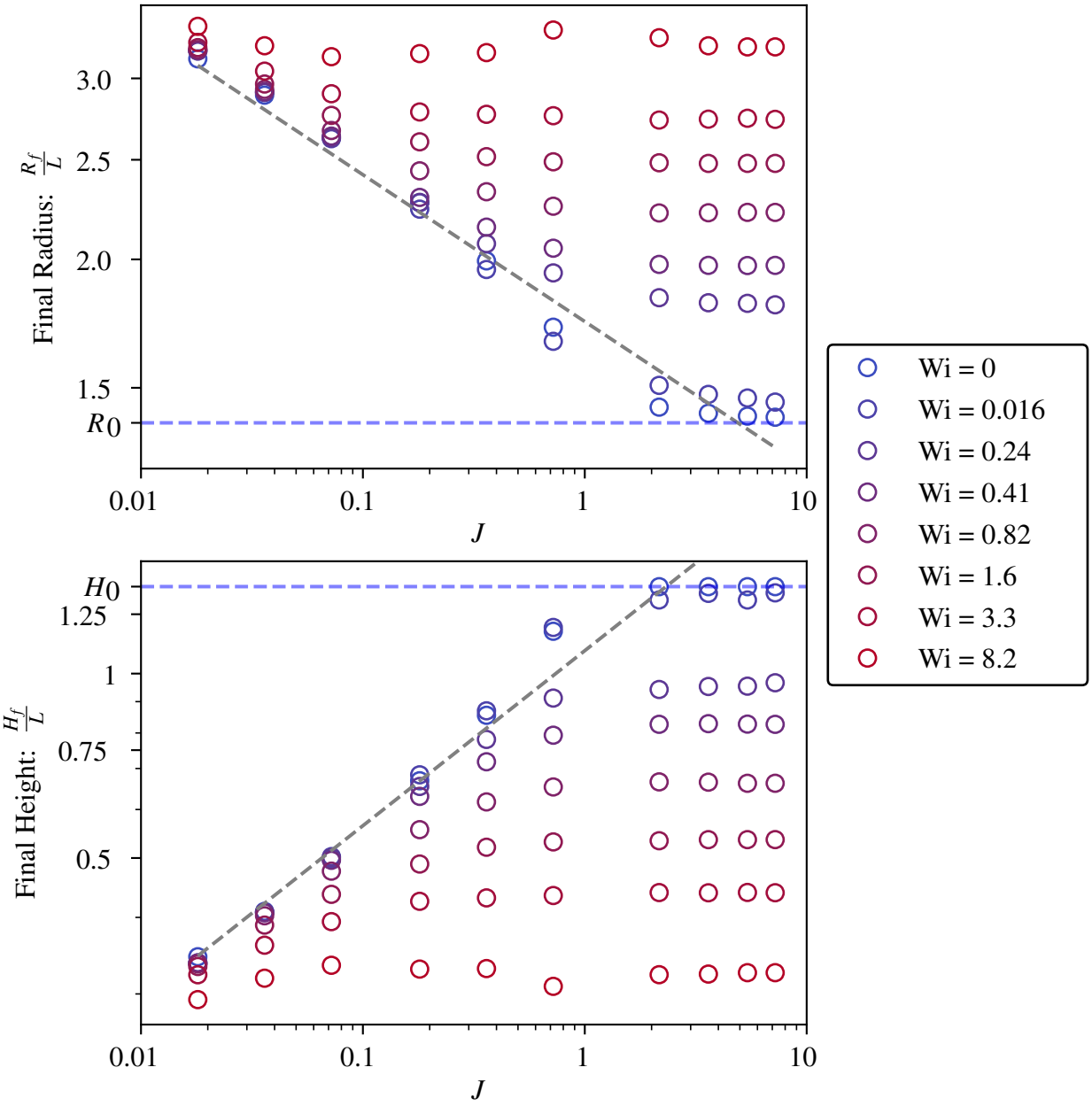

Source: Elaborated by the author.

6.7 Conclusions

In this chapter we numerically investigated the role of elasticity in the spreading of a yield-stress droplet. By using the well-known Saramito model for elastoviscoplastic materials, we were able to perform direct numerical simulations to understand how the spreading occurs.

After non-dimensionalizing the problem, we focus our study on the importance of two nondimensional groups: the plastocappilary number and the Weissenberg number. We

confirm that increasing the plastocappilary number reduces the droplet spreading, as previously discovered in the literature. More interestingly, we see that the Weissenberg number, related to elasticity, works in the opposite direction and promotes more spreading. This effect is associated to the polymeric relaxation time, which delays the development of the internal droplet stresses, allowing the droplet to spread with less resistance.

Moreover, we also see that varying the Weissenberg number has a greater impact when the plastocapillary number is high. This indicates that, in Saramito's model, the elasticity is more impactful when the material is in the elastic solid state than when it is a fluid.

We believe the results in this chapter could shed light on the importance of elastic parameters in common industrial problems such as 3D printing with spreading of droplets.

CHAPTER

7

GENERAL CONCLUSION

In this thesis, we have numerically studied confined and free surface flows of complex fluids. A description of the mathematical formulation for these problems was presented, along with the numerical methods used to solve the resulting differential equations.

Natural Stress formulation

The natural stress formulation (NSF) was investigated for viscoelastic fluids as an attempt to better calculate the polymeric properties in geometries that contain sharp corners. While the NSF still has some instability issues, it has also shown good results when it comes to accuracy in comparison to the more traditional Cartesian formulation. This accuracy is mostly seen in the asymptotic behaviour of flow properties near geometric singularities.

Viscoelastic binary droplet collisions

We also used our code to study simulations in which topological changes should take place, more specifically binary drop collisions. In this chapter, we were able to numerically study how shear-thinning and viscoelastic droplets behave after collisions. For shear-thinning models, we verified that droplets that are more shear-thinning are more likely to separate after coalescence, a result that is expected from literature results.

For viscoelastic Oldroyd-B simulations, we observe that, like surface tension, elasticity tends to keep the integrity of the coalesced drop, avoiding separation. When the PTT model is considered, both shear-thinning and elasticity effects were studied simultaneously and we observe that they can create opposite effects.

Curvature calculation using machine learning

A novel algorithm was proposed to calculate the local curvature of Front-Tracking interfaces using machine learning. We showed that accurate results can be obtained for simple shapes like circles or sinoids. Furthermore, we also performed free-surface flows with large droplet deformations, in which accurate estimation of curvature is important. We were able to

show that our proposed algorithm is also capable of handling these simulations.

Elastoviscoplastic droplet spreading

Finally, we initiated a study of models that combine elasticity and plasticity, in order to obtain an elastoviscoplastic response. The Saramito EVP model was implemented in the platform Basilisk C and used to simulate a droplet spreading over a thin-film. We were able to verify theoretical scaling laws predicted for the spreading of Newtonian and purely viscoplastic fluids. For purely viscoelastic droplets, we can see that elasticity (given by the Weissenberg number) seems to favour spreading, due to smaller viscous dissipation in the beginning of the spreading. A similar behaviour is observed for fully EVP droplets. Interestingly, we also observe that elasticity has a bigger impact for droplets with high yield-stress, which shows that solids are more impacted by Saramito's elasticity than fluids.

BIBLIOGRAPHY

ABOUBACAR, M.; MATALLAH, H.; WEBSTER, M. Highly elastic solutions for oldroyd-b and phan-thien/tanner fluids with a finite volume/element method: planar contraction flows. **Journal of Non-Newtonian Fluid Mechanics**, Elsevier BV, v. 103, n. 1, p. 65–103, Mar. 2002. Citation on page 43.

AFONSO, A. M.; OLIVEIRA, P. J.; PINHO, F. T.; ALVES, M. A. Dynamics of high-deborah-number entry flows: a numerical study. **Journal of Fluid Mechanics**, Cambridge University Press (CUP), v. 677, p. 272–304, Apr. 2011. Citations on pages 29, 43, and 47.

AL-DIRAWI, K.; AL-GHAITHI, K.; SYKES, T.; PITA, J. C.; BAYLY, A. Inertial stretching separation in binary droplet collisions. **Journal of Fluid Mechanics**, Cambridge University Press (CUP), v. 927, n. A9, p. 1–12, 2021. Citations on pages 59 and 60.

AL-DIRAWI, K. H.; BAYLY, A. E. A new model for the bouncing regime boundary in binary droplet collisions. **Physics of Fluids**, AIP Publishing, v. 31, n. 2, p. 027105, Feb. 2019. Citations on pages 59, 64, 67, 91, and 92.

ALVES, M. A.; OLIVEIRA, P. J.; PINHO, F. T. Benchmark solutions for the flow of oldroyd-b and PTT fluids in planar contractions. **Journal of Non-Newtonian Fluid Mechanics**, Elsevier BV, v. 110, n. 1, p. 45–75, Feb. 2003. Citations on pages 43 and 58.

ARAÚJO, M.; FERNANDES, C.; FERRÁS, L.; TUKOVIĆ, Ž.; JASAK, H.; NÓBREGA, J. A stable numerical implementation of integral viscoelastic models in the OpenFOAM computational library. **Computers & Fluids**, Elsevier BV, v. 172, p. 728–740, Aug. 2018. Citations on pages 29 and 43.

ASHGRIZ, N.; POO, J. Y. Coalescence and separation in binary collisions of liquid drops. **Journal of Fluid Mechanics**, Cambridge University Press (CUP), v. 221, p. 183–204, Dec. 1990. Citation on page 59.

BALMFORTH, N.; CRASTER, R.; PERONA, P.; RUST, A.; SASSI, R. Viscoplastic dam breaks and the bostwick consistometer. **Journal of Non-Newtonian Fluid Mechanics**, Elsevier BV, v. 142, n. 1-3, p. 63–78, Mar. 2007. Citation on page 96.

BALMFORTH, N. J.; FRIGAARD, I. A.; OVARLEZ, G. Yielding to stress: Recent developments in viscoplastic fluid mechanics. **Annual Review of Fluid Mechanics**, v. 46, n. 1, p. 121–146, 2014. Citation on page 22.

BARNES, H. A. The yield stress-a review or ‘παντα ρει’ everything flows? **Journal of Non-Newtonian Fluid Mechanics**, v. 81, n. 1, p. 133–178, 1999. ISSN 0377-0257. Citation on page 96.

BERGEMANN, N.; JUEL, A.; HEIL, M. Viscous drops on a layer of the same fluid: from sinking, wedging and spreading to their long-time evolution. **Journal of Fluid Mechanics**, Cambridge University Press (CUP), v. 843, p. 1–28, Mar. 2018. Citation on page 96.

BINGHAM, E. **Fluidity and Plasticity**. [S.l.]: McGraw-Hill Book Company, Incorporated, 1922. (International chemical series). Citation on page 21.

BIRD, R.; ARMSTRONG, R.; HASSAGER, O. **Dynamics of Polymeric Liquids, Volume 1: Fluid Mechanics**. [S.l.]: Wiley, 1987. (Dynamics of Polymeric Liquids). ISBN 9780471802457. Citation on page 21.

BOGER, D. V. Viscoelastic flows through contractions. **Annual Review of Fluid Mechanics**, Annual Reviews, v. 19, n. 1, p. 157–182, Jan. 1987. Citation on page 43.

CHEDDADI, I.; SARAMITO, P. A new operator splitting algorithm for elastoviscoplastic flow problems. **Journal of Non-Newtonian Fluid Mechanics**, v. 202, p. 13 – 21, 2013. ISSN 0377-0257. Citation on page 22.

CHEDDADI, I.; SARAMITO, P.; DOLLET, B.; RAUFASTE, C.; GRANER, F. Understanding and predicting viscous, elastic, plastic flows. **The European Physical Journal E**, v. 34, n. 1, p. 1, 2011. Citation on page 96.

CHEN, S.; BERTOLA, V. Morphology of viscoplastic drop impact on viscoplastic surfaces. **Soft Matter**, Royal Society of Chemistry (RSC), v. 13, n. 4, p. 711–719, 2017. Citation on page 96.

CHORIN, A.; MARSDEN, J. **A mathematical introduction to fluid mechanics**. [S.l.]: Springer-Verlag, 1979. ISBN 9783540904069. Citation on page 32.

DATTA, S. S.; ARDEKANI, A. M.; ARRATIA, P. E.; BERIS, A. N.; BISCHOFBERGER, I.; MCKINLEY, G. H.; EGGERS, J. G.; LÓPEZ-AGUILAR, J. E.; FIELDING, S. M.; FRISHMAN, A.; GRAHAM, M. D.; GUASTO, J. S.; HAWARD, S. J.; SHEN, A. Q.; HORMOZI, S.; MOROZOV, A.; POOLE, R. J.; SHANKAR, V.; SHAQFEH, E. S. G.; STARK, H.; STEINBERG, V.; SUBRAMANIAN, G.; STONE, H. A. Perspectives on viscoelastic flow instabilities and elastic turbulence. **Physical Review Fluids**, American Physical Society (APS), v. 7, n. 8, Aug. 2022. Citation on page 23.

DEAN, W. R.; MONTAGNON, P. E. On the steady motion of viscous liquid in a corner. **Mathematical Proceedings of the Cambridge Philosophical Society**, Cambridge University Press (CUP), v. 45, n. 3, p. 389–394, Jul. 1949. Citation on page 50.

DERBY, B. Inkjet printing of functional and structural materials: Fluid property requirements, feature stability, and resolution. **Annual Review of Materials Research**, Annual Reviews, v. 40, n. 1, p. 395–414, Jun. 2010. Citations on pages 22 and 96.

DIMITRIOU, C. J.; MCKINLEY, G. H. A canonical framework for modeling elasto-viscoplasticity in complex fluids. **Journal of Non-Newtonian Fluid Mechanics**, 2018. ISSN 0377-0257. Citation on page 22.

DONG, X.; LIU, H.; WANG, Q.; PANG, Z.; WANG, C. Non-newtonian flow characterization of heavy crude oil in porous media. **Journal of Petroleum Exploration and Production Technology**, Springer Science and Business Media LLC, v. 3, n. 1, p. 43–53, Nov. 2012. Citation on page 21.

DU, J.; FIX, B.; GLIMM, J.; JIA, X.; LI, X.; LI, Y.; WU, L. A simple package for front tracking. **Journal of Computational Physics**, Elsevier BV, v. 213, n. 2, p. 613–628, Apr. 2006. Citation on page 83.

DULLAERT, K.; MEWIS, J. A structural kinetics model for thixotropy. **Journal of Non-Newtonian Fluid Mechanics**, v. 139, n. 1, p. 21 – 30, 2006. ISSN 0377-0257. Citation on page 22.

DUPONT, S.; MARCHAL, J.; CROCHET, M. Finite element simulation of viscoelastic fluids of the integral type. **Journal of Non-Newtonian Fluid Mechanics**, Elsevier BV, v. 17, n. 2, p. 157–183, Jan. 1985. Citation on page 29.

EVANS, J. Re-entrant corner behaviour of the giesekus fluid with a solvent viscosity. **Journal of Non-Newtonian Fluid Mechanics**, Elsevier BV, v. 165, n. 9-10, p. 538–543, May 2010. Citation on page 44.

____. Re-entrant corner behaviour of the PTT fluid with a solvent viscosity. **Journal of Non-Newtonian Fluid Mechanics**, Elsevier BV, v. 165, n. 9-10, p. 527–537, May 2010. Citation on page 44.

EVANS, J.; FRANÇA, H.; JUNIOR, I. P.; OISHI, C. Testing viscoelastic numerical schemes using the oldroyd-b fluid in newtonian kinematics. **Applied Mathematics and Computation**, Elsevier BV, p. 125106, Mar. 2020. Citations on pages 50 and 52.

EVANS, J.; OISHI, C. Transient computations using the natural stress formulation for solving sharp corner flows. **Journal of Non-Newtonian Fluid Mechanics**, Elsevier BV, v. 249, p. 48–52, Nov. 2017. Citation on page 43.

EVANS, J. D.; FRANÇA, H. L.; OISHI, C. M. Application of the natural stress formulation for solving unsteady viscoelastic contraction flows. **Journal of Computational Physics**, Elsevier BV, v. 388, p. 462–489, Jul. 2019. Citations on pages 12, 44, 52, 54, 55, and 84.

FATTAL, R.; KUPFERMAN, R. Constitutive laws for the matrix-logarithm of the conformation tensor. **Journal of Non-Newtonian Fluid Mechanics**, Elsevier BV, v. 123, n. 2-3, p. 281–285, Nov. 2004. Available: <https://doi.org/10.1016/j.jnnfm.2004.08.008>. Citation on page 100.

FAVERO, J.; SECCHI, A.; CARDOZO, N.; JASAK, H. Viscoelastic flow analysis using the software OpenFOAM and differential constitutive equations. **Journal of Non-Newtonian Fluid Mechanics**, Elsevier BV, v. 165, n. 23-24, p. 1625–1636, Dec. 2010. Citation on page 43.

FEBRES, M.; LEGENDRE, D. Enhancement of a 2d front-tracking algorithm with a non-uniform distribution of Lagrangian markers. **Journal of Computational Physics**, Elsevier BV, v. 358, p. 173–200, Apr. 2018. Available: <https://doi.org/10.1016/j.jcp.2017.12.021>. Citation on page 83.

FIFTH Workshop on Numerical Methods in Non-Newtonian Flow. **Journal of Non-Newtonian Fluid Mechanics**, Elsevier BV, v. 29, p. ix–xii, Jan. 1988. Citation on page 43.

FINOTELLO, G.; DE, S.; VROUWENVELDER, J.; PADDING, J.; BUIST, K.; JONGSMA, A.; INNINGS, F.; KUIPERS, J. Experimental investigation of non–newtonian droplet collisions: the role of extensional viscosity. **Experiments in Fluids**, v. 59, n. 113, p. 1–16, 2018. Citations on pages 12, 61, 64, 69, 70, 71, and 78.

FINOTELLO, G.; PADDING, J. T.; DEEN, N. G.; JONGSMA, A.; INNINGS, F.; KUIPERS, J. A. M. Effect of viscosity on droplet-droplet collisional interaction. **Physics of Fluids**, AIP Publishing, v. 29, n. 6, p. 067102, Jun. 2017. Citation on page 60.

FOCKE, C.; BOTHE, D. Computational analysis of binary collisions of shear-thinning droplets. **Journal of Non-Newtonian Fluid Mechanics**, Elsevier BV, v. 166, p. 799–810, Apr. 2011. Citation on page 61.

FOCKE, C.; KUSCHEL, M.; SOMMERFIELD, M.; BOTHE, D. Collision between high and low viscosity droplets: direct numerical simulations and experiments. **International Journal of Multiphase Flow**, v. 56, p. 81–92, 2013. Citation on page 61.

FORTIN, A.; ZINE, A.; AGASSANT, J.-F. Computing viscoelastic fluid flow problems at low cost. **Journal of Non-Newtonian Fluid Mechanics**, Elsevier BV, v. 45, n. 2, p. 209–229, Nov. 1992. Citation on page 44.

FRAGGEDAKIS, D.; DIMAKOPOULOS, Y.; TSAMOPOULOS, J. Yielding the yield stress analysis: A thorough comparison of recently proposed elasto-visco-plastic (evp) fluid models. **Journal of Non-Newtonian Fluid Mechanics**, v. 236, p. 104 – 122, 2016. ISSN 0377-0257. Citations on pages 22 and 95.

FRANçA, H. **Um método numérico para o tratamento de mudanças topológicas em escoamentos viscoelásticos com superfície livre**. Master's Thesis (Master's Thesis) — Universidade Estadual Paulista, 2018. Citations on pages 34 and 38.

FRIGAARD, I.; NOUAR, C. On the usage of viscosity regularisation methods for visco-plastic fluid flow computation. **Journal of Non-Newtonian Fluid Mechanics**, Elsevier BV, v. 127, n. 1, p. 1–26, Apr. 2005. Citation on page 101.

FULLER, G.; CATHEY, C.; HUBBARD, B.; ZEBROWSKI, B. Extensional viscosity measurements for low-viscosity fluids. **Journal of Rheology**, v. 31, n. 3, p. 235–249, 1987. Citation on page 61.

GERMAN, G.; BERTOLA, V. Impact of shear-thinning and yield-stress drops on solid substrates. **Journal of Physics: Condensed Matter**, IOP Publishing, v. 21, n. 37, p. 375111, Aug. 2009. Citation on page 96.

GIESEKUS, H. A simple constitutive equation for polymer fluids based on the concept of deformation-dependent tensorial mobility. **Journal of Non-Newtonian Fluid Mechanics**, Elsevier BV, v. 11, n. 1-2, p. 69–109, Jan. 1982. Citation on page 44.

GLIMM, J.; GROVE, J.; LINDQUIST, B.; MCBRYAN, O. A.; TRYGGVASON, G. The bifurcation of tracked scalar waves. **SIAM Journal on Scientific and Statistical Computing**, Society for Industrial & Applied Mathematics (SIAM), v. 9, n. 1, p. 61–79, Jan. 1988. Citations on pages 38 and 39.

GLIMM, J.; MCBRYAN, O.; MENIKOFF, R.; SHARP, D. Front tracking applied to Rayleigh–Taylor instability. **SIAM Journal on Scientific and Statistical Computing**, Society for Industrial & Applied Mathematics (SIAM), v. 7, n. 1, p. 230–251, Jan. 1986. Citation on page 83.

GONNERMANN, H. M.; MANGA, M. The fluid mechanics inside a volcano. **Annual Review of Fluid Mechanics**, Annual Reviews, v. 39, n. 1, p. 321–356, Jan. 2007. Citations on pages 22 and 24.

GOTAAS, C.; HAVELKA, P.; JAKOBSEN, H.; SVENDSEN, H.; HASE, M. Effect of viscosity on droplet-droplet collision outcome: Experimental study and numerical comparison. **Physics of Fluids**, AIP Publishing, v. 19, n. 102106, p. 1–17, 2019. Citations on pages 59 and 60.

HERSCHEL, W. H.; BULKLEY, R. Konsistenzmessungen von gummi-benzollösungen. **Kolloid-Zeitschrift**, Springer Science and Business Media LLC, v. 39, n. 4, p. 291–300, Aug. 1926. Citation on page 21.

HINTERBICHLER, H.; PLANCHETTE, C.; BRENN, G. Ternary drop collisions. **Experiments in Fluids**, v. 56, n. 190, p. 1–12, 2015. Citation on page 61.

HIRSCHLER, M.; OGER, G.; NIECKEN, U.; Le Touze, D. Modeling of droplet collisions using Smoothed Particle Hydrodynamics. **International Journal of Multiphase Flow**, Elsevier BV, v. 95, p. 175–187, 2017. Citation on page 61.

HIRT, C.; NICHOLS, B. Volume of fluid (VOF) method for the dynamics of free boundaries. **Journal of Computational Physics**, Elsevier BV, v. 39, n. 1, p. 201–225, Jan. 1981. Citations on pages 83 and 101.

IZBASSAROV, D.; ROSTI, M. E.; ARDEKANI, M. N.; SARABIAN, M.; HORMOZI, S.; BRANDT, L.; TAMMISOLA, O. Computational modeling of multiphase viscoelastic and elastoviscoplastic flows. **International Journal for Numerical Methods in Fluids**, v. 88, n. 12, p. 521–543, 2018. Citation on page 24.

IZBASSAROV, D.; TAMMISOLA, O. Dynamics of an elastoviscoplastic droplet in a newtonian medium under shear flow. **Physical Review Fluids**, American Physical Society (APS), v. 5, n. 11, Nov. 2020. Citation on page 97.

JALAAL, M.; BALMFORTH, N. J.; STOEBER, B. Slip of spreading viscoplastic droplets. **Langmuir**, American Chemical Society (ACS), v. 31, n. 44, p. 12071–12075, Oct. 2015. Citation on page 96.

JALAAL, M.; SEYFERT, C.; SNOEIJER, J. H. Capillary ripples in thin viscous films. **Journal of Fluid Mechanics**, Cambridge University Press (CUP), v. 880, p. 430–440, Oct. 2019. Citation on page 96.

JALAAL, M.; STOEBER, B.; BALMFORTH, N. J. Spreading of viscoplastic droplets. **Journal of Fluid Mechanics**, Cambridge University Press (CUP), v. 914, Mar. 2021. Citations on pages 15, 97, 103, 104, and 105.

JIANG, Y.; UMEMURA, A.; LAW, C. An experimental investigation on the collision behaviour of hydrocarbon droplets. **Journal of Fluid Mechanics**, Cambridge University Press (CUP), v. 234, p. 171–190, Jan. 1992. Citation on page 59.

JUNIOR, I. L. P.; OISHI, C. M.; AFONSO, A. M.; ALVES, M. A.; PINHO, F. T. Numerical study of the square-root conformation tensor formulation for confined and free-surface viscoelastic fluid flows. **Advanced Modeling and Simulation in Engineering Sciences**, Springer Science and Business Media LLC, v. 3, n. 1, Feb. 2016. Citation on page 24.

KIM, J. M.; KIM, C.; KIM, J. H.; CHUNG, C.; AHN, K. H.; LEE, S. J. High-resolution finite element simulation of 4:1 planar contraction flow of viscoelastic fluid. **Journal of Non-Newtonian Fluid Mechanics**, Elsevier BV, v. 129, n. 1, p. 23–37, Aug. 2005. Citation on page 43.

LARIOS-CÁRDENAS, L.; GIBOU, F. A deep learning approach for the computation of curvature in the level-set method. **SIAM Journal on Scientific Computing**, Society for Industrial & Applied Mathematics (SIAM), v. 43, n. 3, p. A1754–A1779, Jan. 2021. Citation on page 84.

LARIOS-CáRDENAS, L.; GIBOU., F. A hybrid inference system for improved curvature estimation in the level-set method using machine learning. **https://arxiv.org/abs/2104.02951**, 2021. Citation on page 84.

LI, X. G.; FRITSCHING, U. Numerical investigation of binary droplet collisions in all relevant collision regimes. **The Journal of Computational Multiphase Flows**, v. 4, n. 4, p. 207–224, Dec. 2011. Citations on pages 59 and 60.

LINK, F. B.; FREY, S.; THOMPSON, R. L.; NACCACHE, M. F.; MENDES, P. R. de S. Plane flow of thixotropic elasto-viscoplastic materials through a 1:4 sudden expansion. **Journal of Non-Newtonian Fluid Mechanics**, v. 220, p. 162 – 174, 2015. ISSN 0377-0257. Viscoplastic fluids: From theory to application 2013. Citation on page 22.

LIU, C.; SI, Z. An incremental pressure correction finite element method for the time-dependent oldroyd flows. **Applied Mathematics and Computation**, Elsevier BV, v. 351, p. 99–115, Jun. 2019. Citation on page 43.

LIU, K. F.; MEI, C. C. Slow spreading of a sheet of bingham fluid on an inclined plane. **Journal of Fluid Mechanics**, Cambridge University Press (CUP), v. 207, p. 505–529, Oct. 1989. Citation on page 96.

LIU, X.; MORITA, K.; ZHANG, S. Machine-learning-based surface tension model for multiphase flow simulation using particle method. **International Journal for Numerical Methods in Fluids**, Wiley, v. 93, n. 2, p. 356–368, Jul. 2020. Citation on page 84.

LIU, Y.; BALMFORTH, N.; HORMOZI, S. Axisymmetric viscoplastic dambreaks and the slump test. **Journal of Non-Newtonian Fluid Mechanics**, Elsevier BV, v. 258, p. 45–57, Aug. 2018. Citation on page 96.

LÓPEZ-AGUILAR, J.; WEBSTER, M. F.; TAMADDON-JAHROMI, H.; MANERO, O. Predictions for circular contraction-expansion flows with viscoelastoplastic & thixotropic fluids. **Journal of Non-Newtonian Fluid Mechanics**, v. 261, p. 188 – 210, 2018. ISSN 0377-0257. Citation on page 22.

LÓPEZ-AGUILAR, J. E.; WEBSTER, M. F.; TAMADDON-JAHROMI, H. R.; MANERO, O. Numerical modelling of thixotropic and viscoelastoplastic materials in complex flows. **Rheologica Acta**, v. 54, n. 4, p. 307–325, 2015. Citation on page 22.

____. A comparative numerical study of time-dependent structured fluids in complex flows. **Rheologica Acta**, v. 55, n. 3, p. 197–214, 2016. Citation on page 22.

LUU, L.-H.; FORTERRE, Y. Drop impact of yield-dtress fluids. **Journal of Fluid Mechanics**, Cambridge University Press, v. 632, p. 301–327, 2009. Citation on page 96.

MACKAY, M. E. The importance of rheological behavior in the additive manufacturing technique material extrusion. **Journal of Rheology**, Society of Rheology, v. 62, n. 6, p. 1549–1561, Nov. 2018. Citation on page 96.

MANGIAVACCHI, N.; CASTELO, A.; TOMé, M. F.; CUMINATO, J. A.; OLIVEIRA, M. L. Bambozzi de; MCKEE, S. An effective implementation of surface tension using the marker and cell method for axisymmetric and planar flows. **SIAM J. Sci. Comput.**, Society for Industrial and Applied Mathematics, USA, v. 26, n. 4, p. 1340–1368, Apr. 2005. ISSN 1064-8275. Citation on page 83.

MARTINS, F.; OISHI, C.; AFONSO, A.; ALVES, M. A numerical study of the kernel-conformation transformation for transient viscoelastic fluid flows. **Journal of Computational Physics**, Elsevier BV, v. 302, p. 653–673, Dec. 2015. Citations on pages 84 and 90.

MEDVID'OVÁ, M. L.; NOTSU, H.; SHE, B. Energy dissipative characteristic schemes for the diffusive oldroyd-b viscoelastic fluid. **International Journal for Numerical Methods in Fluids**, Wiley, v. 81, n. 9, p. 523–557, Dec. 2015. Citation on page 43.

MENDES, P. R. de S. Modeling the thixotropic behavior of structured fluids. **Journal of Non-Newtonian Fluid Mechanics**, v. 164, n. 1, p. 66 – 75, 2009. ISSN 0377-0257. Citation on page 22.

____. Thixotropic elasto-viscoplastic model for structured fluids. **Soft Matter**, The Royal Society of Chemistry, v. 7, p. 2471–2483, 2011. Citations on pages 22 and 95.

MENDES, P. R. de S.; THOMPSON, R. L. A unified approach to model elasto-viscoplastic thixotropic yield-stress materials and apparent yield-stress fluids. **Rheologica Acta**, v. 52, n. 7, p. 673–694, 2013. Citation on page 22.

MEWIS, J.; WAGNER, N. J. Thixotropy. **Advances in Colloid and Interface Science**, v. 147-148, p. 214 – 227, 2009. ISSN 0001-8686. Colloids, polymers and surfactants. Special Issue in honour of Brian Vincent. Citation on page 22.

MITSOULIS, E.; TSAMOPOULOS, J. Numerical simulations of complex yield-stress fluid flows. **Rheologica Acta**, v. 56, n. 3, p. 231–258, 2017. Citation on page 22.

MOFFATT, H. K. Viscous and resistive eddies near a sharp corner. **Journal of Fluid Mechanics**, Cambridge University Press (CUP), v. 18, n. 1, p. 1–18, Jan. 1964. Citation on page 50.

NASSAR, B.; MENDES, P. R. de S.; NACCACHE, M. F. Flow of elasto-viscoplastic liquids through an axisymmetric expansion–contraction. **Journal of Non-Newtonian Fluid Mechanics**, Elsevier BV, v. 166, n. 7-8, p. 386–394, Apr. 2011. Citation on page 96.

NIKOLOPOULOS, N.; THEODORAKAKOS, A.; BERGELES, G. Off-centre binary collision of droplets: A numerical investigation. **International Journal of Heat and Mass Transfer**, Elsevier BV, v. 52, n. 19-20, p. 4160–4174, Sep. 2009. Citations on pages 59 and 60.

NOBARI, M. R.; JAN, Y.-J.; TRYGGVASON, G. Head-on collision of drops—a numerical investigation. **Physics of Fluids**, AIP Publishing, v. 8, n. 1, p. 29–42, Jan. 1996. Citations on pages 59, 60, and 92.

NOBARI, M. R. H.; TRYGGVASON, G. Numerical simulations of three-dimensional drop collisions. **AIAA Journal**, American Institute of Aeronautics and Astronautics (AIAA), v. 34, n. 4, p. 750–755, Apr. 1996. Citations on pages 59 and 60.

OISHI, C.; MARTINS, F.; TOMÉ, M.; CUMINATO, J.; MCKEE, S. Numerical solution of the eXtended pom-pom model for viscoelastic free surface flows. **Journal of Non-Newtonian Fluid Mechanics**, Elsevier BV, v. 166, n. 3-4, p. 165–179, Feb. 2011. Citation on page 29.

OISHI, C.; THOMPSON, R.; MARTINS, F. Impact of capillary drops of complex fluids on a solid surface. **Physics of Fluids**, AIP Publishing, v. 31, p. 123109, Jun. 2019. Citations on pages 78 and 96.

____. Normal and oblique drop impact of yield stress fluids with thixotropic effects. **Journal of Fluid Mechanics**, Cambridge University Press (CUP), v. 876, p. 642–679, Aug. 2019. Citations on pages 84 and 90.

OISHI, C.; TOMÉ, M.; CUMINATO, J.; MCKEE, S. An implicit technique for solving 3D low Reynolds number moving free surface flows. **Journal of Computational Physics**, v. 227, n. 16, p. 7446 – 7468, 2008. ISSN 0021-9991. Citation on page 36.

OISHI, C. M.; MARTINS, F. P.; THOMPSON, R. L. The "avalanche effect" of an elasto-viscoplastic thixotropic material on an inclined plane. **Journal of Non-Newtonian Fluid Mechanics**, v. 247, p. 165 – 177, 2017. ISSN 0377-0257. Citations on pages 24 and 96.

OISHI, C. M.; THOMPSON, R. L.; MARTINS, F. P. Transient motions of elasto-viscoplastic thixotropic materials subjected to an imposed stress field and to stress-based free-surface boundary conditions. **International Journal of Engineering Science**, v. 109, p. 165 – 201, 2016. ISSN 0020-7225. Citation on page 24.

OLDROYD, J. G. On the formulation of rheological equations of state. **Proceedings of the Royal Society of London. Series A. Mathematical and Physical Sciences**, The Royal Society, v. 200, n. 1063, p. 523–541, Feb. 1950. Citations on pages 21 and 22.

OSHER, S.; SETHIAN, J. Fronts propagating with curvature-dependent speed: Algorithms based on hamilton-jacobi formulations. **Journal of Computational Physics**, Elsevier BV, v. 79, n. 1, p. 12–49, Nov. 1988. Citation on page 83.

PAN, K.-L.; LAW, C. K.; ZHOU, B. Experimental and mechanistic description of merging and bouncing in head-on binary droplet collision. **Journal of Applied Physics**, AIP Publishing, v. 103, n. 6, p. 064901, Mar. 2008. Citations on pages 14, 59, and 91.

PAPANASTASIOU, T. C. Flows of materials with yield. **Journal of Rheology**, Society of Rheology, v. 31, n. 5, p. 385–404, Jul. 1987. Citation on page 101.

PATEL, H.; PANDA, A.; KUIPERS, J.; PETERS, E. Computing interface curvature from volume fractions: A machine learning approach. **Computers & Fluids**, Elsevier BV, v. 193, p. 104263, Oct. 2019. Citation on page 84.

PHAN-THIEN, N. A nonlinear network viscoelastic model. **Journal of Rheology**, Society of Rheology, v. 22, n. 3, p. 259–283, Jun. 1978. Citation on page 44.

PIMENTA, F.; ALVES, M. Stabilization of an open-source finite-volume solver for viscoelastic fluid flows. **Journal of Non-Newtonian Fluid Mechanics**, Elsevier BV, v. 239, p. 85–104, Jan. 2017. Citations on pages 29 and 43.

PLANCHETTE, C.; HINTERBICHLER, H.; LIU, M.; BOTHE, D.; BRENN, G. Colliding drops as coalescing and fragmenting liquid springs. **Journal of Fluid Mechanics**, Cambridge University Press (CUP), v. 814, p. 277–300, 2017. Citations on pages 12, 59, 60, 66, and 67.

POOLE, R. J.; ALVES, M. A.; OLIVEIRA, P. J. Purely elastic flow asymmetries. **Physical Review Letters**, American Physical Society (APS), v. 99, n. 16, Oct. 2007. Citation on page 43.

POPINET, S. A quadtree-adaptive multigrid solver for the serre–green–naghdi equations. **Journal of Computational Physics**, Elsevier BV, v. 302, p. 336–358, Dec. 2015. Citations on pages 100 and 101.

____. Numerical models of surface tension. **Annual Review of Fluid Mechanics**, Annual Reviews, v. 50, n. 1, p. 49–75, Jan. 2018. Citation on page 83.

POPINET, S.; COLLABORATORS. **Basilisk C**. 2013–2021. Accessed on Month Day, Year. Available: <http://basilisk.fr>. Citation on page 100.

POPINET, S.; ZALESKI, S. A front-tracking algorithm for accurate representation of surface tension. **International Journal for Numerical Methods in Fluids**, v. 30, n. 6, p. 775–793, 1999. Citation on page 83.

QI, Y.; LU, J.; SCARDOVELLI, R.; ZALESKI, S.; TRYGGVASON, G. Computing curvature for volume of fluid methods using machine learning. **Journal of Computational Physics**, v. 377, p. 155 – 161, 2019. ISSN 0021-9991. Citations on pages 84, 85, and 87.

QIAN, J.; LAW, C. K. Regimes of coalescence and separation in droplet collision. **Journal of Fluid Mechanics**, Cambridge University Press (CUP), v. 331, p. 59–80, Jan. 1997. Citation on page 59.

QIAN, L.; CONG, H.; ZHU, C. A numerical investigation on the collision behavior of polymer droplets. **Polymers**, MDPI AG, v. 12, n. 2, p. 263, Jan. 2020. Citation on page 61.

RENARDY, M. The stresses of an upper convected maxwell fluid in a newtonian velocity field near a re-entrant corner. **Journal of Non-Newtonian Fluid Mechanics**, Elsevier BV, v. 50, n. 2-3, p. 127–134, Dec. 1993. Citation on page 58.

____. How to integrate the upper convected maxwell (UCM) stresses near a singularity (and maybe elsewhere, too). **Journal of Non-Newtonian Fluid Mechanics**, Elsevier BV, v. 52, n. 1, p. 91–95, Apr. 1994. Citations on pages 29 and 50.

____. Re-entrant corner behavior of the PTT fluid. **Journal of Non-Newtonian Fluid Mechanics**, Elsevier BV, v. 69, n. 1, p. 99–104, Mar. 1997. Citation on page 44.

____. Asymptotic structure of the stress field in flow past a cylinder at high weissenberg number. **Journal of Non-Newtonian Fluid Mechanics**, Elsevier BV, v. 90, n. 1, p. 13–23, Apr. 2000. Citation on page 44.

ROSENBERG, J.; KEUNINGS, R. Numerical integration of differential viscoelastic models. **Journal of Non-Newtonian Fluid Mechanics**, Elsevier BV, v. 39, n. 3, p. 269–290, Jan. 1991. Citation on page 44.

ROUSSEL, N.; COUSSOT, P. "fifty-cent rheometer" for yield stress measurements: From slump to spreading flow. **Journal of Rheology**, Society of Rheology, v. 49, n. 3, p. 705–718, May 2005. Citation on page 96.

SANTOS, D. D. dos; FREY, S. L.; NACCACHE, M. F.; MENDES, P. R. de S. Flow of elasto-viscoplastic liquids through a planar expansion–contraction. **Rheologica Acta**, v. 53, n. 1, p. 31–41, 2014. Citation on page 22.

SARAMITO, P. A new constitutive equation for elastoviscoplastic fluid flows. **Journal of Non-Newtonian Fluid Mechanics**, v. 145, n. 1, p. 1 – 14, 2007. ISSN 0377-0257. Citations on pages 22, 95, 97, and 98.

____. A new elastoviscoplastic model based on the Herschel-Bulkley viscoplastic model. **Journal of Non-Newtonian Fluid Mechanics**, v. 158, n. 1, p. 154 – 161, 2009. ISSN 0377-0257. Viscoplastic fluids: From theory to application. Citations on pages 22 and 95.

SARAMITO, P.; WACHS, A. Progress in numerical simulation of yield stress fluid flows. **Rheologica Acta**, v. 56, n. 3, p. 211–230, 2017. Citation on page 22.

SOMMERFIELD, M.; PASTERNAK, L. Advances in modelling of binary droplet collision outcomes in sprays: A review of available knowledge. **International Journal of Multiphase Flow**, v. 117, p. 182–205, 2019. Citation on page 60.

SOUSA, F.; OISHI, C.; BUSCAGLIA, G. Spurious transients of projection methods in microflow simulations. **Computer Methods in Applied Mechanics and Engineering**, v. 285, p. 659 – 693, 2015. ISSN 0045-7825. Citation on page 36.

SUN, K.; ZHANG, P.; LAW, C.; WANG, T. Collision dynamics and internal mixing of droplets of non-Newtonian liquids. **Physical Review Applied**, v. 4, n. 054013, p. 1–11, 2015. Citation on page 61.

TANG, C.; ZHAO, J.; ZHANG, P.; LAW, C.; HUANG, Z. Dynamics of internal jets in the merging of two droplets of unequal sizes. **Journal of Fluid Mechanics**, Cambridge University Press (CUP), v. 795, p. 671–689, 2016. Citation on page 60.

TAVARES, M.; KOFFI-BI, D.-A.; CHÉNIER, E.; VINCENT, S. A two-dimensional second order conservative front-tracking method with an original marker advection approach based on jump relations. **Communications in Computational Physics**, v. 27, n. 5, p. 1550–1589, 2020. ISSN 1991-7120. Citation on page 83.

THIEN, N. P.; TANNER, R. I. A new constitutive equation derived from network theory. **Journal of Non-Newtonian Fluid Mechanics**, Elsevier BV, v. 2, n. 4, p. 353–365, Jul. 1977. Citations on pages 21, 22, and 44.

THOMPSON, A. B.; TIPTON, C. R.; JUEL, A.; HAZEL, A. L.; DOWLING, M. Sequential deposition of overlapping droplets to form a liquid line. **Journal of Fluid Mechanics**, Cambridge University Press (CUP), v. 761, p. 261–281, Nov. 2014. Citation on page 96.

THOMPSON, R.; OISHI, C. Reynolds and Weissenberg numbers in viscoelastic flows. **Journal of Non-Newtonian Fluid Mechanics**, v. 292, n. 104550, p. 1 – 10, 2021. Citation on page 71.

TOMÉ, M.; BERTOCO, J.; OISHI, C.; ARAUJO, M.; CRUZ, D.; PINHO, F.; VYNNYCKY, M. A finite difference technique for solving a time strain separable k-BKZ constitutive equation for two-dimensional moving free surface flows. **Journal of Computational Physics**, Elsevier BV, v. 311, p. 114–141, Apr. 2016. Citation on page 24.

TOMÉ, M. F. **GENSMAC: a multiple free surface fluid flow solver**. Phd Thesis (PhD Thesis) — University of Strathclyde, 1993. Citation on page 36.

TOMÉ, M. F.; MEREJOLLI, R.; PAULO, G. S.; MCKEE, S. An assessment of the PTT model on the impacting drop problem. **Journal of the Brazilian Society of Mechanical Sciences and Engineering**, Springer Science and Business Media LLC, v. 40, n. 9, Sep. 2018. Citation on page 24.

TRYGGVASON, G.; BUNNER, B.; ESMAEELI, A.; JURIC, D.; AL-RAWAHI, N.; TAUBER, W.; HAN, J.; NAS, S.; JAN, Y.-J. A front-tracking method for the computations of multiphase flow. **Journal of Computational Physics**, Elsevier BV, v. 169, n. 2, p. 708–759, May 2001. Citation on page 83.

TRYGGVASON, G.; SCARDOVELLI, R.; ZALESKI, S. **Direct Numerical Simulations of Gas-Liquid Multiphase Flows**. [S.l.]: Cambridge University Press, 2011. Citations on pages 83 and 98.

UNVERDI, S.; G.TRYGGVASON. A front-tracking method for viscous, incompressible, multi-fluid flows. **Journal of Computational Physics**, Elsevier BV, v. 100, n. 1, p. 25–37, May 1992. Citation on page 83.

WALTERS, K.; WEBSTER, M. F. The distinctive CFD challenges of computational rheology. **International Journal for Numerical Methods in Fluids**, Wiley, v. 43, n. 5, p. 577–596, 2003. Citation on page 43.

WAPPEROM, P.; RENARDY, M. Numerical prediction of the boundary layers in the flow around a cylinder using a fixed velocity field. **Journal of Non-Newtonian Fluid Mechanics**, Elsevier BV, v. 125, n. 1, p. 35–48, Jan. 2005. Citation on page 44.

XU, M.; LI, X.; RISEMAN, A.; FROSTAD, J. M. Quantifying the effect of extensional rheology on the retention of agricultural sprays. **Physics of Fluids**, AIP Publishing, v. 33, n. 3, p. 032107, Mar. 2021. Citation on page 22.

XU, X.; TANG, T.; YU, P. A modified sph method to model the coalescence of colliding non-newtonian liquid droplets. **International Journal for Numerical Methods in Fluids**, v. 92, p. 372–390, 2020. Citations on pages 12, 61, and 69.


ICMC
USP
SÃO CARLOS